

EXPERIMENTAL AND NUMERICAL INVESTIGATION OF SHRINKAGE
MECHANISM OF PLAIN AND REINFORCED CONCRETE MEMBERS

A THESIS SUBMITTED TO
THE GRADUATE SCHOOL OF NATURAL AND APPLIED SCIENCES
OF
MIDDLE EAST TECHNICAL UNIVERSITY

BY

UTKU ALBOSTAN

IN PARTIAL FULFILLMENT OF THE REQUIREMENTS
FOR
THE DEGREE OF DOCTOR OF PHILOSOPHY
IN
CIVIL ENGINEERING

SEPTEMBER 2020

Approval of the thesis:

**EXPERIMENTAL AND NUMERICAL INVESTIGATION OF SHRINKAGE
MECHANISM OF PLAIN AND REINFORCED CONCRETE MEMBERS**

submitted by **UTKU ALBOSTAN** in partial fulfillment of the requirements for the degree of **Doctor of Philosophy in Civil Engineering Department, Middle East Technical University** by,

Prof. Dr. Halil Kalıpçılar
Dean, Graduate School of **Natural and Applied Sciences**

Prof. Dr. Ahmet Türer
Head of Department, **Civil Engineering**

Prof. Dr. Özgür Kurç
Supervisor, **Civil Engineering, METU**

Prof. Dr. İ. Özgür Yaman
Co-Supervisor, **Civil Engineering, METU**

Examining Committee Members:

Prof. Dr. Kağan Tuncay
Civil Engineering, METU

Prof. Dr. Özgür Kurç
Civil Engineering, METU

Assoc. Prof. Dr. Demirkan Çöker
Aerospace Engineering, METU

Assoc. Prof. Dr. Ahmet Hakan Argeşo
Manufacturing Engineering, Atılım University

Assoc. Prof. Dr. Özkan Kale
Civil Engineering, TED University

Date: 22.09.2020

I hereby declare that all information in this document has been obtained and presented in accordance with academic rules and ethical conduct. I also declare that, as required by these rules and conduct, I have fully cited and referenced all material and results that are not original to this work.

Name, Surname: Utku Albostan

Signature:

ABSTRACT

EXPERIMENTAL AND NUMERICAL INVESTIGATION OF SHRINKAGE MECHANISM OF PLAIN AND REINFORCED CONCRETE MEMBERS

Albostan, Utku
Doctor of Philosophy, Civil Engineering
Supervisor: Prof. Dr. Özgür Kurç
Co-Supervisor: Prof. Dr. İ. Özgür Yaman

September 2020, 132 pages

Concrete shrinkage is a long-term process causing a reduction in the volume of a concrete member. In the majority of the concrete models, shrinkage is considered as a uniform unrestrained shortening through the longest dimension, but in reality, due to the existence of aggregates and reinforcing bars, which restrains the shrinkage deformations, a non-homogeneous strain distribution occurs within the member. In order to measure such non-homogeneous deformations on an entire surface, digital image correlation (DIC) method is a good candidate. In the conventional DIC method, high-speed video cameras are utilized, but their measurement sensitivity may not be sufficient to detect shrinkage induced deformations in the order of μm . Thus, a novel DIC based measurement method for measuring drying shrinkage deformation on concrete surfaces is proposed that utilizes high-resolution images acquired by DSLR cameras. The validity of the proposed method is first tested on three different experimental studies. Then, shrinkage deformations of several concrete beams with and without reinforcement under free and restrained boundary conditions are measured with the proposed method for two months at a new experimental set-up designed for such experiments. This way, non-homogeneous strain distribution on the entire surface due to aggregates and reinforcing bars are obtained. In order to

numerically mimic the shrinkage behavior of plain and reinforced concrete members, a new mesoscale modeling and calibration approach is also developed that is based on overlapping lattice method. The validity of this new approach is tested by comparing the numerical results with the DIC measurements of the shrinkage experiments. Numerical results demonstrate that the proposed numerical approach has the capability of modeling shrinkage deformations of plain and reinforced concrete members.

Keywords: Concrete Shrinkage, Digital Image Correlation, Mesoscale Concrete Model, Overlapping Lattice Model

ÖZ

BETON VE BETONARME ELEMANLARIN BÜZÜŞME MEKANİZMASININ DENEYSEL VE SAYISAL OLARAK İNCELENMESİ

Albostan, Utku
Doktora, İnşaat Mühendisliği
Tez Danışmanı: Prof. Dr. Özgür Kurç
Ortak Tez Danışmanı: Prof. Dr. İ. Özgür Yaman

Eylül 2020, 132 sayfa

Beton büzüşmesi, bir beton elemanın hacminde azalmaya neden olan uzun vadeli bir süreçtir. Güncel beton modellerinin çoğunda büzüşme, en uzun boyut boyunca sabit ve sınırlandırılmamış bir kısalma olarak kabul edilir, ancak gerçekte, elemanın içerisinde büzüşme deformasyonlarını sınırlayan agregaların ve donatıların varlığı nedeniyle homojen olmayan bir gerinim dağılımı meydana gelir. Tüm yüzeydeki bu tür homojen olmayan deformasyonları ölçmek için dijital görüntü korelasyon (DIC) yöntemi iyi bir adaydır. Geleneksel DIC yönteminde, yüksek hızlı video kameralar kullanılır, ancak bunların ölçüm hassasiyeti, büzüşmeden kaynaklı mikrometre mertebesindeki deformasyonları ölçmek için yeterli olmayabilir. Bu nedenle, bu çalışmada DSLR kameralar aracılığıyla elde edilen yüksek çözünürlüklü görüntüleri kullanarak, beton elemanların yüzeylerinde oluşan kuruma kaynaklı büzüşme deformasyonunu ölçmek için yeni bir DIC tabanlı ölçüm yöntemi önerilmiştir. Önerilen yöntemin geçerliliği ilk olarak üç farklı deneysel çalışmada test edilmiştir. Daha sonra, birkaç beton kirişin serbest ve sınırlandırılmış sınır koşulları altında donatılı ve donatısız büzüşme deformasyonları, bu yeni deney düzeneğinde iki ay süreyle önerilen yöntemle ölçülmüştür. Bu sayede tüm yüzeyde agregalar ve donatı çubuklarından dolayı homojen olmayan gerinim dağılımı elde edilmiştir. Düz ve

betonarme elemanların bzme davranıını sayısal olarak elde etmek iin, rten kafes yntemine dayanan yeni bir mezo-lek modelleme ve kalibrasyon yaklaımı da gelitirilmitir. Bu yeni yaklaımın geerlilięi, sayısal sonuların bzme deneylerinin DIC lmleri ile karılatırılmasıyla sınınmıtır. Elde edilen sayısal sonular, nerilen sayısal yaklaımın dz ve betonarme elemanların bzme deformasyonlarını modelleme kapasitesine sahip olduęunu gstermektedir.

Anahtar Kelimeler: Betonun Bzme Mekanizması, Dijital Grnt Korelasyonu, Meso-lekli Beton Modeli, rten Kafes Yntemii

To My Family

ACKNOWLEDGEMENTS

I wish to express my utmost gratitude to my supervisor Prof. Dr. Özgür Kurç and co-supervisor Prof. Dr. İ. Özgür Yaman for their guidance, advice, criticism, support, encouragement and insight throughout the research.

Prof. Dr. Kağan Tuncay and Assoc. Prof. Dr. Demirkan Çöker are also sincerely acknowledged for their valuable support.

I owe special thanks to the staff of METU Structural Mechanics Laboratory, METU Construction Materials Laboratory, METU Petroleum Research Center, and METU Wind Energy Research Center for valuable help in the experimental part of this study.

I would like to present my gratitude to Mehmet Kemal Ardoğa for invaluable support during material testing. I would like to thank Ruhi Deniz Yalçın, Münci Tunç Kalaycıoğlu, and Gökberk Işık for their help in laboratory works.

I would like to thank my co-workers in LARSA, Inc. for their understanding and support.

I am grateful for all continuous support, understanding and encouragement I have received from all of my family members. I would like to express my gratitude to my wife Feyza Soysal Albostan for her continuous support and endless patience throughout this study and in all aspects of my life.

I would also like to appreciate my friends for standing next to me during this process

This study has been conducted with the funds BAP-03-03-2015-002 and BAP-03-03-2017-006 from the Middle East Technical University.

TABLE OF CONTENTS

ABSTRACT	v
ÖZ.....	vii
ACKNOWLEDGEMENTS	x
TABLE OF CONTENTS	xi
LIST OF TABLES	xiv
LIST OF FIGURES.....	xv
CHAPTERS	
1. INTRODUCTION	1
1.1. Problem Definition	1
1.2. Related Work.....	4
1.3. Objectives and Scope	8
1.4. Thesis Outline.....	10
2. Development of DIC Measurement Technique	13
2.1. Introduction	13
2.2. Fundamentals of DIC Method	15
2.3. A Novel DIC Methodology for Small Deformations Governing in a Long Duration.....	18
2.4. Validation of the Proposed DIC Measurement Method	23
2.4.1. Experiment 1: Concrete under Uniaxial Compression	24
2.4.1.1. Experimental Setup	24
2.4.1.2. Comparison of Results	26
2.4.2. Experiment 2: Three-Point Bending Test of RC Beam	31

2.4.2.1. Experimental Setup.....	31
2.4.2.2. Comparison of Results.....	34
2.4.3. Experiment 3: Reinforced Concrete Pressure Tunnel	38
2.4.3.1. Experimental Setup.....	39
2.4.3.2. Comparison of Results.....	43
2.5. Summary	46
3. Measuring Shrinkage Deformations of Concrete Members.....	49
3.1. Introduction.....	49
3.2. Properties of Concrete Constituents and Mix Design.....	50
3.2.1. Aggregates.....	51
3.2.2. Cement.....	53
3.2.3. Water	54
3.2.4. Concrete Mix Design.....	54
3.2.5. Mechanical Properties of Concrete	55
3.2.5.1. Elastic Modulus and Compressive Strength Tests.....	56
3.2.5.2. Tensile Strength Test	58
3.3. Validation of the Shrinkage Testing Apparatus by DIC	61
3.3.1. Experimental Configuration	61
3.3.2. Uncertainty Estimation.....	68
3.3.3. Comparison of Results	71
3.4. Free and Restrained Shrinkage Testing of Concrete by DIC.....	78
3.4.1. Experimental Configuration	78
3.4.2. Comparison of Results	82
3.5. Summary	84

4. Numerical Modeling	87
4.1. Introduction	87
4.2. Theory of Overlapping Lattice Model.....	88
4.3. Analytical Modeling.....	94
4.3.1. Mortar Shrinkage Strain.....	103
4.4. Validation Studies	105
4.4.1. Two-Dimensional OLM Analysis	105
4.4.2. Three-Dimensional OLM Analysis	110
4.5. Summary.....	115
5. Conclusion and Future Works	117
5.1. Executive Summary.....	117
5.2. Concluding Remarks	119
5.3. Recommendations for Future Study	121
REFERENCES.....	123
CURRICULUM VITAE	131

LIST OF TABLES

TABLES

Table 2-1 Camera Configuration Parameters	25
Table 2-2 Camera Configuration Parameters	32
Table 2-3 Camera Configuration Parameters	41
Table 2-4 Camera Configuration Parameters	42
Table 3-1 Granulometry of Aggregate (ASTM C136-06).....	53
Table 3-2 Mix Design Input Parameters.....	55
Table 3-3 Compressive Strength and Elastic Moduli	58
Table 3-4 Tensile Strengths and Elastic Moduli.....	60
Table 3-5 Camera Configuration Parameters	68
Table 3-6 Camera Configuration	81
Table 4-1 Modified Material Parameters.....	101
Table A-1 Features of DSLR cameras.....	129

LIST OF FIGURES

FIGURES

Figure 2-1 Sample Surface (a), Sample Surface Covered Fully with Strain Gauges (b)	14
Figure 2-2 Raster Points.....	16
Figure 2-3 Single Pixel Tracking Example.....	17
Figure 2-4 Flow Chart of DIC Measurement Process.....	19
Figure 2-5 Pattern Samples (SEM, 2014) and GOM Correlate (2018) Pattern Quality Average Values	21
Figure 2-6 Target Objects (a), Target Pattern (b)	23
Figure 2-7 Concrete Specimen (one-quarter of the cubic specimen).....	25
Figure 2-8 Example Image Shift on Images	26
Figure 2-9 Vertical Displacement Distributions	28
Figure 2-10 Vertical Displacement at Bottom End.....	29
Figure 2-11 Experimental Results. Final Image Captured just before the failure (a), Final Image at the end (just after the failure) (b), DIC - First Principal Strain (just before the failure) (c), Video Magnification Method (just before the failure) (d).....	30
Figure 2-12 Experimental Setup (a), DIC Systems (b), LVDT Locations (c)	32
Figure 2-13 Loading Schemes. LS1 (a), LS2 (b)	34
Figure 2-14 Displacement and Strain Distributions under Load of 7 tons. Displacement Distribution in Horizontal Direction (a), Displacement Distribution in Vertical Direction (b), First Principal Strain Distribution (c), Final State (d).....	35
Figure 2-15 Displacement Plots. Vertical Displacement (a), Horizontal Displacement at Top (b), Horizontal Displacement at Bottom (c)	36
Figure 2-16 Displacement and Strain Distributions under Load of 27.8 tons. Displacement Distribution in Horizontal Direction (a), Displacement Distribution in Vertical Direction (b), First Principal Strain Distribution (c), Visible Cracks (d).....	37

Figure 2-17 Displacement Plots. Horizontal Displacement at Top (a), Horizontal Displacement at Bottom (b), Vertical Displacement (c)	38
Figure 2-18 Experimental Setup. (Loading Mechanism (a), Lining (b), Rock Body (c), Pre-tensioning System (d)) ((Kalaycıoğlu et al., 2018).....	39
Figure 2-19 LVDT and Strain Gauge Locations	40
Figure 2-20 Camera Properties, Locations and ROI's.....	41
Figure 2-21 Camera ROI's	43
Figure 2-22 First Principal Strain Distributions (Combination of results of all cameras)	44
Figure 2-23 Comparison with Strain Gauges Readings	46
Figure 3-1 Aggregates. 4-12 mm (a), 0-4 mm (b)	51
Figure 3-2 XRD Device (a), Crushed Limestone Sample (b), XRD Spectrum (c) ...	52
Figure 3-3 Gradation of Aggregates	53
Figure 3-4 Cement	54
Figure 3-5 Concrete Mix (a), Slump Test (b)	55
Figure 3-6 Elastic Modulus Test Setup (a), Compressive Strength Test Setup (b), Elastic Modulus Test Results of samples with M1 concrete at the 43 rd day (c), Compressive Strength Test Results of samples with M1 concrete at the 43 rd day (d)	57
Figure 3-7 Dog-Bone Shaped Sample. Dimensions (a), Samples Photos Before and After the Test (b)	59
Figure 3-8 Tensile Strength Test Setup and Strain Gauge (a), M1 at 13 th day (b), M1 & M1-M at 29 th day (c).....	60
Figure 3-9 Location of Single Coarse Aggregate in the sample with M1 tested at the 29 th day	61
Figure 3-10 Concrete Specimen	62
Figure 3-11 Specimen Dimensions (cm). S1-M1 & S1-M2 (a), S2-M1-R (b).....	63
Figure 3-12 Experimental Setup.....	64
Figure 3-13 Curing (a), Broken Specimen while Locating to the Testing Apparatus (b)	65

Figure 3-14 Samples	65
Figure 3-15 Color Change Effect on Speckles during Concrete Drying. First Day of the Test (a), 45 th Day of the Test (b)	66
Figure 3-16 Positions and Views of Cameras and LVDT Contact Points. Camera Positions (a), Top Camera View of S1 (b) and S2 (c), Side Camera View of S2 (d)	67
Figure 3-17 Camera Schematic for Calculation of Image Acquisition Uncertainty (a), Out of Plane Displacement Uncertainty (b)	69
Figure 3-18 LVDT Locations (a & b) and Displacements at Free End (c, d, e, & f) (S1)	73
Figure 3-19 Longitudinal Displacement (a) and 1 st Principal Strain Distributions (b) at the Final State	74
Figure 3-20 Horizontal Strain Distributions of Original and Modified Images	75
Figure 3-21 Second Principal Strain Distribution and Section Cuts of S1-M1	76
Figure 3-22 Horizontal Displacement (a) and First Principal Strain (b) Distributions of S2-M1-R	78
Figure 3-23 Reinforcement Details (a), Reinforcement in the Mold (b), Molds used (c)	79
Figure 3-24 Cylindrical and Dog-Bone Shaped Samples	80
Figure 3-25 Experimental Setup	81
Figure 3-26 LVDT Locations and Displacements at Free End (S1)	83
Figure 3-27 Propagation of First Principal Strains on FSS and RSS with Time.	84
Figure 4-1 Sample Horizon for OLM ($a = 1.5$)	89
Figure 4-2 Sample Domains. Continuum Approach (a), OLM (b)	90
Figure 4-3 Three-Dimensional OLM Domain	92
Figure 4-4 3D View of Specimen Domain (a), Probability Density Function of Aggregate Granulometry (b), 3D View of Specimen with Aggregates (c), Location of Aggregates in a Section Cut (d)	95
Figure 4-5 Discretized Domain Coarse Aggregates only (a), Reinforcement and Coarse Aggregates (b)	96
Figure 4-6 Truss Element Exist on Interface (a), Duplicated Truss Elements (b)	97

Figure 4-7 Elastic Modulus of Mortar (a), Stress-Strain curve for ITZ (b).....	99
Figure 4-8 Mortar Material Model Example	100
Figure 4-9 Tensile Behavior	101
Figure 4-10 Time-Dependent Elastic Modules.....	103
Figure 4-11 Time-Dependent Shrinkage Deformation Curves	104
Figure 4-12 Scanning Concrete Samples via Tomography	105
Figure 4-13 Tomography Image of Right Surface (a), Two-Dimensional OLM Model (b), OLM Strain Distribution of Right Surface (c), DIC and OLM Strain Distributions on the Specimens (d & e).....	107
Figure 4-14 Tomography Image of Top Surface (a), Two-Dimensional OLM Model (b), OLM Strain Distribution of Top Surface (c), DIC Strain distribution at top Surface (d), DIC and OLM Strain Distributions on the Specimens (e).....	109
Figure 4-15 Free End Displacement of FSS	111
Figure 4-16 Free End Displacement of RSS.....	112
Figure 4-17 Longitudinal Element Strain (a), Computed First Principal Strain Distribution (b)	113
Figure 4-18 Propagation of First Principal Strains on FSS and RSS with Time.....	113
Figure 4-19 Strain Distributions of FSS. First Principal Strain Distribution (DIC) (a), First Principal Strain Distribution (OLM) (b)	114
Figure 4-20 Strain Distributions of RSS. First Principal Strain Distribution (DIC) (a), First Principal Strain Distribution (OLM) (b)	115

CHAPTER 1

INTRODUCTION

1.1. Problem Definition

In plain concrete and reinforced concrete members, shrinkage results in a reduction in volume with time (Hedegaard, 2020; Wallah, 2009). Shrinkage causes additional tensile forces on restrained members having larger surface areas such as slabs or walls, which may result in cracking and complicated progressive collapse (Tang et al., 2016; Weiss et al., 1998). Similarly, shrinkage cracks can propagate on concrete pavements due to restraints at the bottom interface. Thus, understanding shrinkage mechanisms in such members and having analytical/computational methods for computing the effects of shrinkage are crucial for a robust design of such members.

Shrinkage is a complex and long-term process. The volume reduction due to shrinkage is considered to continue for many years, and usually, four significant mechanisms, i.e., plastic, autogenous, drying, and carbonation shrinkage, are deemed to be effective. Plastic shrinkage is caused by the loss of water from the surface due to evaporation after casting of the concrete and is considered to be one of the main reasons for surface cracks if the concrete is not adequately cured (Holt, 2005; Qi, 2005). Autogenous and drying shrinkage initiate in the early ages of concrete but may continue up to several years. As autogenous shrinkage occurs due to the loss of water during the hydration process, carbonation shrinkage initiates as the concrete becomes exposed to carbon dioxide in the air. Moreover, volume reduction due to shrinkage in concrete members is not uniform. Shrinkage is effective in the cement paste, while aggregates restrain the amount of volume reduction depending on their relative stiffness to the cement paste. Furthermore, the water demand for the aggregate is another parameter that affects the shrinkage (Rao, 2001; Mokarem, 2002). Thus,

numerical modeling and simulating the behavior of members under the effect of shrinkage is a very complex task.

Because of this reason, concrete shrinkage is handled mainly in a simplified manner for engineering purposes. Concrete is considered as a homogeneous material and shrinkage mechanism is defined as a uniform shortening through the longest dimension of a member (Rao, 2001; Tang et al., 2011). Such a simplified approach may work for beams and columns whose length is much larger than their sectional dimensions; however, better numerical methods are required for slabs and walls where shrinkage is effective in both directions, i.e., along the length and width. In addition to this, all the current shrinkage models only describe the shortening of concrete, they don't give any guidelines about how the shrinkage deformations are influenced when there are reinforcing bars within the member. As a result, there is still a need for better computational methods that not only describe the shrinkage effects for every type of member but also considers the effect of reinforcing bars that act as a local restraint against shrinkage as well as the aggregates.

Such local restraining effects can only be observed and hence modeled if the deformation of the whole surface can be measured for a long duration of time, weeks even months. The digital image correlation based measurement method (DIC) is a good candidate for this purpose. The DIC method is frequently utilized in recent years for measuring displacement, strain, and cracks on deforming surfaces. The method is based on the comparison of back to back acquired high-resolution images of a surface by tracking the motion of many points on the surface where the surface is painted by randomly located speckles (Buttlar et al., 2014; Gajewski & Garbowski, 2014; Romeo, 2013; Sutton et al., 2009). The main advantage of DIC-based measurements is that it requires no contact with the specimen and provides the evolution of the displacement field of a surface in an automated way.

In spite of this powerful feature of the DIC method, it has measurement accuracy limitations regarding the resolution of the used cameras. Generally, high-speed video

cameras are preferred to catch every detail of the deformation that the specimen will be subjected to. However, those cameras' resolutions are limited. For understanding the concrete shrinkage mechanism, measuring relatively small deformations, such as concrete strains, can only be done by focusing on a specific relatively small region.

As an alternative option to high-speed cameras, a single high-resolution camera such as DSLR camera, whose image resolution is much higher in photograph mode, can be utilized for measuring such relatively small deformations on larger surfaces without losing sensitivity provided that the speed of the camera can catch the rate of deformation. Photo shooting, however, causes additional issues that affect the measurement accuracy because this type of camera is not designed for this purpose. Hence, this study proposes a novel methodology, which mostly fixes such device-based issues and allows utilizing such high-resolution DSLR cameras in DIC measurements without losing sensitivity for a long duration of time.

Modeling the shrinkage effects of members with any shape and under the influence of different boundary conditions requires further attention. From an engineering point of view, macro-scale modeling, assuming homogeneous material behavior, is usually preferred due to its simplicity for both linear and nonlinear behaviors. Constant length change throughout an element due to shrinkage is assumed and any localization inside the element volume is not considered.

The highly heterogeneous composition of concrete makes the physics of shrinkage behavior significantly more complicated at the mesoscale since considering the local restraints such as coarse aggregates and reinforcing bars, which results in strain localization. When these localized strains exceed the elastic limit, nonlinear behavior like cracking occurs. For such problems, macro-scale modeling approaches are powerless as they focus on average behavior and do not account for such strain localization. Spatio-temporal evolution of material and interface properties should be considered in models; accordingly, a mesoscale model that takes those effects into account could be used.

Particle-based approaches such as lattice methods and recently emerging peridynamics are strong alternatives to continuum-based finite element methods for simulating the nonlinear behavior of brittle materials. These approaches can be considered to be non-local continuum models in which particles influence other particles within a specified distance (horizon), and damage occurs at the connection between these particles (Silling & Askari, 2005). This modeling approach is based on the integration over the horizon instead of differentiating the domain. Hence, it concerns the force equilibrium, and if any interaction is lost, i.e., cracked, the formulations are still valid. Overlapping Lattice Model (OLM) is the simplest version of the peridynamics approach in which connections between horizons are set by pin-connected truss elements (Aydin et al., 2018, 2019; Soysal Albostan et al., 2017). Hence the other contribution of this study is to propose a novel methodology about how to generate mesoscale OLM models of the real samples stochastically and how to simulate shrinkage induced deformations of concrete members with and without reinforcing bars.

1.2. Related Work

Shrinkage mechanism is mainly defined as a uniform shortening through the longest dimension of a member and concrete is usually considered as a homogenous material for engineering purposes (Rao, 2001; Tang et al., 2011). In order to determine the axial strain due to shrinkage shortening, there are various standard tests (ASTM C596, RILEM TC 107-CSP, ASTM C1581, etc.). Free shrinkage test, i.e., the members are free to deform, focus on measuring the amount of shortening in one-dimensional members. For one-dimensional members, i.e., one of the dimensions is relatively larger than the other two, such as column or beam, length change is considered only along the longest dimension. The effects of shrinkage along the other two directions are neglected as shrinkage effects are not considered to be essential for those directions. At the end of the test, shrinkage strain vs. time relationship is obtained

where the strain is calculated by dividing the amount of shortening with the initial length of the member. Restrained shrinkage tests, i.e., members are not allowed to deform, are mainly conducted to determine the age of cracking and induced tensile stress of the material. The main challenge of such tests is the requirement of doing the test under constant temperature and relative humidity for a time period of up to 64 weeks, according to ASTM C157 (ASTM International, 2017a).

The majority of the experimental studies on the shrinkage behavior of cementitious materials follow the provisions of the aforementioned standard test methods (Grzybowski & Shah, 1989; Keskin et al., 2014; Mokarem, 2002; Weiss et al., 1998). In these studies, the lengths of the members are much longer than the other dimensions so that shrinkage can be assumed to be active only along the length of the member. Measurements are taken at certain points at one end of the members. There are also studies that focus on the shrinkage behavior of concrete plates where shrinkage is effective both along the length and width of the member (Almusallam, 2001; Holt, 2005; Holt, 2001). In these studies, displacement measurements are also taken at several points with conventional instruments. Thus, the majority of the experimental studies on the shrinkage behavior of concrete members focus on the global behavior of members rather than considering local effects that can only be observed by measuring the deformation of the whole surface.

In recent years, the digital image correlation method (DIC) is more frequently utilized for measuring displacement, deformation, and cracks on the surface (Destrebecq et al., 2011; Nghiem et al., 2015; Romeo, 2013; Shah & Kishen, 2011). The method is based on comparison of back to back acquired high-resolution images of a surface by tracking the motion of many points on the surface where the surface is painted by randomly located speckles (Baril et al., 2016; Buttlar et al., 2014; Gajewski & Garbowski, 2014; Sutton et al., 2009). The main advantage of DIC based measurements is, it requires no contact with the specimen and can provide full displacement field of surface in an automated way (Hoult et al., 2016).

The majority of the studies utilized the DIC method captured images via video cameras (Buttlar et al., 2014; Jin et al., 2015). These studies mainly focus on short-duration experiments with a rather small area of interest due to the limited resolution of cameras used. Buttlar et al. (2014) used the DIC method to observe mode I fractural behavior on a 5x6.5 cm area with a 2MP camera. Similarly, Jin et al. (2015) focused on a rather small area of a circular laminated composite plate whose dimensions are 7x7 cm by using 4.2 MP cameras for the DIC measurement of thermal buckling. Measurement of shrinkage deformation of cementitious materials, on the other hand, requires either a smaller surface area for a low-resolution camera or a larger surface area for a high-resolution camera and measurement for a much more extended period. Qi et al. (2003) tracked shrinkage induced crack propagation in a restrained slab by utilizing the DIC method at the age of 24 hours. They selected image frame size as 480x480 pixels (17x17 mm image size) to gather sufficient resolution to identify fine cracks. Due to image size limitation, to visualize a crack pattern that was 200mm in length, they moved the sample under the camera and they captured a series of images throughout the cracking path. Mauroux et al. (2012) focused on identifying cracks due to drying in coating mortars for 10 days with the DIC method. They utilized two DSLR cameras with 2MP resolution for measuring deformations at the top (20x20 cm) and side (20x1 cm) surfaces of specimens, respectively. Likewise, Maruyama et al. (2016) investigated the role of aggregates on the drying shrinkage of concrete. They measured the local restraint of aggregates during the shrinkage process with an 8.4 MP high-resolution camera and computed local strains on a maximum 19x10 cm surface area with the DIC method for more than 400 days.

From an engineering point of view, macroscale modeling, assuming homogeneous material, is preferred due to its simplicity for both linear and nonlinear behavior. Shrinkage induced length change is assumed to be constant throughout an element volume and any localization inside the element volume is not accounted for (Di Luzio, 2009; Grasley & Lange, 2004; Tang et al., 2011; Turcry et al., 2006; Weiss et al., 2000). Various design codes and guides suggest using shrinkage prediction models,

which are empirical expressions based on experimental studies and focus solely on one-dimensional behavior (ACI Committee 209, 2008; Baweja, 1995; Hedegaard, 2020). Standard test methods that aim to determine shrinkage properties of mortar and concrete samples suggest measuring total length change in the longest dimension of the sample (ASTM International, 2017a, 2017b). Describing the shrinkage deformation as total length change can be used even for multi-dimensional structural elements by considering each direction separately (Almusallam, 2001; Holt, 2001).

A highly heterogeneous composition of concrete makes the physics of shrinkage behavior significantly more complicated at the mesoscale (Idiart et al., 2011). Local restraints such as coarse aggregates and reinforcing bars cause strain localization. As localized strains exceed the elastic limit, cracks occur, resulting in highly nonlinear behavior at mesoscale. For such problems, macroscale modeling approaches are powerless as they focus on average behavior and do not account for strain localization. To shed light on the mesoscale shrinkage behavior, mesoscale modeling accounting for spatial heterogeneity is required, and the model should take into consideration the spatial distribution of constituents and spatio-temporal evolution of material and interface properties.

In literature, a number of mesoscale models that focus on the shrinkage behavior of concrete have been proposed and most of them are based on the finite element approach (Idiart et al., 2011; Maruyama & Sugie, 2014; Tang et al., 2016, 2013). These studies focus on micro-crack formation due to the drying shrinkage of concrete. For this purpose, they generated two-dimensional finite element models in the mesoscale level to investigate moisture diffusivity within concrete or aggregate size effect in not only mesoscale but also at the macroscale level.

Particle-based approaches such as lattice methods and recently emerging peridynamics are strong alternatives to continuum-based finite element methods (FEM) for simulating the nonlinear behavior of brittle materials (Maruyama et al., 2016). These approaches can be considered to be non-local continuum models in

which particles influence other particles within a specified distance (horizon), and damage occurs at the connection between these particles (Silling & Askari, 2005). This modeling approach is based on the integration over the horizon instead of differentiating the domain. Hence, it concerns the force equilibrium, and if any interaction is lost, i.e., it is cracked, the formulations are still valid. It can be used for modeling shrinkage induced cracks in concrete (Grassl et al., 2010; Luković et al., 2016; Maruyama et al., 2016; Sadouki & Van Mier, 1997; Schlangen et al., 2007). Overlapping Lattice Model (OLM) is the simplest version of the peridynamics approach in which the connection between horizons is set by pin-connected truss elements (Aydin et al., 2018, 2019; Soysal Albostan et al., 2017) where the authors validated the method by solving several benchmark problems that involve simulation of fracture in plain and reinforced concrete structures. Furthermore, they generated FEM and OLM models of several dam bodies to compare crack patterns and concluded that OLM better estimates the discrete crack profile.

1.3. Objectives and Scope

There are three main objectives of this study. The first objective is to develop a novel measurement technique in order to obtain surface deformations of a concrete member under the effect of shrinkage deformations. By using this measurement technique, conducting shrinkage experiments on concrete specimens with/without reinforcements that have different concrete mixes is the second main objective of this study. This way, more detailed strain distribution over a surface would be obtained and these results could be compared with the results of the more refined numerical simulations. Thus, the final objective is to simulate the shrinkage deformation of these concrete members utilizing the overlapping lattice model method to question the capability of this method to describe the shrinkage behavior of concrete as well as reinforced concrete members.

For the first objective, the DIC method is utilized as a measurement method. During the measurements, high-resolution DSLR cameras that can provide more details in the images are used in order to increase the measurement sensitivity of the DIC method. This approach not only allows to recognize relatively small deformations that can occur primarily in concrete members but also takes measurement for a long duration of time. Their sensors have more pixels than the high-speed cameras; accordingly, a larger area of interest for the measurement can be obtained as well. On the other hand, they have several drawbacks such as distortions, noises, and mechanical vibration of the shutter mechanism and these drawbacks may reduce measurement accuracy. To handle these drawbacks, several improvements are applied to the captured images after the experiment. The efficiency and accuracy of performing DIC measurements using DSLR cameras together with the proposed improvements are tested at different types of experiments, i.e., concrete compression test, three-point flexure test of a reinforced concrete beam, reinforced concrete pressure tunnel test.

A new experimental setup is designed for measuring long-term drying shrinkage deformation of either plain or reinforced concrete members with the proposed DIC measurement method. For this purpose, initially, two sets of experiments were conducted for ten days to examine the effects of gravels and reinforcing bars on shrinkage deformations as well as to obtain a figure of merit of the proposed measurement approach. Furthermore, the top and side surfaces of the specimen were measured independently to validate the results of the DIC measurement. After the experiments, a good match was obtained in the first principal strain distributions at the neighborhood edge of the top and side surfaces, which gave enough confidence about the experimental setup to start the actual shrinkage experiments.

The actual experiments were conducted for a much longer time (i.e., for 61 days). Two beams, one was made up of plain concrete and the other one had reinforcing bars in it, were tested to observe free and internally restrained shrinkage deformations. The experiments were successfully completed and the surface displacement and strain distribution variations for 61 days were obtained for both specimens. The results were

in good agreement with the LVDT measurements and the restraining effects of reinforcing bars were clearly observed at the surface strains.

As a final step, a new mesoscale modeling approach to simulate three-dimensional shrinkage behavior of plain concrete and reinforced concrete members is proposed. This approach is based on the OLM method. In this approach, first, three-dimensional models of the experimental specimens were modeled with one-dimensional (truss) elements. The stiffness of these truss members was calibrated by equating the internal energies of the generated system to the continuum strain energy. Several nonlinear material behaviors were obtained from the laboratory tests of the material samples. The methods for generating the heterogeneous material matrix properly and selecting the corresponding material properties for different components of the material matrix in a simplified manner are also discussed. All computations were performed using Matlab R2015a (*MATLAB*, 2015). As validation studies, first, two-dimensional models for the specimen with plain concrete was generated. The material matrix was generated close to the actual case by using slices of the 2D tomography images of the specimen. Then, the results of the OLM simulations and DIC measurements were compared. As a second validation study, a full three-dimensional model of the experimental samples with and without reinforcements were analyzed. This time, the material matrices were synthetically generated and the results of 3D OLM simulations were compared with the experimental DIC measurements as well as the CIB-FIB 90 shrinkage model.

1.4. Thesis Outline

The outline of the thesis is as follows. Fundamentals of the DIC method and theory of proposed improvements for it to increase measurement sensitivity are discussed in Chapter 2. Validation studies that are conducted to test the accuracy of the proposed improvements are also presented in the second chapter. Details of the experimental setup for measuring shrinkage deformation of cementitious materials and its validation

studies are covered in Chapter 3. In this chapter, the results of various shrinkage experiments, including both free and restrained conditions, are presented. Moreover, features of the concrete constituent materials and the basic properties of the concrete are explained. Chapter 4 involves details of the numerical modeling approach for simulating the shrinkage behavior of concrete. Thus, the theory of the Overlapping Lattice Model (OLM) and the required elastic and inelastic calibrations of certain parameters are described in Chapter 4. Finally, Chapter 5 summarizes the main aspects of this study and presents the main conclusions of the thesis.

CHAPTER 2

DEVELOPMENT OF DIC MEASUREMENT TECHNIQUE

2.1. Introduction

DIC measurement fulfills two or three-dimensional displacements and strain distribution for the whole surface, which makes it more powerful than the classical instruments, such as LVDTs and strain gauges. Getting strain distribution through the whole surface of any larger specimen, for instance, requires placing many strain gauges and interpolating and/or extrapolating their measurements (Figure 2-1). Accordingly, using strain gauges for such a purpose is not practical, although they provide higher accuracy for the average strain measurements through their lengths. Moreover, proper gluing those instruments to the surface properly is quite difficult; accordingly, special attention is required for that process. Similarly, obtaining displacement distribution of any surface by utilizing only LVDTs is not practical; hence, only relative/absolute displacement measurement for specific points are preferred instead. DIC, on the other hand, provides those surface displacement and strain distributions without touching the specimen, which makes it advantageous for surface deformation measurements.

In spite of this powerful feature of the DIC method, it has measurement accuracy limitations regarding the resolution of the used cameras. Generally, high-speed video cameras are preferred to catch every detail of the sample that it will be subjected to. However, those cameras' resolutions are limited. For this problem in hand, measuring relatively small deformations, such as concrete strains, can be done by focusing on a specific relatively small region only. This limitation may result in a similar situation as in the case with strain gauges, which is the requirement of using multiple measurement instruments to measure the deformation of an entire surface.

As an alternative, a single high-resolution camera such as DSLR whose image resolution is higher in photograph mode can be utilized for measuring such relatively small deformations on larger surfaces without losing sensitivity provided that the speed of the camera can catch the rate of deformation. Photo shooting, however, causes additional issues that affect the measurement accuracy because this type of camera is not designed for this purpose. At this point, this study proposes a novel methodology, which mostly fixes such device-based issues. This way, such high-resolution cameras can be utilized in DIC measurements without losing sensitivity.

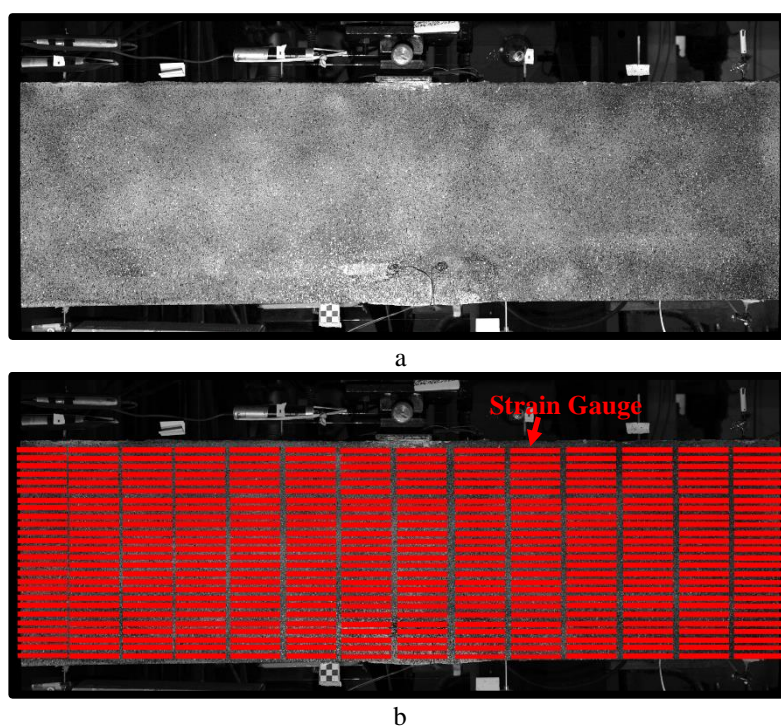


Figure 2-1 Sample Surface (a), Sample Surface Covered Fully with Strain Gauges (b)

In this chapter, first, the fundamentals of the DIC method are briefly covered. After that, the novel methodology for using high-resolution DSLR cameras in DIC measurements and its validation for various engineering applications are discussed.

2.2. Fundamentals of DIC Method

The main advantage of the DIC method is, not requiring any contact with the specimen for measurement during an experiment. This method allows measuring the displacements and strain distributions on the surface of the sample either in two or three dimensions. Stereo cameras are needed for the three-dimensional measurements provided that the optical axes of both cameras coincide on the specimen's surface. One single camera, on the other hand, is sufficient for the two-dimensional measurement that could be the choice for cases having negligible out of plane motions. In this case, the camera should be located in such a way that the normal of the specimen surface is perpendicular to the sensor plane, i.e., it should be parallel to the optical axis of the camera (Gajewski & Garbowski, 2014; Romeo, 2013; Sutton et al., 2009).

In the DIC method, the surface of the specimen is painted in such a way that the surface has a random speckle pattern. The accuracy of the technique depends on pattern quality directly. Speckles should be distributed homogeneously, and their diameters should be as small as possible (Romeo, 2013). Speckles, nevertheless, should not be smaller than 3-5 pixels to identify the feature of interest correctly (Lionello & Cristofolini, 2014).

Measurements are based on tracking user-defined points on the surface of the specimen, called raster points, at back to back grey scaled images that follow the deformation of the sample (Figure 2-2). The raster points are considered with their neighbor pixels within a region. Such regions are called facets, and random speckle pattern induced stochastic information of the faces simplifies tracking a particular raster point on another image called deformed image that shows the deformed state.

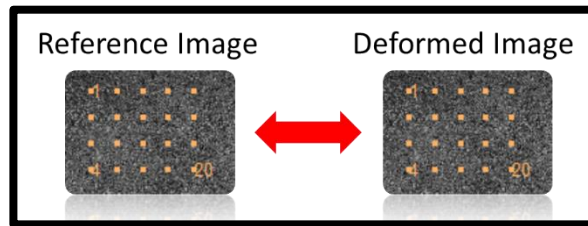


Figure 2-2 Raster Points

Tracking single pixels, rather than facets, may not be stable for cases that displacements are less than the size of a single-pixel. In Figure 2-3, pixel intensities received from any part of an image is represented with colors and numbers, and the center pixel, which is indicated with a red border and will be tracked, is shown. When the pattern shifts 0.5-pixel in the horizontal direction in the picture, only the half size of the current point becomes visible for the center pixel. The remaining half portion is now seen by the neighbor pixel. This way, that pixel (indicated with red color) begin to see the color of multiple features (i.e., various colors) and reads the average of them unless it is subjected to noise. The received intensities on the deformed image that is seen in Figure 2-3 do not include the same features; accordingly, the current point may not be detected clearly. Tracking the whole subset rather than a single-pixel provides more information about the movement that makes it easy for detecting such small shifts.

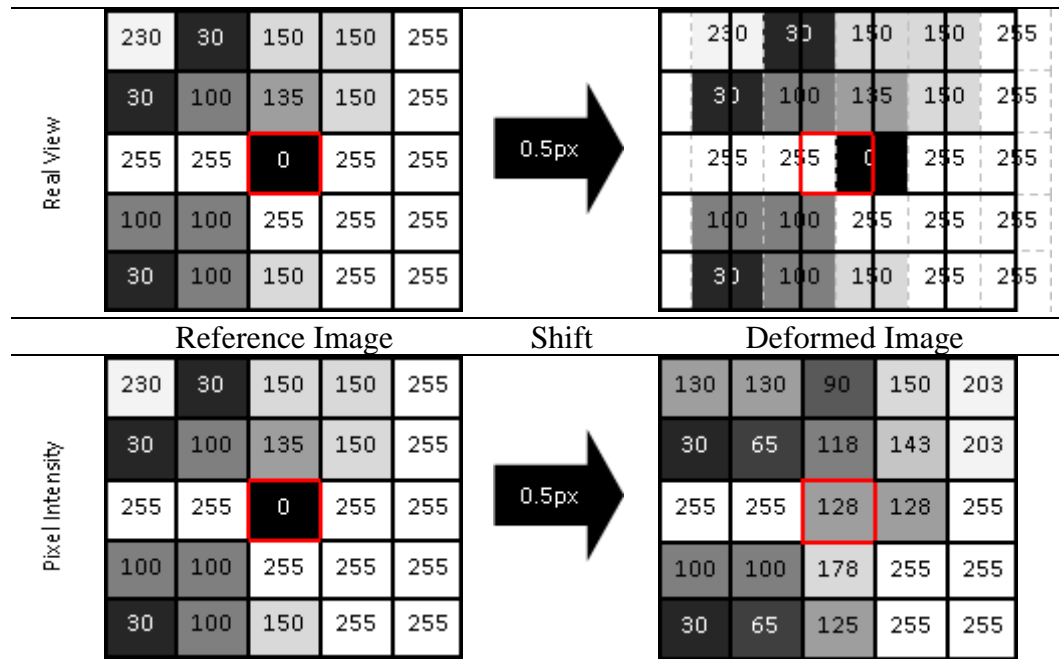


Figure 2-3 Single Pixel Tracking Example

This is actually the main idea behind the DIC method. Instead of tracking a single point, the DIC method aims to find the new location of the facets on the deformed image by either using cross-correlation or least squares method (Romeo, 2013). In the cross-correlation approach, the facet in the deformed image is searched in the reference image by moving it in a particular search area that may be two or more times greater than the facet size and the location having the highest correlation coefficient is considered as the new location of that facet. The main disadvantage of the cross-correlation method is that it can only capture rigid body translation of the facet, the deformation or rigid body rotation of the facet cannot be captured.

The least-square method (Equation 2.1), on the other hand, can capture both translational and rotational movement of a facet. Moreover, changes in illumination and geometric distortions (deformation of the facet) can be handled with two additional parameters, r_0 and r_1 , respectively. In Equation 2.1, f and g are the reference and the deformed images, respectively, x_i and y_i are the coordinates of a point, and x_t and y_t are the coordinates of the new location of the same point, which are computed

by polynomial fit equations given in Equations 2.2. and 2.3. This method tries to find polynomial parameters (a_j) and transformation parameters (r_j) to minimize the total error by considering each pixel in the facet. The total number of pixels in the facet is represented with the letter n . Since the equation is not linear and it can be solved by an iterative method like Newton Raphson, this approach is much more time consuming; nevertheless, it gives more accurate results than the cross-correlation method (Romeo, 2013).

$$\min \sum_{i=1}^n |f(x_i, y_i) - (r_0 + r_1 g(x_t, y_t))|^2 \quad (2.1)$$

$$x_t = a_1 + a_2 x_i + a_3 y_i + a_4 x_i y_i \quad (2.3)$$

$$y_t = a_5 + a_6 x_i + a_7 y_i + a_8 x_i y_i \quad (2.4)$$

2.3. A Novel DIC Methodology for Small Deformations Governing in a Long Duration

There are several challenges to measure small deformations for a long duration of time accurately. Measuring shrinkage deformations at the surface of a concrete specimen is a very good example of such a problem. Shrinkage deformations occur at a prolonged rate (approximately 45 $\mu\text{E}/\text{day}$) and continue for a long duration, up to years. During that time, experiments should be conducted in an isolated, controlled environment free of noticeable vibrations and without considerable temperature and moisture variations that can influence the experimental results as well as measurement-setup. In addition to these, shrinkage deformations are very small in magnitude in the order of μE , which occurs at the whole volume; thus, measuring deformation at certain points would provide very limited information.

Considering all these challenges, the DIC method is very attractive since it can provide a surface deformation pattern with respect to time, but current on the shelf DIC measurement instruments do not provide sufficient sensitivity for such measurements.

Moreover, they are not suitable for collecting data for a long duration of time, such as days or weeks. Because of these reasons, a novel measurement method based on DIC that uses high-resolution DSLR cameras is proposed. This method can be utilized not only for shrinkage experiments but also for experiments with a slow rate of deformation that requires displacement measurements in the range of μm . The main steps of the proposed method are presented in Figure 2-4. The method has three main steps, i.e., pre-experiment preparations, image acquisition during the experiment, and post-processing the experimental results.

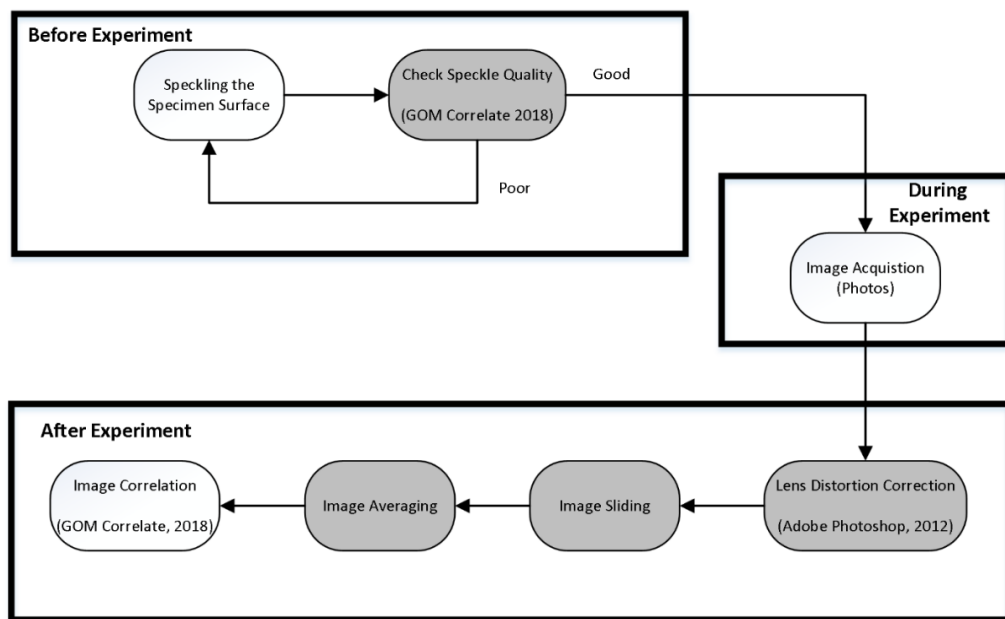


Figure 2-4 Flow Chart of DIC Measurement Process

The most important step before the experiment the way the region of interest is painted in speckles. Quality of the speckle pattern is crucial to obtain reliable and accurate results. In order to assess the quality of a speckle pattern, the pattern quality feature of the GOM Correlate (2018) software is utilized. This software is also used for processing the images for computing the displacements. According to our experience,

raster points having a quality value 3 or higher can be tracked accurately throughout the whole duration of the experiment. Thus, before initiating the experiment, the quality index of each raster point is computed for a sample image, and if the quality of the pattern is not satisfactory, the speckle pattern is regenerated until an acceptable pattern is obtained.

Benchmark images provided by the Society for Experimental Mechanics, SEM (2014) are utilized to illustrate the effect of the quality assessment approach. These benchmark tests involve translation, rotation, and different strain conditions with various speckle pattern qualities and illumination conditions. As presented in Figure 2-5, two sample patterns, named as Sample3 and Sample4 by SEM (2014), were chosen, and the average quality value of the pattern was calculated for randomly selected 20 raster points. In both cases, the specimens undergo rigid body translation and the specimens move 0.1 pixels in both horizontal and vertical directions at each step. The samples involve 11 images and they undergo 1 pixel total translation in both directions. The images of Sample3 have a mean quality value equal to 4.31, thus have acceptable speckle pattern quality. In this case, the translation in both directions could be fully tracked within an error of less than 3.5%. In the case of Sample4 whose mean quality value is equal to 1.13, however, most of the raster points could not be fully tracked and errors at the points that could be tracked are as high as 20%.

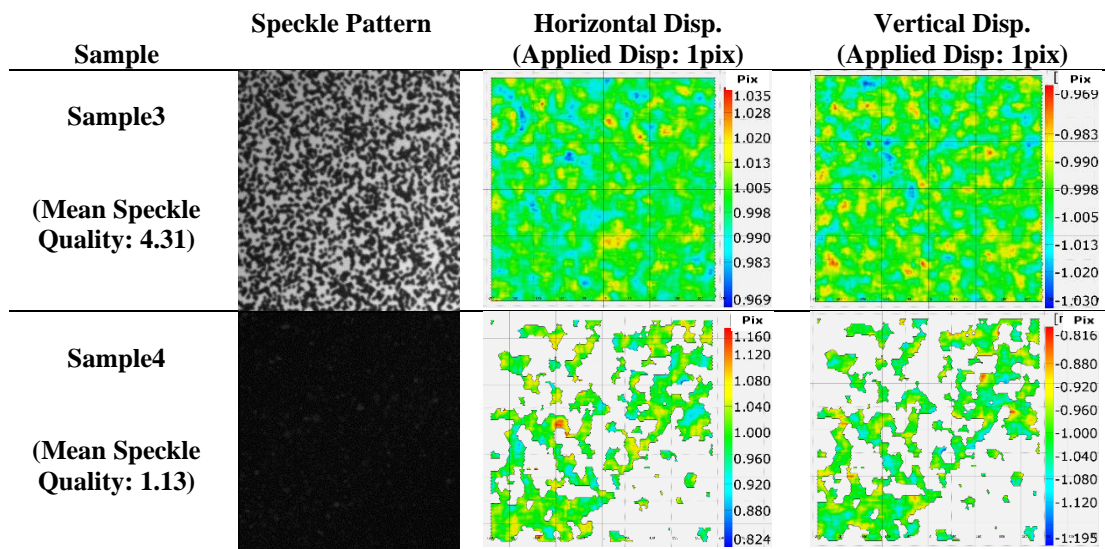


Figure 2-5 Pattern Samples (SEM, 2014) and GOM Correlate (2018) Pattern Quality Average Values

It is very common to use images captured by video recordings. There are two problems with this approach. Using videos for long-duration measurements would require large storage capacity and significant computation time for post-processing. Furthermore, such images can have in the range 4-8 MP resolution, which would either reduce the size of the region of interest or increase the magnitude of the smallest deformation that can be accurately measured. Because of these reasons, the images can be acquired as photos by using DSLR cameras. In the experiments, Nikon D5200/D5300 with 24 MP resolution (Appendix A) was utilized. This approach, on the other hand, requires additional post-processing of images before correlation to reduce the errors in the measurements. These additional post-processing steps are named as Lens Distortion Correction, Image Sliding Correction, and Image Averaging (Figure 2-4).

The effect of lens distortions on the image-based measurement can reduce the accuracy of the results. There are several lens distortion models such as spherical, coma, astigmatism, etc., and each of them has different lens distortion based parameters that need to be determined. Considering all the distortion models together makes the distortion equation as highly nonlinear; thus, the solution may converge to incorrect points if the initial values are not set accurately. Because of this reason,

considering only one or two distortion models is suggested for lens distortion corrections to obtain reliable results (Sutton et al., 2009). In this study, the lens distortions were corrected by using Adobe Photoshop CS6 (2012), which utilizes predefined distortion models for various DSLR lenses, which are geometric, chromatic aberration, and lens vignette corrections.

The main disadvantage of taking photos with DSLR cameras instead of recording videos is the mechanical vibration caused by the shutter mechanism. Such vibration may cause a small rotation or a small shift in the camera view in any direction, even if the camera is fixed properly. Thus, the effect of such a movement should be eliminated in every image. This step of correction is named as “Image Sliding Correction.”

For this purpose, several target objects are located on fixed objects in the setup. These target objects can include either checkerboards or crosses that would be the reference for the Image Sliding Correction which could be done by feature tracking algorithms (Figure 2-6 (a)). Alternatively, random speckle patterns can be painted on the surfaces of fixed target objects and randomly selected raster points on this pattern can be considered as fixed points and tracked by utilizing the DIC algorithm (Figure 2-6 (b)). These two options were tested, and after a series of experiments, it was understood that using a random speckle pattern is a much better option to track shifting or rotation of the camera. Furthermore, from these experiments, it was experienced that performing correction for the rotations less than 0.01° does not give any benefit; on the contrary, it causes more damage in the images. Such tiny rotations result in translation much smaller than 1-pixel size for the pixels being close to the rotation center. Representing such minor translations in a discrete environment may lose the characteristic feature of a particular speckle.

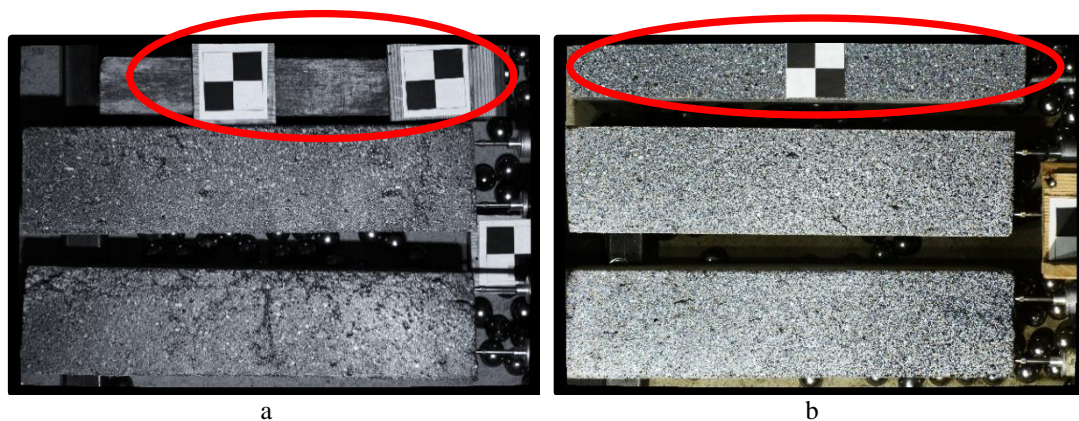


Figure 2-6 Target Objects (a), Target Pattern (b)

As a final step, Image Averaging Method (Su et al., 2015) is utilized to minimize the noise on images. At each image acquisition period, multiple images are taken. Then, by taking the average pixel intensity values of these images, a new and less noisy image is obtained. It should be noted that to benefit from this noise reduction method, the deformation or the movement of the specimen should be negligible for that image acquisition period. Alternatively, using higher exposure instead of applying the Image Averaging Method can be preferred, which reduces the noise on images also. In this case, the camera takes an average of the pixel intensities itself while collecting light of the sensors at a particular image acquisition period. However, if the shutter mechanism related vibrations continue for a while, the image would be blurry. Image Sliding Correction, however, would handle such vibrations in the case of the Image Averaging Method. That is why image averaging is preferred instead of using high exposure.

2.4. Validation of the Proposed DIC Measurement Method

The proposed DIC measurement methodology was tested in three different experimental projects, surface deformation measurement at uniaxial compression test of plain concrete, three-point bending test of a reinforced concrete beam, and reinforced concrete pressure tunnel lining. Each experiment challenged the proposed

DIC measurement method in a different way; however, for all experiments, the measurement results were compared with the results of other measurement equipment. This way, the reliability of the DIC measurement was questioned.

2.4.1. Experiment 1: Concrete under Uniaxial Compression

Uniaxial compression test of a concrete sample covers validation of DIC measurement technique for catching minor cracks on surface by capturing photo with a high-resolution DSLR camera. For this purpose, a rectangular-shaped concrete specimen was prepared such that one face of it was speckled for DIC measurement. Then, it was subjected to uniaxial compression by applying displacement increment in the uniaxial direction until it failed. Measurements were conducted via DIC method and displacements were compared with the applied ones. DIC strain localizations, on the other hand, were compared with another methodology called Eulerian Video Magnification (Wu et al., 2012) which detects and magnifies the minor/invisible changes in back to back captured images to make them visible.

2.4.1.1. Experimental Setup

A cubic concrete specimen, prepared according to ASTM standards (15 cm in each dimension), was divided into four pieces (7.5 x 7.5 x 15 cm) (Figure 2-7). One-piece was speckled and tested under uniaxial compressive loading. The vertical displacement and strain distributions on the speckled surfaces were computed using the DIC method. Furthermore, the vertical displacement measured at the center of the bottom end of the specimen was compared with the applied displacements.



Figure 2-7 Concrete Specimen (one-quarter of the cubic specimen)

In this experiment, images were captured by using Nikon D5200 DSLR camera (Appendix A) with the configurations displayed in Table 2-1. The camera was connected to a desktop computer that controlled the whole process of image capturing, such as timing for photo shooting and transferring/storing the captured images, etc.

Table 2-1 Camera Configuration Parameters

Nikon:	D5200
ISO:	2000
Aperture:	f/25
Shutter Speed (sec.):	1/160
Focal Length (mm):	105
Scale ($\mu\text{m}/\text{pixel}$):	44.7

Lens distortion in each image was corrected by utilizing Photoshop software (Photoshop, 2012), firstly. Then, the image-sliding correction was performed since there were significant shifts, almost 2 and 4 pixels in horizontal and vertical directions, respectively. This shift can be observed in Figure 2-8 that when the first and the last images are superimposed in a single image, the fixed objects are seen as blurry because they are not at the same location anymore.

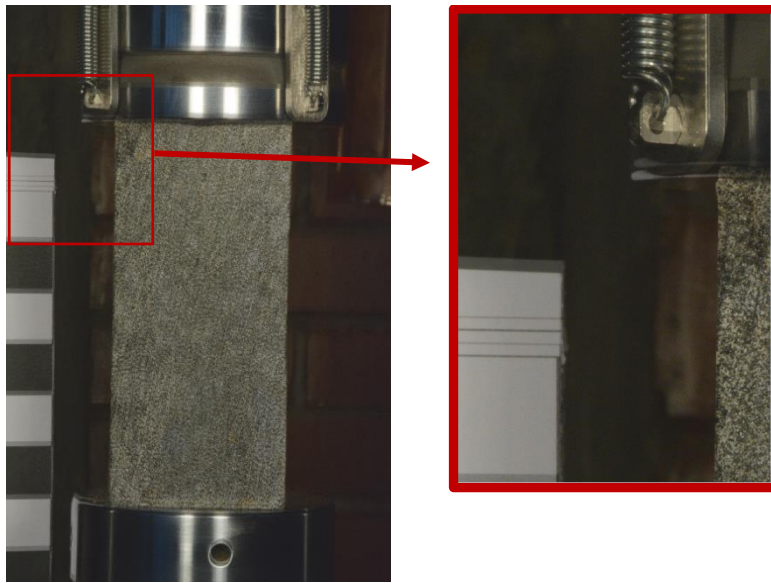


Figure 2-8 Example Image Shift on Images

During the experiments, images were captured at 5 seconds time intervals. In each interval, three images were captured to reduce the noise that occurred on the images by performing an image-averaging process. The averaged images, then, were inserted into GOM Correlate software (*GOM Correlate*, 2018) for the correlation process. By selecting 88,106 raster points and 19-pixel sized facets, displacement and strain distributions were obtained. Moreover, the Eulerian Video Magnification method, which is a particular method for tracking the changes between back to back images and magnifying them to become visible, was applied to the averaged images and obtained results were compared with DIC measurements.

2.4.1.2. Comparison of Results

The concrete specimen was subjected to uniaxial compression until it failed. Although the force was applied with a small displacement increment, it failed suddenly, i.e., no visible crack was observed just before the failure, and the measurement surface dropped as a whole suddenly. Accordingly, DIC measurement could be conducted until the failure state, and no plastic behavior was observed from the vertical

displacement distribution with respect to the time shown in Figure 2-9. Although maximum displacement was measured at the bottom of the specimen, which is approximately 1.2 mm, it was subjected to almost 0.5 mm relative displacement just before the failure.

The applied and measured vertical displacement at the bottom end were drawn in the same figure (Figure 2-10). In this figure, DIC measurements from original images (called “DIC-Orig”) and corrected ones against image-sliding (called “DIC-Corr”) are shown together. The vertical shift in the original images (not corrected against shift) resulted in an approximately 11% displacement error. The trend of the line of the corrected images, on the other hand, is quite similar to the applied ones until the failure.

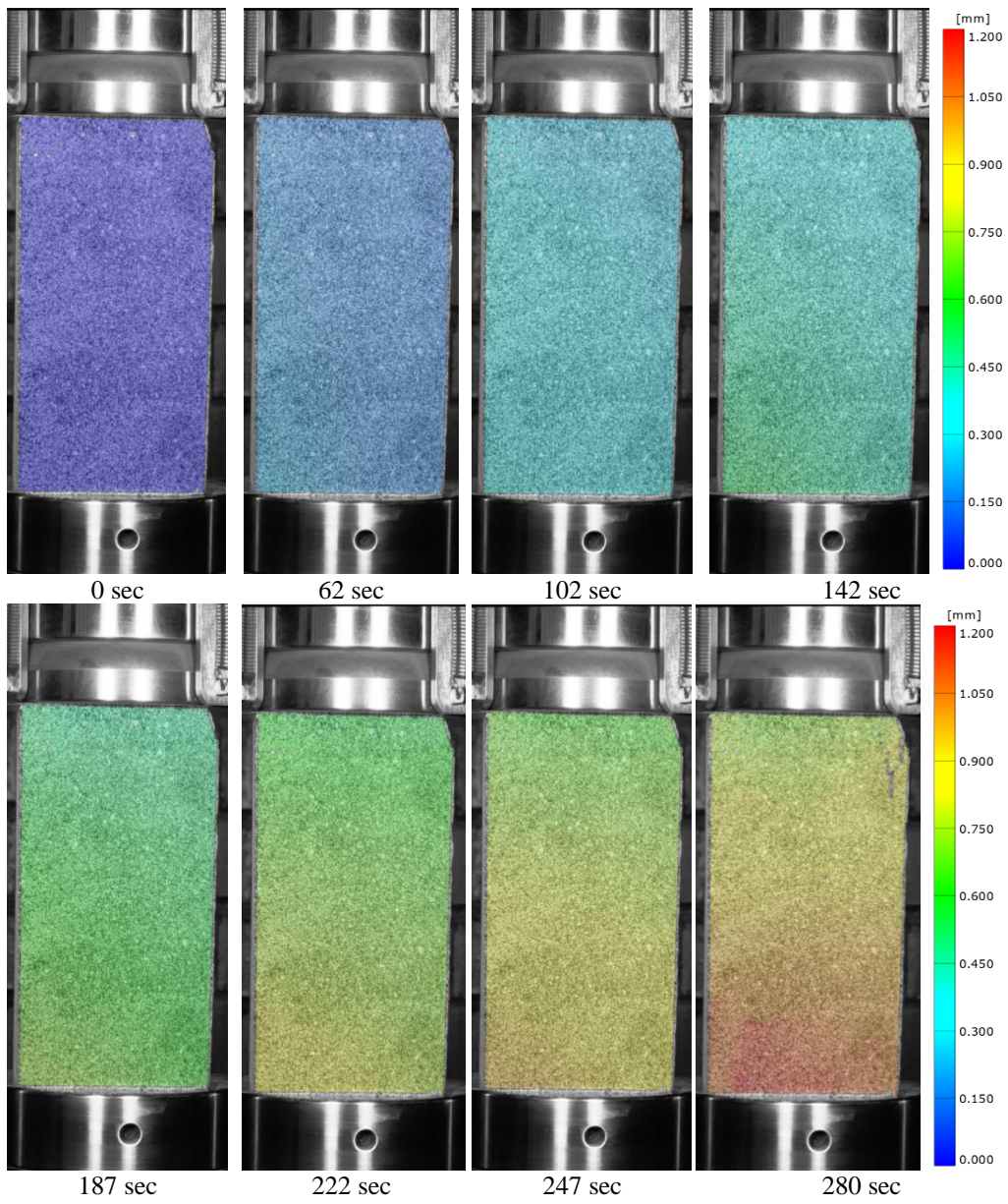


Figure 2-9 Vertical Displacement Distributions

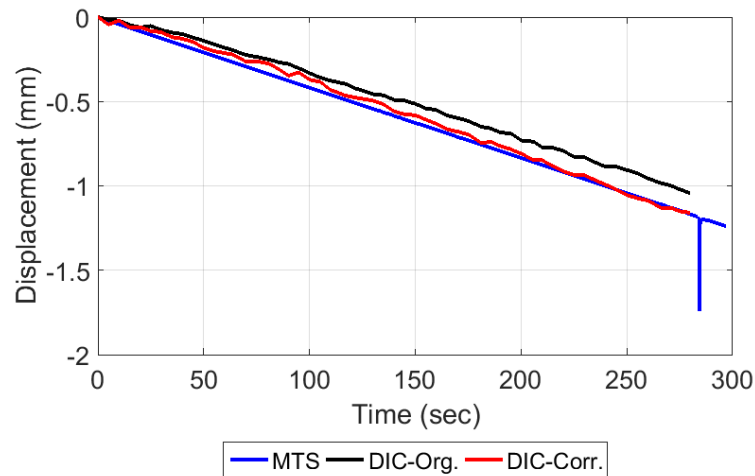


Figure 2-10 Vertical Displacement at Bottom End

Vertical displacement results show that the deformation-time relation was linear until the failure. In Figure 2-11 (a) and (b), the images just before and after the failure is presented, respectively. Until the failure state, the first principal strain distribution that was calculated by utilizing the DIC tool shows the strain localization regions (represented by red color in Figure 2-11 (c)) even though they could not be detected with the naked eye. These local strain branches indicate the potential cracking pattern just before the sudden failure. Furthermore, the same images were input into the Eulerian Video Magnification tool. It indicated the moving regions (i.e., detected changes with respect to the previous image) with pink color (Figure 2-11 (d)), whereas it did nothing for the remaining regions. Thus, change in color represents discontinuous deformations (i.e., cracks). It provided the same discontinuous deformations pattern also. This proved that the proposed DIC method could measure the localized strains successfully even they were not identified by naked-eye.

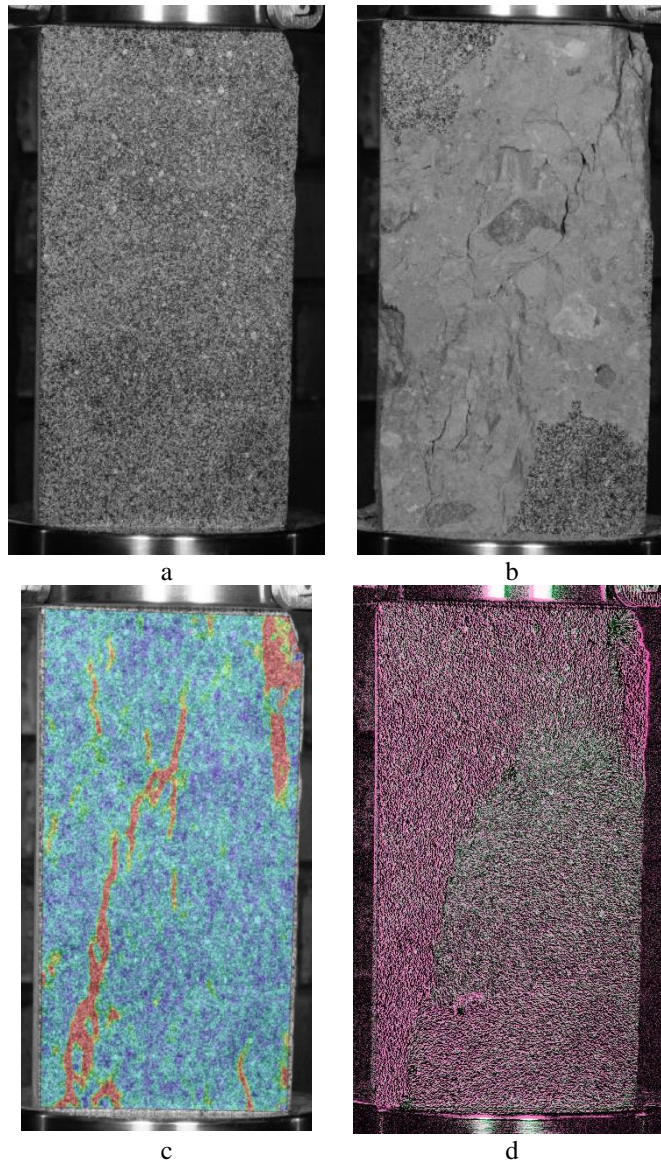


Figure 2-11 Experimental Results. Final Image Captured just before the failure (a), Final Image at the end (just after the failure) (b), DIC - First Principal Strain (just before the failure) (c), Video Magnification Method (just before the failure) (d)

2.4.2. Experiment 2: Three-Point Bending Test of RC Beam

In this project, a simply supported reinforced concrete beam was subjected to three-point flexural test (Albostan & Kurç, 2016). The beam had a rectangular cross-section whose dimensions were 0.3 and 0.4 m in width and depth, respectively, and the span length was 3 m (Figure 2-12 (a)). It was supported at its both ends in such a way that one side was pinned, whereas a roller was used for the other side. Force was applied by utilizing a hydraulic piston at the mid-span of the beam in the direction of gravity.

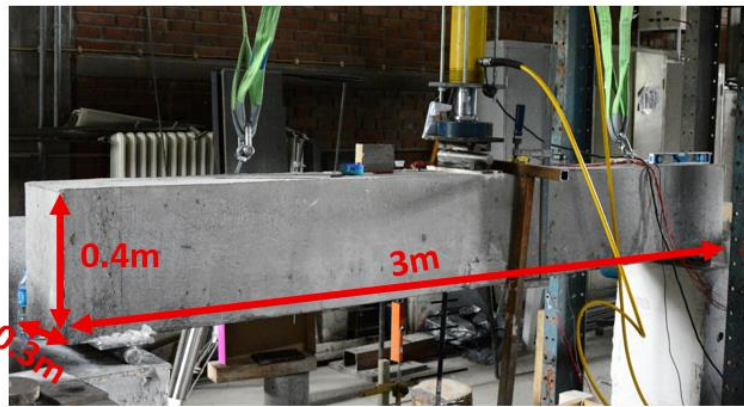
2.4.2.1. Experimental Setup

One side of the beam was speckled by using black and white spray paints for DIC measurement in such a way that homogenous and randomly distributed speckle pattern was obtained. A single camera was focused on a region at the mid-span of the beam. By using Nikon D5200 DSLR camera in photograph mode (Table 2-2), deformations at a region of interest (ROI) having 1.4 x 0.4 m dimensions were measured. In this experiment, 1-pixel length corresponded to 232 μm on the specimen.

The camera was placed in such a way that the normal vector of the specimen surface was perpendicular to the sensor plane (Figure 2-12 (b)). Images were captured at every 8 seconds time intervals. Within this time interval, three images were consecutively taken. This 8-seconds delay between each image acquisition process was basically the time required for the camera to convert sensor data of these three images to raw image format and transfer them to the computer. After the test, these three images were used during the image-averaging correction step.

Table 2-2 Camera Configuration Parameters

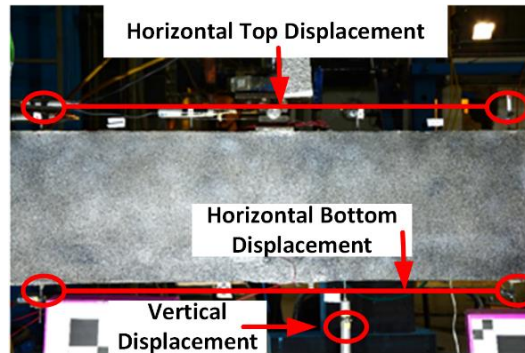
Nikon:	D5200
ISO:	100
Aperture:	f/6.3
Shutter Speed (sec.):	1/25
Focal Length (mm):	35
Scale ($\mu\text{m}/\text{pixel}$):	232



a



b



c

Figure 2-12 Experimental Setup (a), DIC Systems (b), LVDT Locations (c)

In order to verify the displacement measurement of the proposed method numerically, three classical displacement measurement instruments, LVDTs, were also set (Figure 2-12 (c)). One of them was set at a point close to mid-span in such a way that it measured vertical deflection of the beam. The other two were placed on the beam, and they measured displacements in the horizontal direction at the top and bottom layer of the beam. Indeed, they measured the relative horizontal shortening/elongation

between two points with a distance of approximately 1.2 m. To measure relative displacement between two far points, LVDTs can be set with a rubber band and thin wire. The used LVDTs' rods can move in compression direction only from the rest; therefore, they have to be compressed as required amount initially to measure elongation. Thus, the rods of the LVDTs which had been set one of the reference points were compressed fully with a rubber band. Then, the wire was connected between the rod and the other point, and it was stretched. The top face of the beam would be shortened due to bending; accordingly, the wire of the corresponding system was stretched so that the pre-compressed rod returned its original position (i.e., no force on the rod). When the points went closer to each other due to loading, the tensile load on the wire would reduce and the rubber band would pull the rod back, i.e., it would read compression. The bottom face, on the other hand, would be subjected to elongation; thus, the corresponding wire was stretched up to releasing the rod a little. While the beam face elongates, the tensile force on the wire would raise and push the rod in the forward direction. In other words, it would measure elongation as expected.

A single point load was applied to the mid-span of the beam in the direction of gravity by using a hydraulic piston. The beam was loaded twice. In the first loading scheme (called LS1) was applied in three steps up to the 3, 5, and 7 tons, respectively, which would not cause any inelastic deformation. The beam was then loaded until it lost load carrying capacity (LS2). In this case, the beam was loaded up to 27.8 tons twice, which resulted in significant cracks on the beam. Loading schemes for both cases are presented in Figure 2-13.

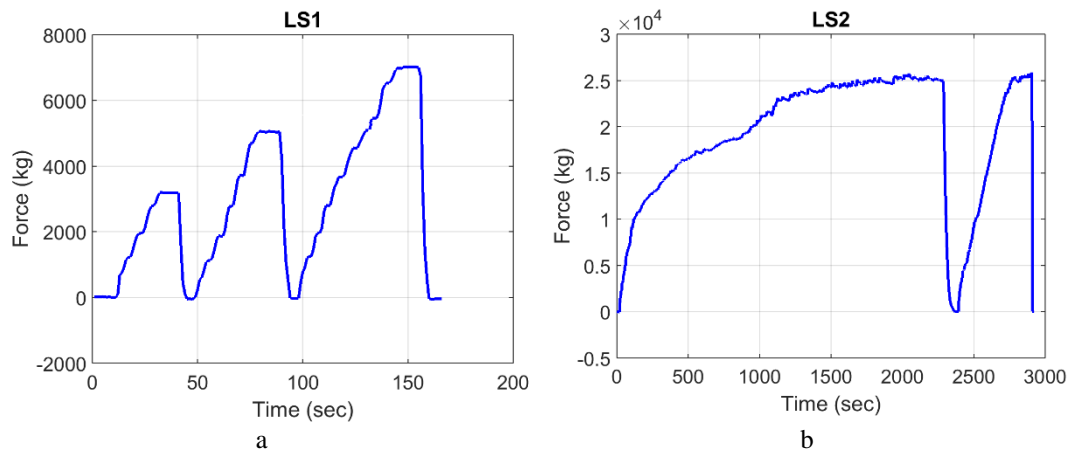


Figure 2-13 Loading Schemes. LS1 (a), LS2 (b)

Like the previous experiment, images were corrected against lens distortion, camera vibration, and image noises consecutively. Then, displacements and strains at equally spaced (10 pixels distance for each) 115,185 raster points were calculated by tracking 30-pixel sized facets.

2.4.2.2. Comparison of Results

For LS1 loading, horizontal and vertical displacements, first principal strains, and the corresponding deformed image under 7 tons are presented in Figure 2-14. Horizontal displacement distribution shows that the top of the beam was subjected to compression, whereas the bottom layer elongated. The maximum vertical displacement was at the mid-span of the beam, which can be seen in vertical displacement distribution, clearly. These two results are as expected, except the discontinuity in horizontal displacement distribution at mid-span. This discontinuity in the displacement field is due to a flexural crack at the mid-span. This crack can be clearly observed in the first principal strain distribution. The red color indicates maximum tensile strains which shows the possible location of cracks. There is no visible crack at the end of LS1 loading.

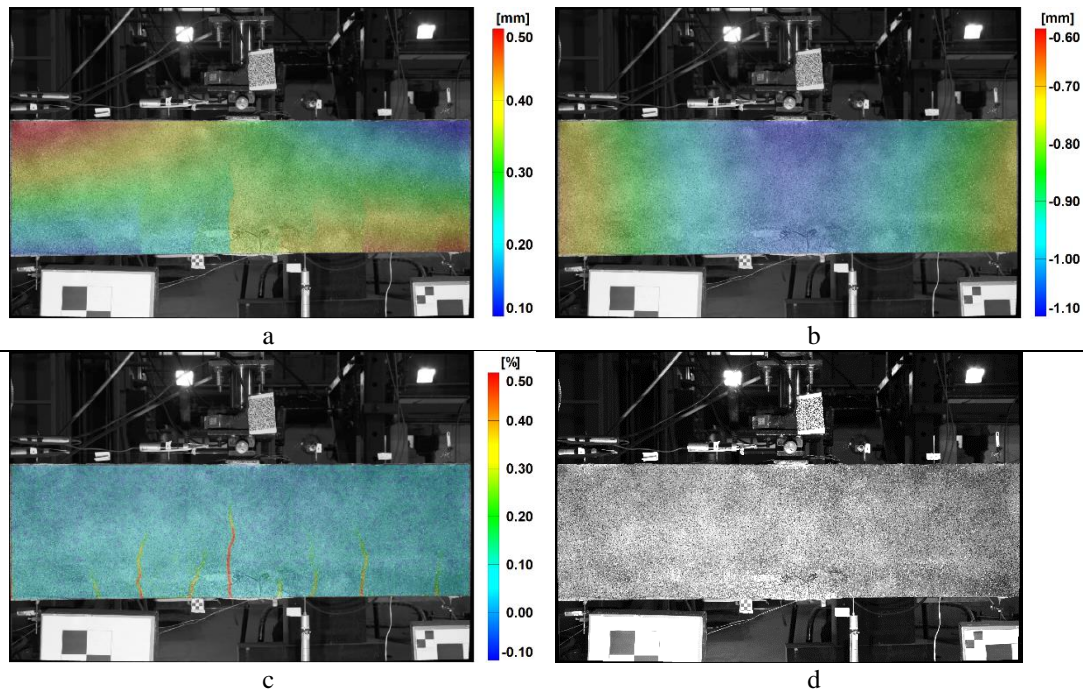


Figure 2-14 Displacement and Strain Distributions under Load of 7 tons. Displacement Distribution in Horizontal Direction (a), Displacement Distribution in Vertical Direction (b), First Principal Strain Distribution (c), Final State (d)

The measurement results with LVDT and DIC measurements were compared numerically. From the DIC measurements, the closest points to the LVDT instruments were selected and their displacements were plotted at the same graph with the corresponding LVDT readings (Figure 2-15). Both measurement techniques measured the same vertical displacement (Figure 2-15 (a)). There are significant differences in horizontal top displacement readings (Figure 2-15 (b)). The expected top displacement under 7 tons was calculated as $378 \mu\text{m}$ for the linear elastic case, which is closer to the DIC measurement. This situation implies that the LVDTs could not measure small displacements in compression properly by connecting them with rubber and thin wire. On the other hand, for bottom displacement measurement in the horizontal direction (Figure 2-15 (c)), the error limit of the DIC tool is the main reason for the difference seen in the figure.

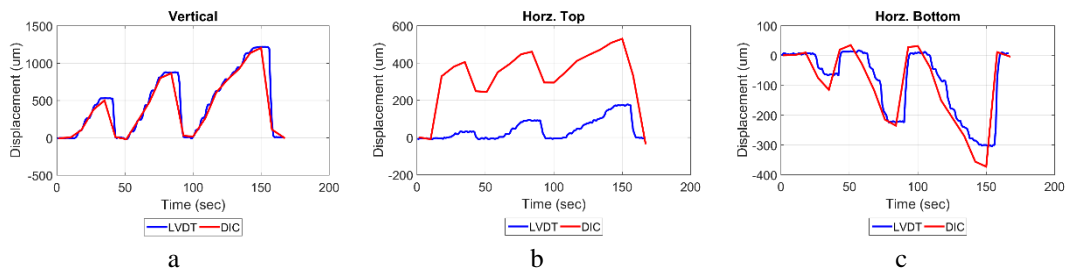


Figure 2-15 Displacement Plots. Vertical Displacement (a), Horizontal Displacement at Top (b), Horizontal Displacement at Bottom (c)

For LS2 loading, DIC displacement and strain distributions under 27.8 tons are presented in Figure 2-16. Displacement distributions are similar to the previous case except for the cracking patterns. At the visible crack regions, the correlation could not be conducted since there were no speckles at these regions. Because of this reason, there are no color contours at the location of visible cracks. The first principal strain distribution can clearly show the possible crack location where localized tensile strains are observed. Figure 2-16 (d) shows the visible cracks after the test and there is a one-to-one correspondence between the possible locations of cracks at the first principle strain distribution and the actual location of cracks. This shows that DIC measurements can locate the visible cracks as well as the ones that are not detected by naked-eye.

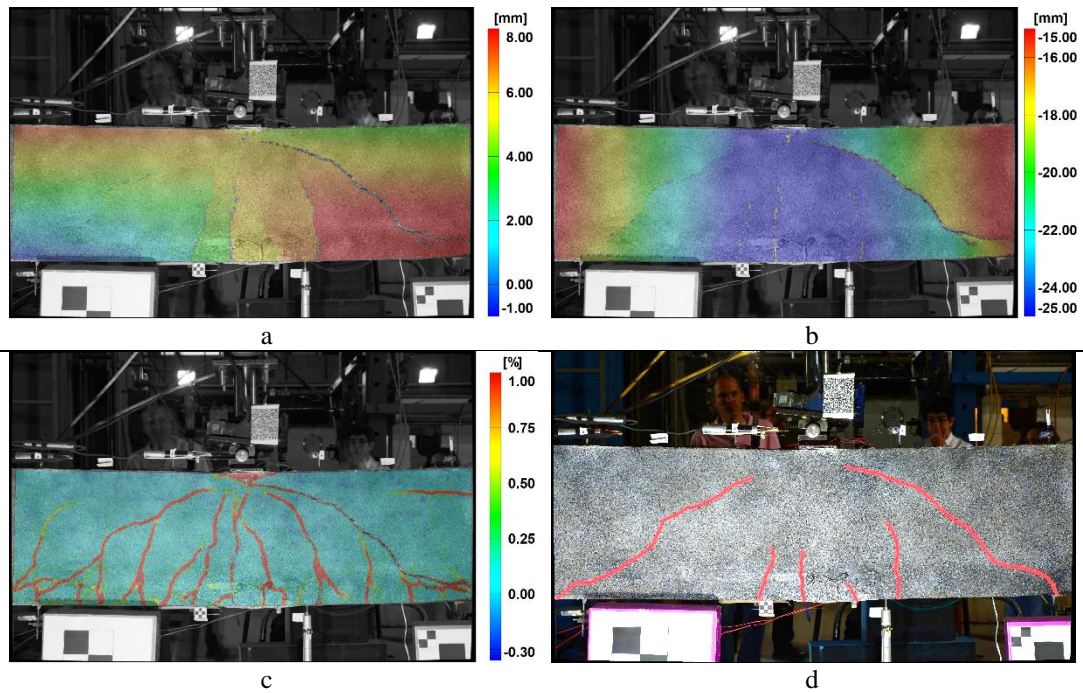


Figure 2-16 Displacement and Strain Distributions under Load of 27.8 tons. Displacement Distribution in Horizontal Direction (a), Displacement Distribution in Vertical Direction (b), First Principal Strain Distribution (c), Visible Cracks (d)

In addition to the contour plots, numerical values of displacements were compared with the LVDTs' measurements (Figure 2-17). Although the vertical displacements are very close to each other, there are minor differences in horizontal displacement plots towards the end of the experiment. The main reason for this difference is the rotation of the measurement axis of the LVDT due to large vertical displacement.

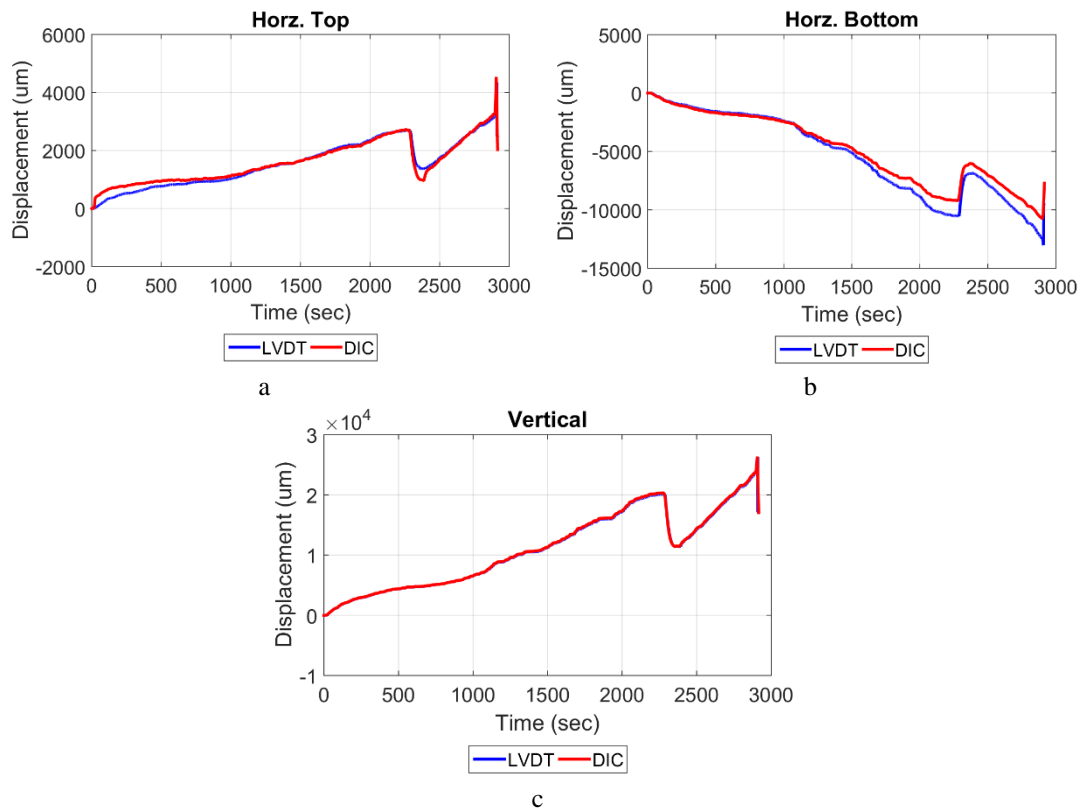


Figure 2-17 Displacement Plots. Horizontal Displacement at Top (a), Horizontal Displacement at Bottom (b), Vertical Displacement (c)

2.4.3. Experiment 3: Reinforced Concrete Pressure Tunnel

The experimental study covers examination of tunnel lining behavior subjected to horizontal and vertical stresses and the contact between the lining and the rock body (Kalaycıoğlu et al., 2018). For this purpose, a novel two-dimensional tunnel testing setup considering in-situ stress state was constructed in the Mechanics of Structure Laboratory in METU in such a way that 0.4 times scaled model of a horseshoe-shaped reinforced concrete tunnel was built inside a masonry structure resembling a rock body. By acting internal hydrostatic pressure to the tunnel lining, deformations occurred on the structure was examined. Displacements and deformations were measured from specific points by using LVDTs and strain gauges, respectively. In addition to them, the DIC method was utilized to visualize strain localization on the lining, contact, and the rock body. Since the setup was relatively large and the

expected deformations would be rather small, more than one camera was utilized in such a way that each one would focus on different portions of the structure and would shoot simultaneously. At this point, the challenge for the proposed DIC method was combining the measurements from different camera models having different configurations. Moreover, in this experiment, DIC strain measurements were compared with the strain gauge readings.

2.4.3.1. Experimental Setup

A novel experimental setup, which was 0.4 times scaled version of the existing pressure tunnel of Topçam Dam in Ordu/Turkey, was constructed as a two-dimensional model such that a 20 cm thick sample was generated. The generated tunnel lining was placed at the center of the rock body, which was built as masonry, and it was compressed by applying pre-tensioning in such a way that it was subjected to uniform compressive pressure in both horizontal and vertical directions (Figure 2-18). The lining was subjected to internal hydraulic pressure from orthogonally located two pistons inside the tunnel.

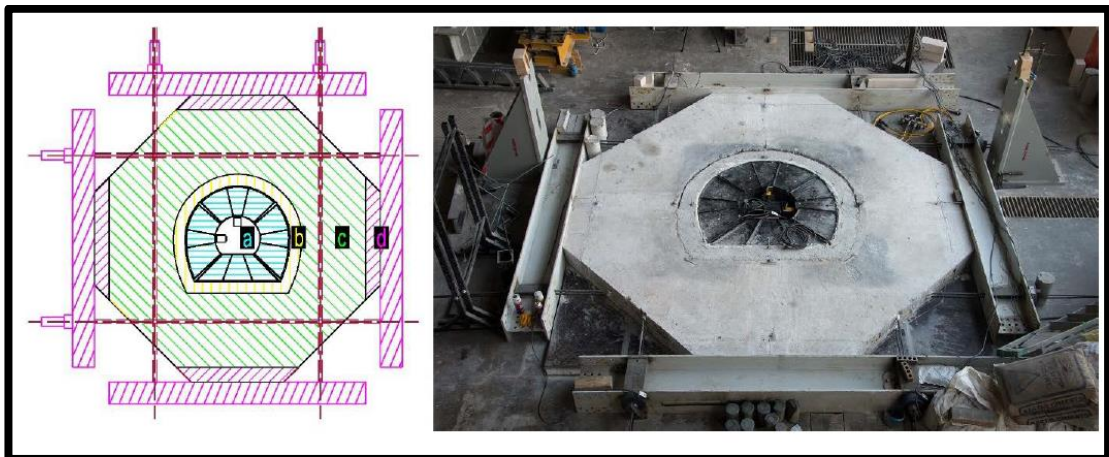


Figure 2-18 Experimental Setup. (Loading Mechanism (a), Lining (b), Rock Body (c), Pre-tensioning System (d))
(Kalaycıoğlu et al., 2018)

A vast amount of LVDTs was located for relative and absolute displacement measurements, and lots of strain gauges were glued to critical strain regions. Locations of both LVDTs and strain gauges are presented in Figure 2-19 in which numbers 1 and 2 indicate strain gauges on the lining and the rock body, respectively. The location of LVDTs are represented with number 3. In addition to these classical measurement instruments, the DIC technique with the proposed methodology was used.

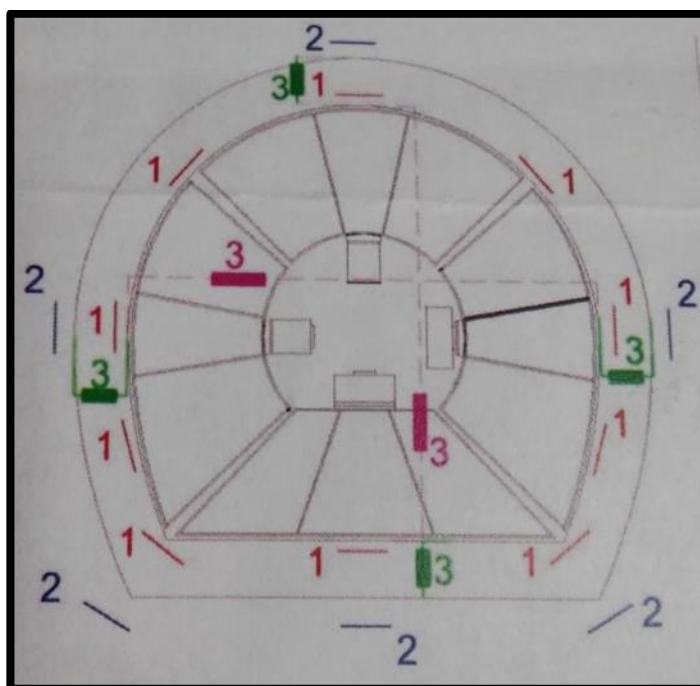


Figure 2-19 LVDT and Strain Gauge Locations

Although almost ten experiments were conducted, only two of them were covered in this study. In the first one, partially confined lining was measured fully by using five cameras in total (four different cameras and/or lens models (Table 2-3)) in such a way that the ROI of each camera coincided with its neighbors (Figure 2-20). This allowed comparing the measurements of different model cameras for the intersection regions. Positioning at different elevations and using a particular configuration for each lens

type provided a variation of ROI's sizes. Accordingly, one camera was able to focus on almost half of the lining, whereas the other four together covered the remaining.



- : Camera 1 & 2: Nikon D5200 with AF-S DX NIKKOR 18-105mm f/3.5-5.6G ED VR Lens
- : Camera 3: Nikon D5300 with AF-S DX NIKKOR 18-105mm f/3.5-5.6G ED VR Lens
- : Camera 4: Nikon D800 with AF NIKKOR 20mm f/2.8D Lens
- : Camera 5: Nikon D300 with 18-200mm f/3.5-5.6G ED VR Lens

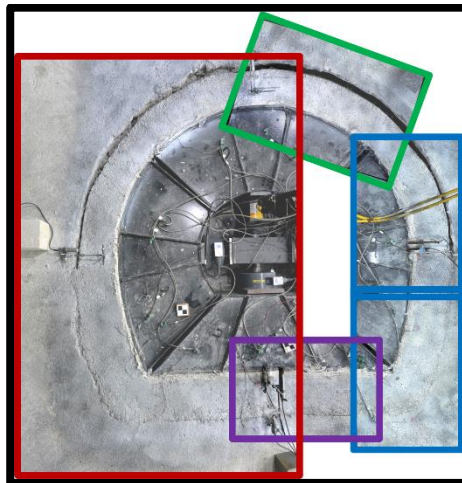


Figure 2-20 Camera Properties, Locations and ROI's

Table 2-3 Camera Configuration Parameters

	Camera 1 & 2	Camera 3	Camera 4	Camera 5
Nikon:	D5200	D5300	D800	D300
ISO:	500	500	1000	500
Aperture:	f/5	f/4.8	f/9	f/6.3
Shutter Speed (sec.):	1/200	1/250	1/200	1/160
Focal Length (mm):	30	42	20	36
Scale ($\mu\text{m}/\text{pixel}$):	156.0 & 154.8	138.4	321.3	269.1

The lining was subjected to internal hydrostatic pressure such that it was increased until it failed. The load was applied by pumping oil by someone as slow as possible to capture all possible failure states. However, controlling multiple cameras by a single computer system was another challenge. Triggering all the cameras simultaneously and receiving images from the cameras immediately would cause excessive data traffic and therefore much delaying time between triggers. Moreover, sometimes, it may result in communication loss. Because of these, only three cameras were connected to the computer system, whereas the other two were controlled by itself. Even this way, at least 5 seconds delay was required to transferring only a single image from each camera. Accordingly, not to extend delays between triggers, the methodology, capturing multiple images and averaging them (image-averaging), could not be applied. Each camera shot only one image simultaneously for each 5 seconds time interval.

In the second experiment, on the other hand, was about a fully confined lining. This time, only two identical cameras (Table 2-4) were focused on the bottom corners of the lining and the rock body since stress localization would occur in those regions (Figure 2-21). Because of this reason, two strain gauges, one is for lining and the other for rock body, were glued at each corner. Strain gauge readings were compared with the DIC measurements for the same gauge length.

Table 2-4 Camera Configuration Parameters

	Camera 1	Camera 2
Nikon:	D5200	D5200
ISO:	100	100
Aperture:	f/10	f/10
Shutter Speed (sec.):	1/8	1/8
Focal Length (mm):	35	35
Scale ($\mu\text{m}/\text{pixel}$):	133.058	130.744

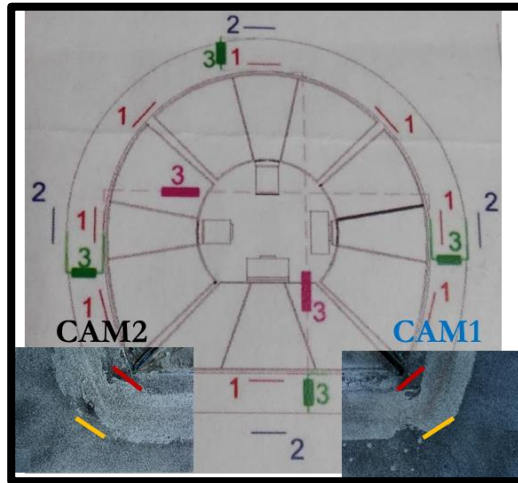


Figure 2-21 Camera ROI's

2.4.3.2. Comparison of Results

Five individual cameras captured images of the entire lining sequentially with 5 seconds time interval. Then the image sets for each camera were processed and correlated one by one, and computed distributions were put in together.

The first principal strain distributions for initial and final states are presented in Figure 2-22 . The final state represents the case in which the lining was subjected to maximum hydrostatic pressure. Accordingly, several regions where strain localized (red color) were observed on the lining, especially on no confinement parts as expected. In such regions, the force could not transfer to the rock body; accordingly, only lining resisted the applied force. For the confinement part, on the other hand, the applied force was easily transferred to the rock body. Thus, only at two significant regions on the lining, bottom corners and end of confinement region, local strains were observed. In addition, measurements stated that the contact layer between the lining and the rock body was subjected to higher deformations.

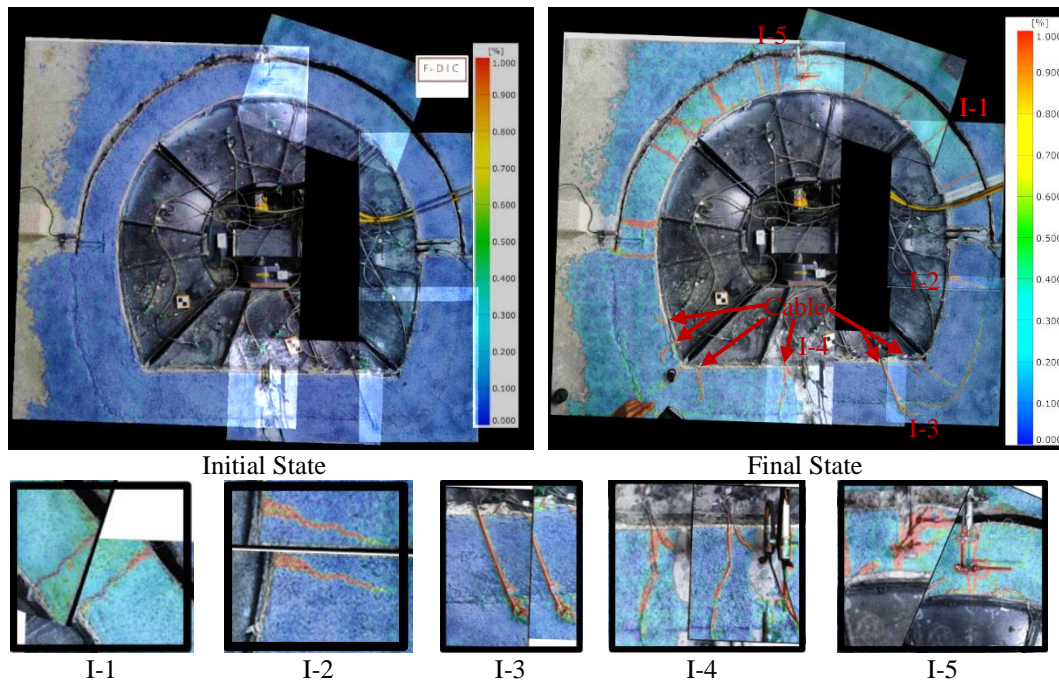


Figure 2-22 First Principal Strain Distributions (Combination of results of all cameras)

The primary outcome which this study focuses on is that individual measurements conducted by using various camera types provided quite similar deformations at the intersection regions. In Figure 2-22, again, the first principal strain distributions obtained from the two distinct cameras for each intersection region (called as I-1 to I-5) are presented. The measured deformations or tracking movement of the cables are quite close to each other, although there are minor differences between both images. These minor differences are related to using differently configured cameras/lenses, which provided different scale amounts and sensitivity in measurements. Thereby, this shows that the measurement technique provides convenient results even for using different types of cameras and lenses.

For the second experiment, on the other hand, two identical cameras measured deformations that occurred at the bottom corners of the lining and the rock body. In those regions, strain gauges also recorded the deformation not only for the lining but also for the rock body. Strain measurements for both methods were plotted at the same figure (Figure 2-23). It can be observed from the lining plots that there is a maximum

strain limitation for strain gauge devices. If this limit is exceeded during the experiment, they stop measurement. Nevertheless, up to those limit points, both measurements are quite close to each other for lining strains. On the other hand, no significant strain occurred on the rock body as expected. This relatively small strain at the right corner of rock (i.e., Cam1 view) was gathered by both measurement systems successively, and their measurements were matched well. However, there is a significant difference between strain gauge and DIC measurements at the left corner of the rock. Indeed, strain gauge readings are a little bit suspicious. Its curve shows that it was subjected to compression for some time, then the behavior went in a reverse direction despite trying to expand the whole structure. This was caused due not to gluing it to the structure properly. DIC measurements, on the other hand, provided similar behavior with the others that were expected.

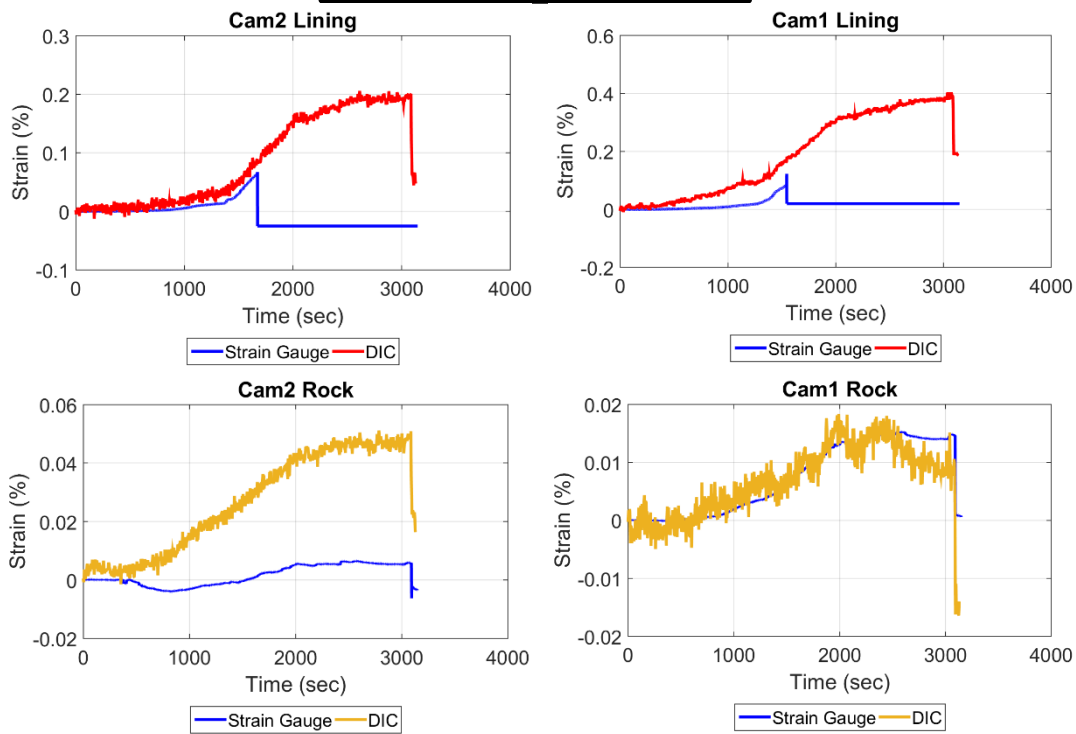
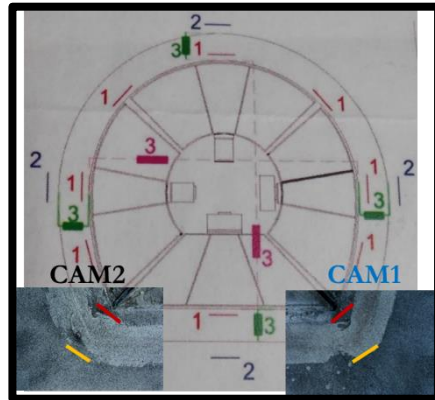


Figure 2-23 Comparison with Strain Gauges Readings

2.5. Summary

Measuring strain distribution on the entire surface of any specimen is more practical with the DIC method instead of gluing many strain gauges. It provides displacement and strain distribution in any direction for the entire surface, and no contact with the specimen is required during the loading. These advantages make the DIC method popular for engineering measurements.

This section covers the fundamentals of DIC theory and a novel methodology, which improves the measurement accuracy significantly, especially for the slowly loaded tests. The methodology is mainly about using high-resolution cameras such as DSLRs in DIC measurements, which provide focus on larger surface areas without losing sensitivity or capability to track much less displacement for the current ROI when images are captured as photos.

The proposed methodology was utilized in three different experiments for validation. The surface deformation of a plain concrete sample under uniaxial compression load showed the localized strain pattern that could not be detected with the naked eye just before the failure. This strain pattern matched with the visible crack pattern that was observed at the end of the test. Furthermore, the obtained localized strain pattern was validated by using the Eulerian Video Magnification tool by inputting the same images to the tool and observing the same deformation discontinuity.

Quantitative displacement validation of the proposed methodology was conducted in three-point bending test of a reinforced concrete beam by comparing it with the LVDT records. Generally, they matched well except for the cases related to the setup of the LVDT instruments. In addition, as in the first experiment, strain distribution of the proposed DIC method provided strain localizations that could not be observed with the naked eye and ended up cracking in the next stages.

Finally, in the reinforced concrete pressure tunnel lining experiment, several cameras that are not identical were used for the proposed methodology to cover the broader ROI. At the intersection regions, similar surface deformation patterns were obtained from the individual. Thereby, this shows that the measurement technique provides convenient results even for using different types of cameras and lenses. In addition, the measured strains via the proposed methodology were compared with the strain gauge records in another experiment set, and similar results were observed if the gauges were glued properly. Furthermore, strain gauges work in a particular strain

range and they could not measure deformations out of that range. In contrast, the proposed DIC method could continue reading.

CHAPTER 3

MEASURING SHRINKAGE DEFORMATIONS OF CONCRETE MEMBERS

3.1. Introduction

Shrinkage of concrete is a complex and long-term process that is considered to continue for many years. Controlling the ambient conditions and taking records for a long-term period without any interruption are some of the major challenges for shrinkage measurements. Recently, focusing on shrinkage induced local deformations and trying to measure those small deformations from relatively larger samples seem to be a challenge for researchers. For these purposes, a novel experimental setup for measuring either free or restrained shrinkage deformations on the entire surface of concrete specimens by utilizing the DIC method is proposed in this chapter.

Standard test setups for the measurement of shrinkage, such as ASTM C157 (ASTM International, 2017a) and ASTM C1581 (ASTM International, 2016a), mainly focus on average length change measured from a single point for free shrinkage case and determination of age when cracking starts due to shrinkage for the restrained case. Shrinkage, however, results in multi-dimensional strain localization mechanisms in a concrete sample that is more complicated. Accordingly, focusing on those local behaviors may provide to understand this mechanism, clearly.

Also, concrete constituents have a rather significant role in shrinkage measurement setup even if it involves only cement, water, and aggregates (fine and coarse). Raising the water-cement ratio (w/c), for instance, accelerates the shrinkage mechanism under standardized environmental conditions (temperature, humidity, etc.) that causes a reduction in measurement duration. Meanwhile, it should gain enough strength to remove from molds and to place in the testing apparatus without causing any damage.

Accordingly, the selection of concrete mix-design is another factor that should be taken into account while designing the experimental setup.

This chapter covers a novel experimental setup about concrete shrinkage deformation measurement in which both LVDT and DIC measurement methods are simultaneously covered. The performance of the test setup is measured by comparing the results of two short-term shrinkage tests. In addition to the shrinkage measurement setup, the properties of the concrete ingredients together with the concrete mix design are also provided. Moreover, compressive/tensile strength and elastic modulus of the hardened concrete are also given in this chapter that will be required for modeling the experiments, numerically.

3.2. Properties of Concrete Constituents and Mix Design

Increasing the shrinkage deformations as much as possible is needed to perform many more tests in a shorter time period. For this purpose, a special concrete mix-design should be prepared by setting a higher water-cement ratio with minimum bleeding. Furthermore, when all constituents are mixed together, shrinkage begins immediately, even if the concrete has not been set yet. Measurement, therefore, should start as early as possible to catch each instance of the behavior. However, it should immediately gain enough strength that is required to remove from molds and to place to the setup without any damage. Another important point is the proportion of the gravels with respect to the concrete mix. Indeed, the concrete should have enough gravels, i.e., local restraints, to observe strain localization clearly.

In the light of these situations, a particular concrete mixture that would shrink excessively in a short time period and would gain enough strength at an early age not to damage the sample while removing molds or placing it to the experimental setup was needed. No chemical admixtures, however, was considered; only the basic constituents, cement, water, coarse and fine aggregates, were taken into account to simplify the behavior as much as possible. To prepare such a mixture that would

satisfy all those conditions, characteristic of all ingredients should be determined, thoroughly.

3.2.1. Aggregates

Limestone based aggregates were obtained from the same quarry in two different size groups, namely 4-12 mm (Figure 3-1 (a)) and 0-4 mm (Figure 3-1 (b)). The XRD spectrum (Figure 3-2) of the aggregates showed that the origin of the rock was Calcite.

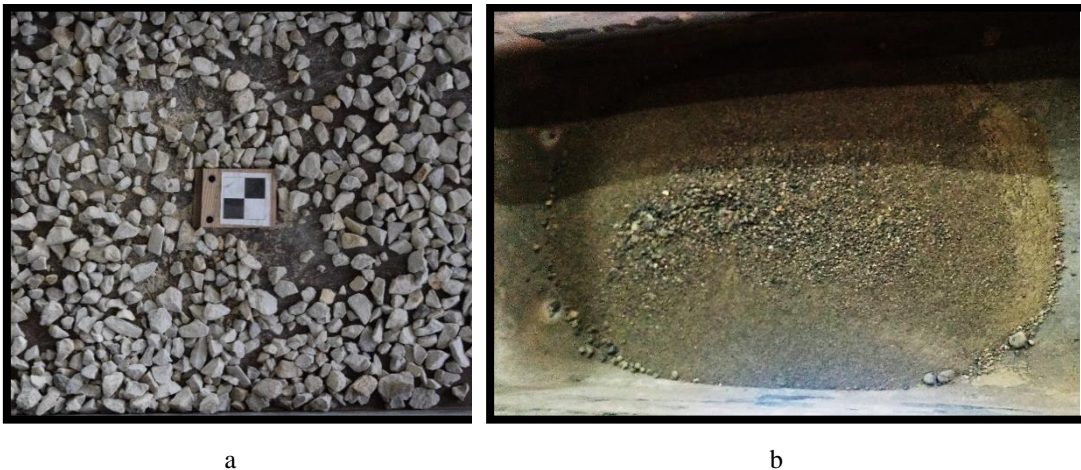
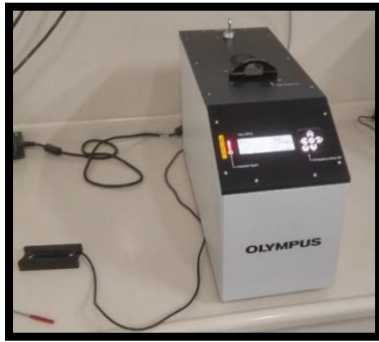


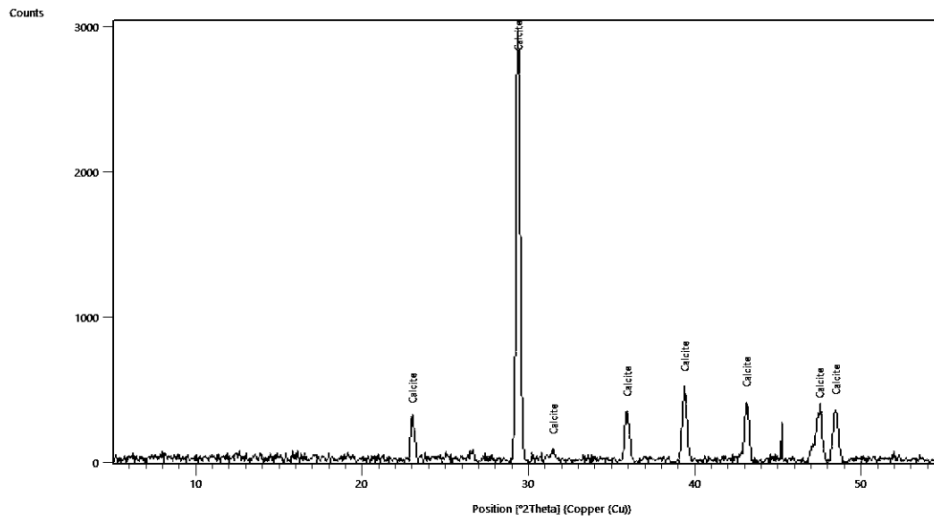
Figure 3-1 Aggregates. 4-12 mm (a), 0-4 mm (b)



a



b



c

Figure 3-2 XRD Device (a), Crushed Limestone Sample (b), XRD Spectrum (c)

To determine the physical properties of aggregates, several standard tests such as sieve analysis, bulk, and relative density, were performed by following the relevant ASTM Standards, namely ASTM C136 (ASTM International, 2014), ASTM C29 (ASTM International, 2016b) and ASTM C127 (ASTM International, 2015a), and ASTM C128 (ASTM International, 2015b). The sieve analysis results of both aggregates are provided in Figure 3-3.

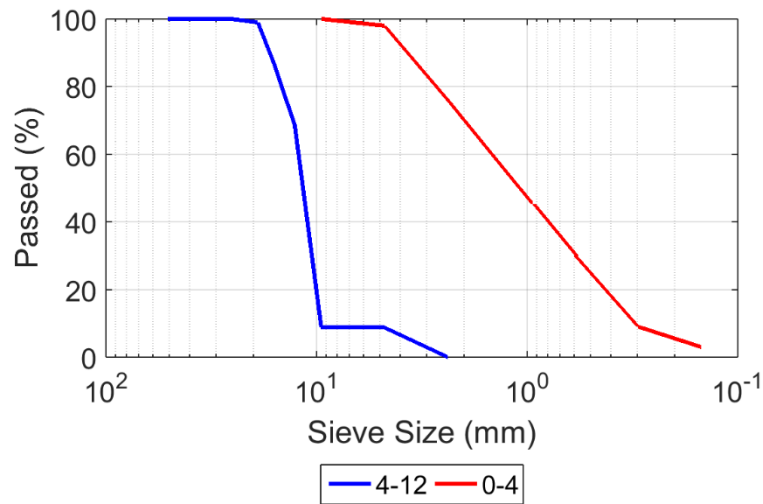


Figure 3-3 Gradation of Aggregates

The specific gravity and the absorption capacity of the aggregates are provided in Table 3-1.

Table 3-1 Granulometry of Aggregate (ASTM C136-06)

	Sand (0-4)	Gravel (4-12)
SSD Specific Gravity (g/ml)	2.54	2.69
Absorption Capacity (%)	4.01	0.76

3.2.2. Cement

As for the cement, a blended cement labeled as CEM II/A-M(V-LL) 42.5 R according to EN197 Standard was used (Figure 3-4). The specific gravity of the cement was determined as 2.98 g/ml using the ASTM C188-09 (ASTM International, 2017b) Standard.



Figure 3-4 Cement

3.2.3. Water

Tap water in Materials of Construction Laboratory of Civil Engineering Department at METU was used for all mixtures.

3.2.4. Concrete Mix Design

Based on the characteristic features of constituents stated above, a special concrete mix design was prepared in such a way that it would experience a high shrinkage deformation in a relatively short time; on the other hand, it would gain enough strength as soon as possible not to damage while removing from molds and placing it to the setup. Moreover, it would contain sufficient gravel proportion to provide local restraints that result in strain localization. No chemical admixture was conducted in order to simplify the shrinkage mechanism as well as possible.

It is well known that excessive water in the concrete mixture is the main source of shrinkage deformations. Based on that knowledge, a relatively higher water-cement ratio (w/c) of 70% was selected to speed up that behavior. Moreover, in order to remove the concrete specimens from the molds in a relatively short time, like two

days, a high amount of cement dosage was also selected. On the other hand, it was decided to use 40% gravel with respect to the total aggregate amount, which would cause local restraints against shrinkage and strain localization. All of the input parameters that decided to use and the obtained concrete mix design proportions are presented in Table 3-2. The sample, called M1-M, is the mortar constituent of the M1 concrete, which was obtained by using the proportions given in the table. At the end, the concrete mixture became pretty workable with a slump of 24 cm (Figure 3-5).

Table 3-2 Mix Design Input Parameters

Mix	Water	Mass (kg/m ³)			w/c	Air (%)
		Cement	Sand	Gravel		
M1	245.0	350.0	977.0	651.0	0.70	1.5
M1-M	322.0	460.0	1283.0	-	0.70	2.0
M2	245.0	350.0	1581.0	-	0.70	1.5



Figure 3-5 Concrete Mix (a), Slump Test (b)

3.2.5. Mechanical Properties of Concrete

In order to characterize the mechanical properties of concrete, three standard cylindrical and two dog-bone shaped samples were cast. These samples were cured in the same way as the shrinkage samples and stored in the same environment during shrinkage tests with the experimental setup.

These test samples were tested by using a uniaxial load frame in Construction Materials Laboratory at METU such that cylindrical samples were used for determining the elastic modulus and compressive strength; dog-bones, on the other hand, were used for getting its tensile strength. The cylindrical-shaped samples whose dimensions are 10 and 20 cm in diameter and height, respectively, were preferred rather than the larger ones (15 – 30 cm) since the capacity of the loading frame is not sufficient for breaking those larger samples. There was not enough dog-bone shaped formwork; hence, tensile strength test results might not be statistically significant, i.e., unreliable. This was done just to get an idea. It was taken from literature for the numerical models.

3.2.5.1. Elastic Modulus and Compressive Strength Tests

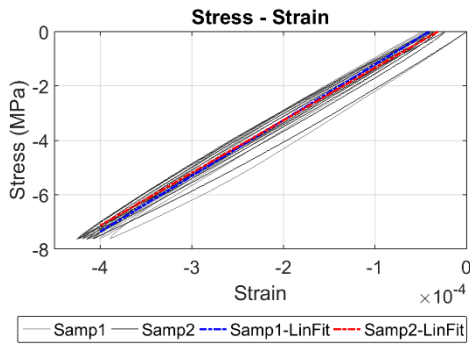
Three standard cylindrical shaped samples were tested for specifying its elastic modulus first based on ASTM C469 (ASTM International, 2010) and then tested for its compressive strength based on ASTM C39 (ASTM International, 2017c) by using the same uniaxial loading frame (Figure 3-6 (a) and (b)). Two of them were put in a compressometer that holds two LVDT instruments for axial and a single extensometer for lateral displacement measurements. Then, they were loaded in a displacement-controlled way up to a stress level (8 MPa) that might not cause any plastic deformation inside and then unloaded with the same loading rate to determine the elastic modulus. This loading scheme was repeated three times to obtain more reliable results (Figure 3-6 (c)). The concrete elastic modulus was calculated by averaging the linear curves that had been fit to each sample's stress-strain curve.



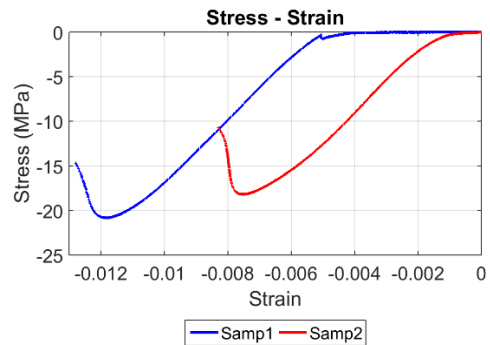
a



b



c



d

Figure 3-6 Elastic Modulus Test Setup (a), Compressive Strength Test Setup (b), Elastic Modulus Test Results of samples with M1 concrete at the 43rd day (c), Compressive Strength Test Results of samples with M1 concrete at the 43rd day (d)

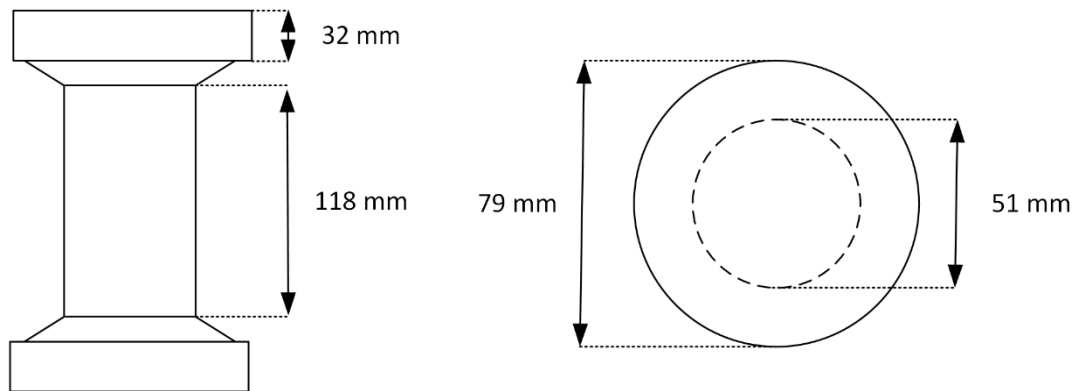
After the elastic modulus test, the compressometer instrument was removed from the setup and all of the samples were loaded one by one until they failed by using the same loading frame (Figure 3-6 (d)). The averaged compressive strength and elastic modulus are tabulated in Table 3-3.

Table 3-3 Compressive Strength and Elastic Moduli

	Age (day)	Compressive Strength (MPa)	Elastic Modulus (GPa)
M1	43	19.5 ± 1.13	19.9 ± 0.85
M1-M	43	20.5 ± 0.74	12.1 ± 1.56
M2	28	14.2 ± 0.66	-

3.2.5.2. Tensile Strength Test

Standard three-dimensional dog-bone shaped samples were prepared for the determination of concrete tensile strength (Figure 3-7). The same uniaxial loading frame was used by replacing the compression platens with tension grips. This time three 75 mm strain gauges were utilized for each sample to measure deformation. These gauges were glued on the narrower part of the samples such that the angle between each gauge was 120°, approximately when it is viewed from the top.



a



b

Figure 3-7 Dog-Bone Shaped Sample. Dimensions (a), Samples Photos Before and After the Test (b)

Each sample was pulled until they failed and the stress-strain curve was recorded (Figure 3-8). Similar to the elastic modulus test, strain computed by taking the average of the deformation records were plotted with respect to the applied stress and tensile strength was the peak of these curves. In addition to tensile strength determination, by fitting a linear curve to these plots, elastic moduli for each concrete mixture were computed again from an independent test. The obtained compressive strength and elastic moduli are tabulated in Table 3-4 for each concrete mix.

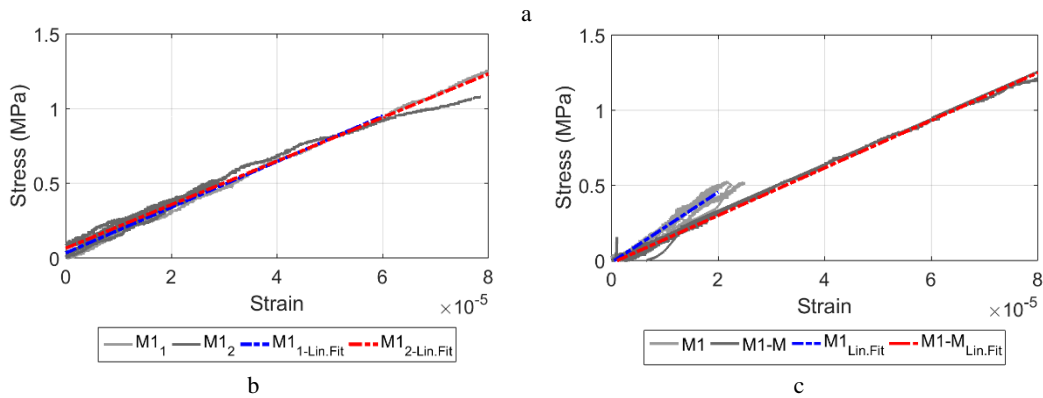
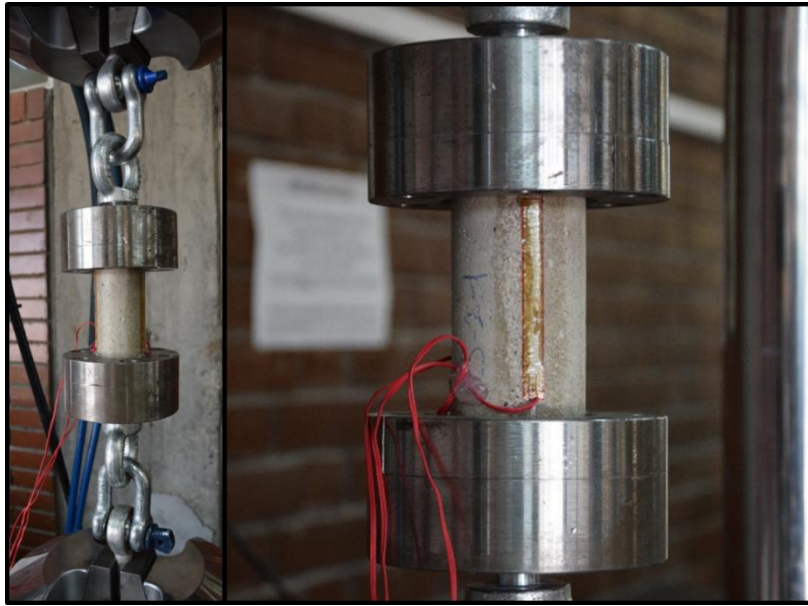


Figure 3-8 Tensile Strength Test Setup and Strain Gauge (a), M1 at 13th day (b), M1 & M1-M at 29th day (c)

Table 3-4 Tensile Strengths and Elastic Moduli

	Age (day)	Tensile Strength (MPa)	Elastic Modulus (GPa)
M1	13	1.2 ± 0.23	14.3 ± 1.77
M1	29	0.5 ± 0.0	14.3 ± 0.0
M1-M	29	1.3 ± 0.0	16.1 ± 0.0

According to the results, the tensile strength of the M1 sample on the 29th day is relatively less than the M1 on the 13th day. When the reason for this low capacity was investigated, it was observed that a single coarse aggregate was located in such a way

that it covered most of the cross-section, and the sample was cracked due to the weakness of the aggregate-cement interaction under tensile stress (Figure 3-9). A more reliable tensile strength was obtained from the test conducted on the 13th day. The tensile strength of the M1-M sample, which did not involve any gravel, is almost the same as the one of M1 at the 13th day.



Figure 3-9 Location of Single Coarse Aggregate in the sample with M1 tested at the 29th day

3.3. Validation of the Shrinkage Testing Apparatus by DIC

A novel experimental setup was prepared by utilizing the proposed DIC measurement method discussed in Chapter 2 to observe drying shrinkage induced localized strains that would occur in either plain or reinforced concrete members. This way, free and restrained shrinkage deformation and strain distributions throughout the entire surface can be monitored in detail.

3.3.1. Experimental Configuration

The setup was designed for concrete members having a dimension of 75x75x320 mm (Figure 3-10) for this study; however, it can be easily modified for any other

geometries. In addition to DIC provided surface displacement and strain distributions, two LVDTs were also set at the beam ends to measure the total length change of the samples. This way, the accuracy of the proposed DIC method for shrinkage deformations was validated.

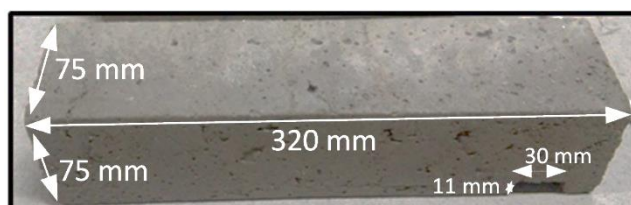


Figure 3-10 Concrete Specimen

For the validation, two shrinkage tests were conducted for a short time (10 days) in order to observe local restraining effects of gravels and reinforcing bars inside. In the first setup (S1), two plain concrete samples with different concrete mixes; the first specimen (S1-M1) was made up of M1, whereas the other one (S1-M2) was made of a different mixture (M2) obtained by replacing the gravels with the sand (Table 3-2), were tested in order to monitor the effect of gravel on shrinkage deformations (Figure 3-11 (a)). For the second test (S2), two pieces of steel bars with 8 mm diameter and 11 cm in length, on the other hand, were placed inside the specimen (S2-M1-R), which was made of M1 mixture, to create local restraining effect to shrinkage deformations (Figure 3-11 (b)). These bars were located very close to the top surface in order to better observe their effect on DIC measurements.

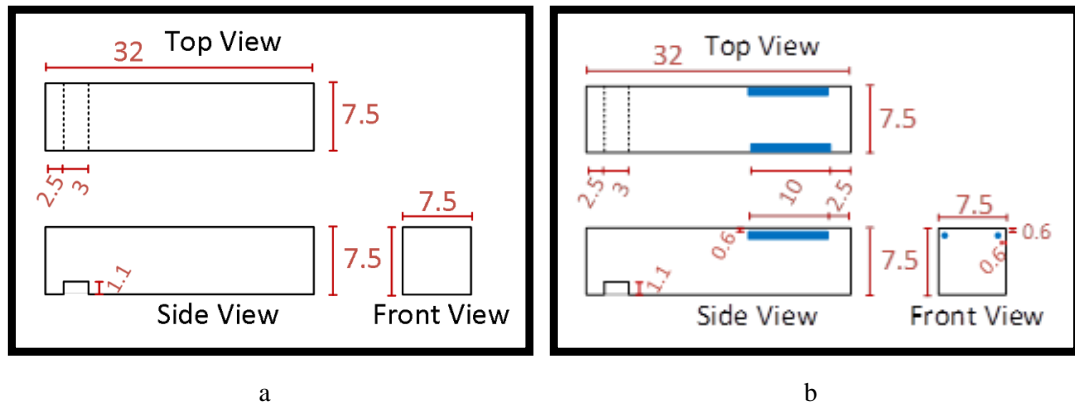


Figure 3-11 Specimen Dimensions (cm). S1-M1 & S1-M2 (a), S2-M1-R (b)

A rectangular steel frame was prepared as a testing apparatus to support the specimens and the measurement instruments (Figure 3-12 (a)). Indeed, a small gap that was compatible with the steel frame was left at one end of the beams to fix them on the steel frame such that the gap was filled by the steel profile properly (Figure 3-12 (c)). Accordingly, the beams were fixed at one end to the experimental setup. The other end was left free in the longitudinal direction. The beams were located on the steel balls to hinder the surface friction at the bottom and to allow drying of the bottom surface also. Thus, the beams were subjected to almost uniform drying through their cross-section. As presented in Figure 3-12 (a) and (b), Linear Variable Differential Transformers (LVDT) were connected to the rectangular steel frame to measure the deflections at the two points being close to the top surface.

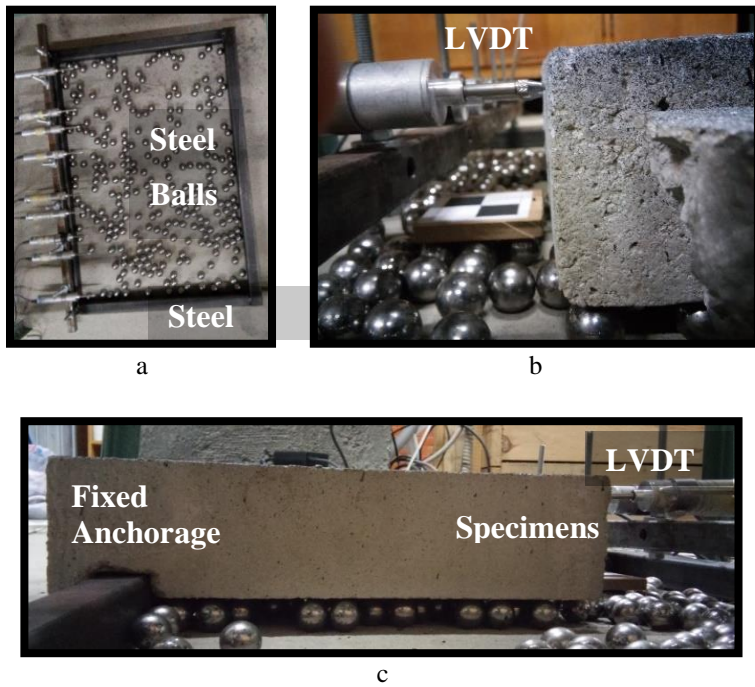


Figure 3-12 Experimental Setup

The setup was placed in a room in which ambient temperature and relative humidity were kept constant at $23 \pm 2^\circ\text{C}$ and $45 \pm 5\%$, respectively. Concrete was cast into steel molds in the same room, and they were appropriately cured for two days to delay drying shrinkage deformation and to gain sufficient strength not to break while either removing from the molds or placing to the testing apparatus (Figure 3-13 (a)). The part behind the fixed anchorage might be weak when any gravels came to this part. While removing the molds or setting it on the steel frame, it could break due to this weakness (Figure 3-13 (b)).

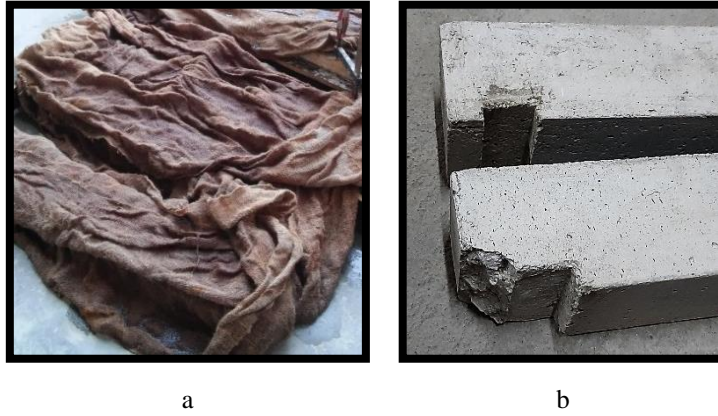


Figure 3-13 Curing (a), Broken Specimen while Locating to the Testing Apparatus (b)

For both sets, while casting concrete, two-cylinder samples (10 mm in diameter and 20 mm in height) for each mixture were also taken to obtain mechanical features of the used concrete mixtures (Figure 3-14).



Figure 3-14 Samples

Right after removing the molds (i.e., after two days), they were prepared for the DIC measurements. When the molds were removed, samples were still wet, and their colors were different from dry ones. Such a color change would affect the speckle quality since white speckles would become invisible with time; whereas, black ones would be

challenging to be recognized on a wet concrete surface (Figure 3-15). Because of this reason, the whole surface of the specimen was painted with a white color first, and then speckles were formed by applying black and white spray paints, simultaneously. The quality of the speckle pattern was tested, and the specimen was painted again if necessary. This process was generally completed in 3 or 4 hours. After that, the beams were placed in the testing setup, and the measurement system started immediately.

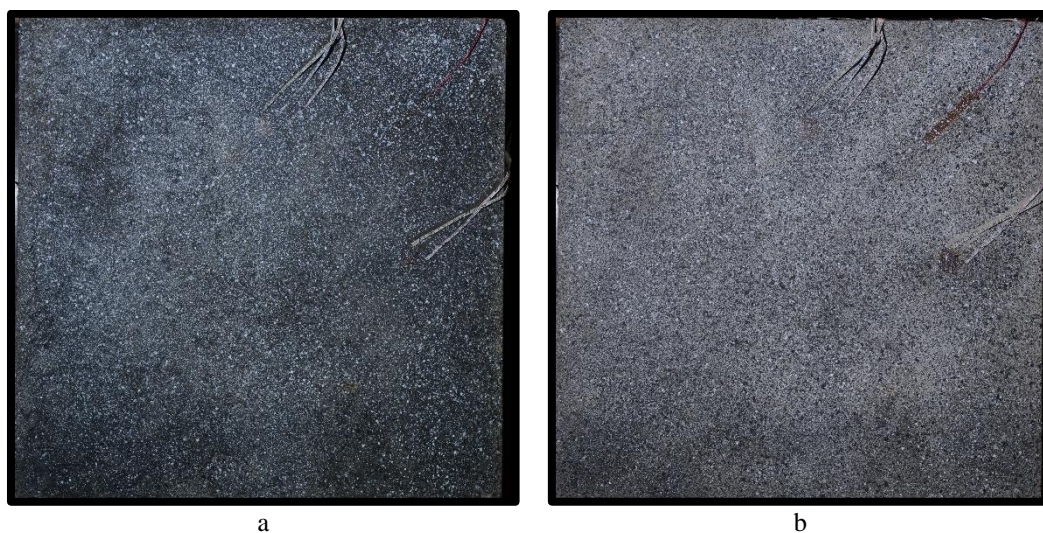


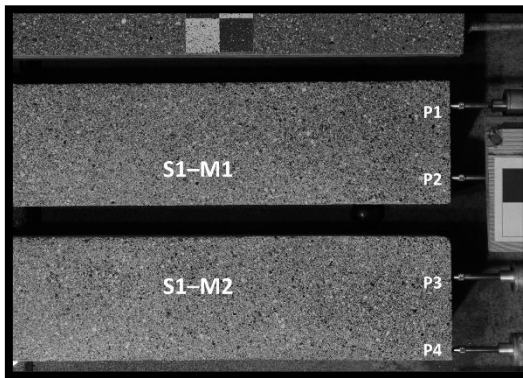
Figure 3-15 Color Change Effect on Speckles during Concrete Drying. First Day of the Test (a), 45th Day of the Test (b)

Classical measurement approaches do not provide information regarding the deformation field at the mesoscale. Therefore, the DIC method was additionally utilized to measure the two-dimensional deformation field. For this purpose, one of the DSLR cameras (CAM1) was placed at the top of the specimens to view the top surface of them clearly (Figure 3-16 (a)). Another identical DSLR camera (CAM2) was used to measure the deformations at the side surface of Specimen S2-M1-R for the second test. Camera configuration parameters are tabulated in Table 3-5. The views of both cameras are presented in Figure 3-16 (b), (c), and (d). Both cameras

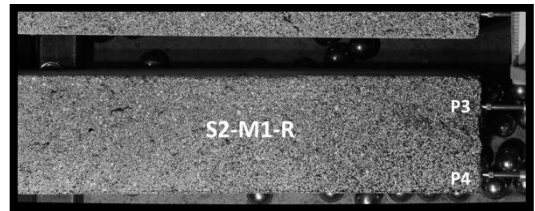
were connected to a computer that controlled the image acquisition process and stored images. The setup was illuminated with two LED projectors.



a



b



c



d

Figure 3-16 Positions and Views of Cameras and LVDT Contact Points. Camera Positions (a), Top Camera View of S1 (b) and S2 (c), Side Camera View of S2 (d)

Table 3-5 Camera Configuration Parameters

	S1	S2	
	Top Camera	Top Camera	Side Camera
Nikon:	D5200	D5200	D5200
ISO:	100	100	100
Aperture:	f/20	f/18	f/13
Shutter Speed (sec.):	1/6	1/6	1/6
Focal Length (mm):	70	70	18
Scale ($\mu\text{m}/\text{pixel}$):	62.81	60.58	62.98

For both experiments, the subset size and point distances were taken as 51 and 10 pixels for the correlation, respectively. In this study, 1 pixel in images represented approximately 60 μm for the top views and 63 μm in the side views.

3.3.2. Uncertainty Estimation

Five events, i.e., non-parallel surfaces (x_{nps}), out-of-plane deflection (x_{oop}), image sliding (x_{isld}), image averaging (x_{iav}), and image correlation (x_{icor}), were considered in the uncertainty estimation study. Any uncertainties in the measurements due to lens distortion were not taken into account. The uncertainties due to these five events were assumed to be independent and random. This way, total uncertainty is calculated by taking the square root of the sum of the squares (SRSS) of the uncertainty of each event (Taylor, 1997), as shown in Equation 3.1.

$$\delta z = \sqrt{\delta x_{nps}^2 + \delta x_{oop}^2 + \delta x_{isld}^2 + \delta x_{iav}^2 + \delta x_{icor}^2} \quad (3.1)$$

In this equation, z and x represent the total displacement and displacement due to each event and the δ prefix represents the uncertainty.

The uncertainty in non-parallel surfaces event involves the measurement plane of the specimen not being parallel to the sensor of the camera (Gajewski & Garbowski, 2014; Romeo, 2013; Michael A. Sutton et al., 2009). According to Meng et al. (2006), the

angle between the measurement surface and the camera less than 5° results in a displacement error not larger than 0.01 pixels.

Just before the experiment, both the camera's and the specimens' top surfaces were set parallel using a spirit level. Thus, the source of uncertainty for this event would be the sensitivity of the spirit level, which is $\pm 0.35^\circ$. 0.35° error can occur both at the specimen and the camera, thus by taking the SRSS the error for both planes, total uncertainty is calculated as 0.5° . In order to convert the uncertainty in the angle between these two planes, the following approach, as presented in Figure 3-17 (a), was utilized.

According to this approach, when a raster point moves from point O to point A , the actual displacement is d , whereas the measured displacement would be d' . The error in the measurement can be calculated by using Equation 3.2. Assuming that the angle θ is small and $\sin\theta$ is then equal to zero, the uncertainty can be calculated by Equation 3.3. 0.5° degree difference between the plane of the specimen surface and the sensor of the camera, the uncertainty calculated using Equation 3.3 is 0.004%. The maximum measured displacement in this study in one direction was 3.75 pixels; thus, there was 2×10^{-4} pixel uncertainty in the non-parallel surfaces event.

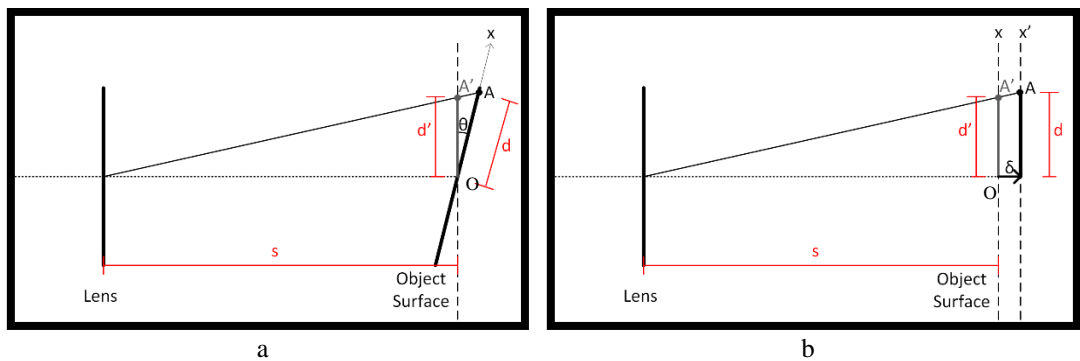


Figure 3-17 Camera Schematic for Calculation of Image Acquisition Uncertainty (a), Out of Plane Displacement Uncertainty (b)

$$\delta d = d - d' = d \left(1 - \frac{S \cos \theta}{S + d \sin \theta}\right) \quad (3.2)$$

$$\frac{\delta d}{d} = |1 - \cos \theta| \quad (3.3)$$

When the 2D DIC method is utilized, out-of-plane displacements cause errors in in-plane displacement measurements. Utilizing telecentric lenses or increasing the distance between the camera and the specimen reduce such errors (Pan et al., 2009; Sutton et al., 2008). In order to determine the uncertainty in measurements due to out-of-plane displacements, the approach presented in Figure 3-17 (b) was utilized.

As the raster point in interest moves from point O to point A , there can be an out-of-plane displacement δ . The camera sees that raster point at A' ; thus, d' is measured as displacement instead of d . In order to calculate the uncertainty, Equation 3.4 is utilized, which mainly depends on the out-of-plane displacement δ , and the distance between the camera and the specimens, s . For the presented experimental step, the maximum measured out-of-plane displacement by the side-view camera was 0.08 mm and the s distance was 104 cm. By using Equation 3.4, the uncertainty for this event (x_{oop}) was calculated as 0.008%. Considering the maximum measured displacement during experiments was 3.75 pixels, the uncertainty then became equal to 3×10^{-4} pixels.

$$\frac{\delta d}{d} = \frac{d - d'}{d} = \frac{\delta}{s} \quad (3.4)$$

Determining the uncertainty due to sliding involves two processes, tracking the raster points and computing the displacement of a surface from raster point displacements. In order to determine the uncertainty for this event, the benchmark problem, Sample 3, by SEM (2014), which involves images for rigid body translation of a surface in both X and Y directions, was utilized. 10 points were randomly selected on the surface and the uncertainty of each point was determined by computing the standard deviation

of the errors in translations for both X and Y directions. The maximum value, which is equal to 4×10^{-3} pixels, was considered to be the uncertainty for the image sliding event (x_{isld}).

Noise in the pixel intensities of the images can cause errors in the DIC measurements and averaging the pixel intensities of consecutive images is considered to be an effective way of minimizing the noise (Romeo, 2013). In order to determine the uncertainty in displacement measurement for image averaging, an image captured from one of the experiments was taken as a reference image and 30 new images were generated by adding white noise to the pixel intensities to the reference image with mean and standard deviation equal to 0 and 0.05, respectively. Then, another image was created by simply averaging these 30 generated images. By using the reference and generated image, displacements were calculated. The average of the horizontal standard deviation of displacements of 419 raster points was calculated as 6×10^{-3} pixels and considered to be the uncertainty of the image-averaging event (x_{iaV}).

The final event for uncertainty estimation is the uncertainty due to the correlation algorithm. For this purpose, sample images having a good speckle quality (Sample 1, 3, and 5 by SEM (2014)) were utilized and the resultant displacements were calculated utilizing GOM Correlate (2018). The standard deviation in the displacement errors was computed for every sample and the maximum standard deviation, i.e., 3×10^{-3} pixels, was considered as the uncertainty of the image correlation event (x_{icor}).

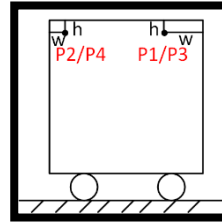
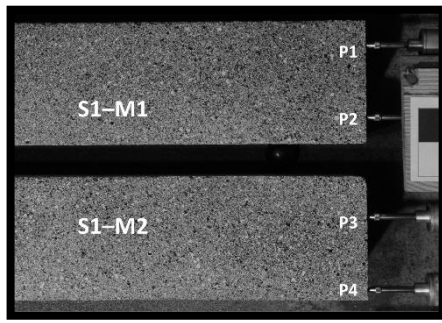
As a result, combining all the uncertainties using Equation 3.1, the total uncertainty of the measurements presented in this study was calculated as 8×10^{-3} pixels. The scale factor for the shrinkage experiments were around $63 \mu\text{m}/\text{pixels}$; thus, the total uncertainty for the presented results were about $0.5 \mu\text{m}$.

3.3.3. Comparison of Results

Both experiments were conducted for 10 days and 30 images were acquired at every 1-hour interval. These 30 images were captured sequentially with a 4-second delay

between each shot. All acquired images were modified according to the proposed correction methods in Chapter 2. After the images were corrected for lens distortion, movement of the ROI in the image due to camera vibration was also corrected (Image Sliding Correction). Initially, the maximum amount of shifting of the ROI (i.e., rigid body translation of the focused area) among the experiments was 4.61 pixels. Once the correction step was applied, the maximum shifting at the images was reduced to 0.13 pixels, which corresponded to 8×10^{-3} mm. Then, pixel intensities of the 30 images acquired at every 1-hour interval were averaged to minimize the noise in the images.

In the first experiment (S1), shrinkage displacements were measured at the top surface of the S1-M1 and S1-M2 samples. Figure 3-18 presents the location of the LVDT measurements and horizontal displacement – time graph at four points, P1, P2, P3, and P4, where LVDT and DIC measurements were compared. Even though there are the same differences in displacements readings in the first two days, the measurements match very closely after that except P3. Such differences at the beginning of the experiment may be due to having LVDT measurements 1, 3, and 6 mm below the top surface at P1, P2, and P3-P4, respectively and having displacements smaller than 0.01 mm. Although the distances between LVDT and DIC measurements in the vertical direction were the same for P3 and P4, there is a little bit difference between LVDT records at these points. The reason for such a difference may be due to the transverse distance of these points from the closest outer edge. Since the points closer to the outer edges dry faster than the core, greater shortening at the edges is expected. DIC measurements, on the other hand, were taken from the edge, it was a little bit greater than the LVDT measurement at the point P3.



	h (mm)	w (mm)
P1	1	14
P2	3	16
P3	6	23
P4	6	6

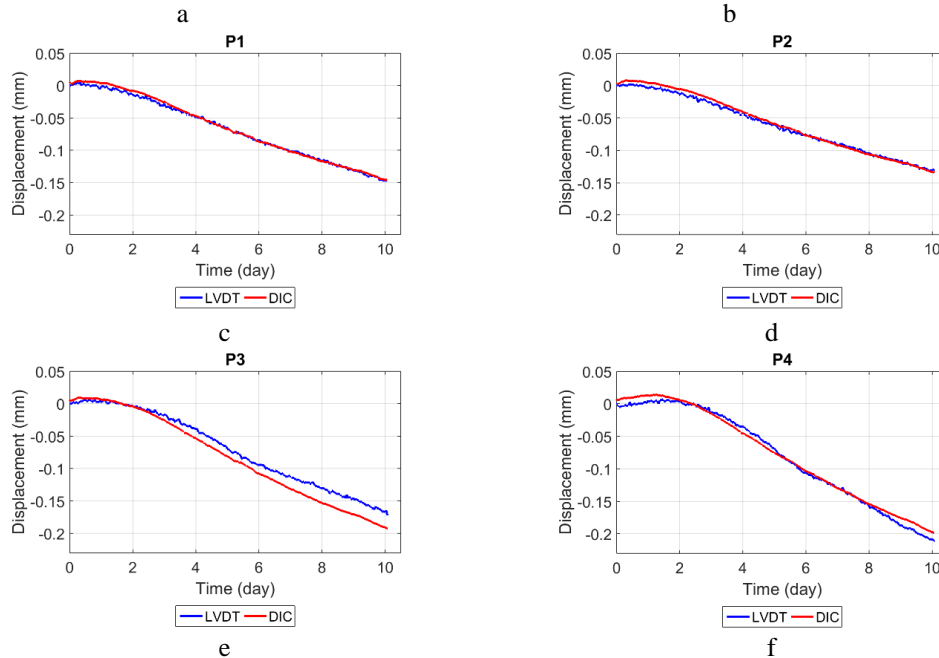


Figure 3-18 LVDT Locations (a & b) and Displacements at Free End (c, d, e, & f) (S1)

Figure 3-19 presents the longitudinal displacement and first principal strains at the top surface of the specimens after ten days. An almost uniform shortening can be observed in both samples; nevertheless, it is greater in S1-M2 than the S1-M1 sample due to lack of gravels. Since the specimens were free to move, the first principal strains should be zero. There are, however, regions with high local longitudinal strains that are colored with red. At these regions in the S1-M1 sample, as mortar shrinks due to water loss and gravels restrain this deformation, high tensile strains were measured at locations where there were gravels close to the top surface. Relatively more homogeneous strain distribution, on the other hand, can be observed on the S1-M2

sample due to not having dominant local restriction inside, but the higher strain regions were concentrated at the fixed support region.

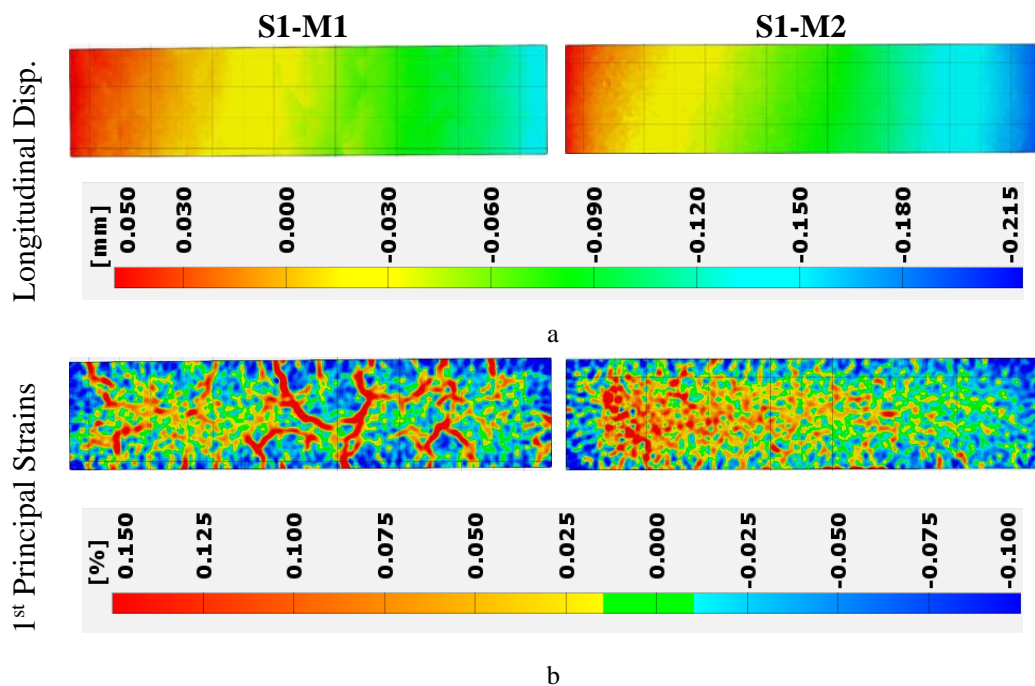


Figure 3-19 Longitudinal Displacement (a) and 1st Principal Strain Distributions (b) at the Final State

In order to determine whether the regions of local maximum strains were real or due to the noise in the images, white noise with mean and standard deviation equal to 0 and 0.05, respectively, were added to the pixel intensities of the averaged images of the S1-M1 sample. Then, these new images were correlated using the same parameters and longitudinal strains were computed one more time. Figure 3-20 presents the longitudinal strains obtained from original images and the modified images with white noise at different times.

Adding white noise to the images significantly increased the number of locations where there are local maximum strains (red regions). These regions, however, did not occur at the same place at different times. Thus, it is possible to say that spurious local maximum strains that did not occur at the same location are measurement errors due

to noise in the images. The actual local maximum strains, on the other hand, occurred at the same location as the deformation progressed even though the images have significant artificial noise at their pixel intensities. Such regions are marked with blue circles in Figure 3-20.

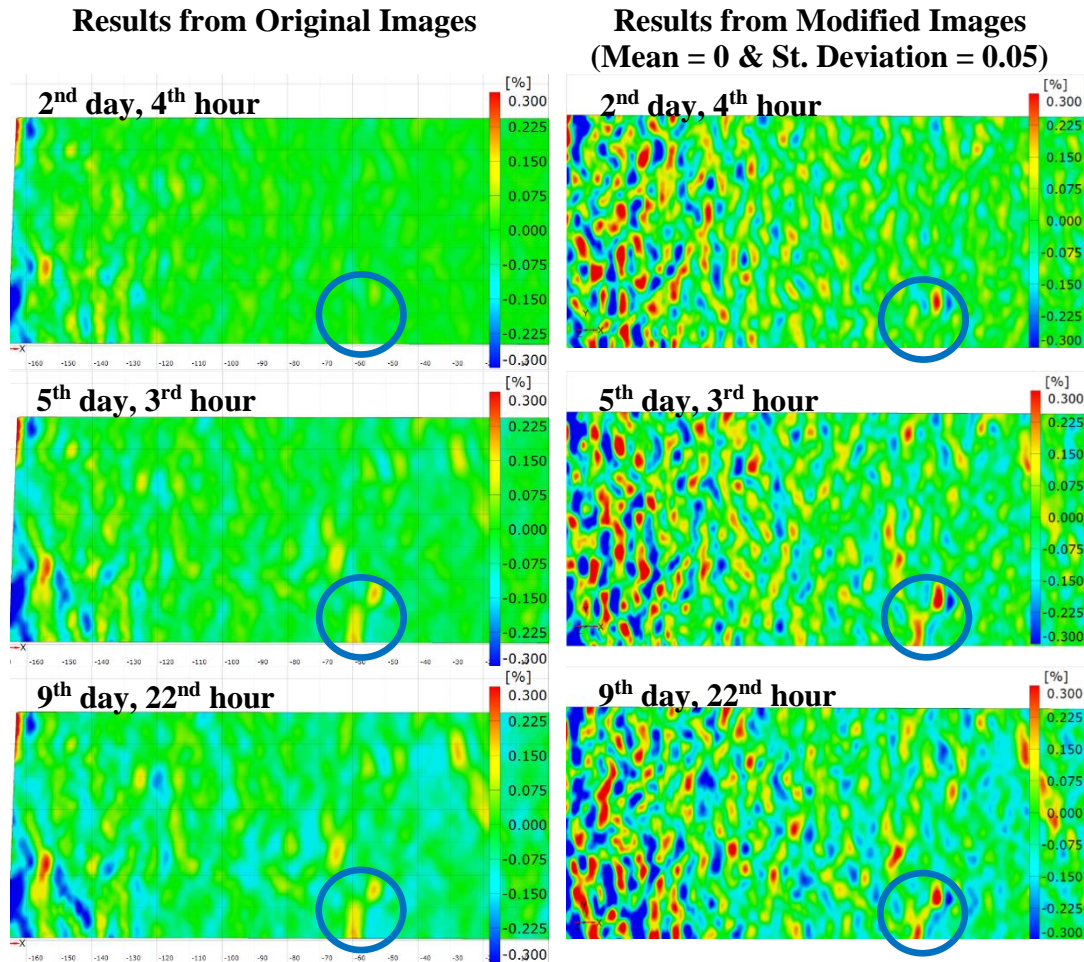


Figure 3-20 Horizontal Strain Distributions of Original and Modified Images

In order to determine whether the actual maximum strains occurred because of the gravels, the specimen was divided into four pieces, as shown in Figure 3-21. Before cutting the specimen, the second principal strains were calculated. Second principal strains are a better indicator of the locations of gravels since they restrain the

deformation, thus causes zero principal strains (Figure 3-21 (a)). In Figure 3-21 (b), (c), and (d), surface strains and photos of the slices are shown at their exact locations on the specimen. As can be seen from these figures, there is a strong correlation between the gravels that are close to the measured surface and zero principal strains.

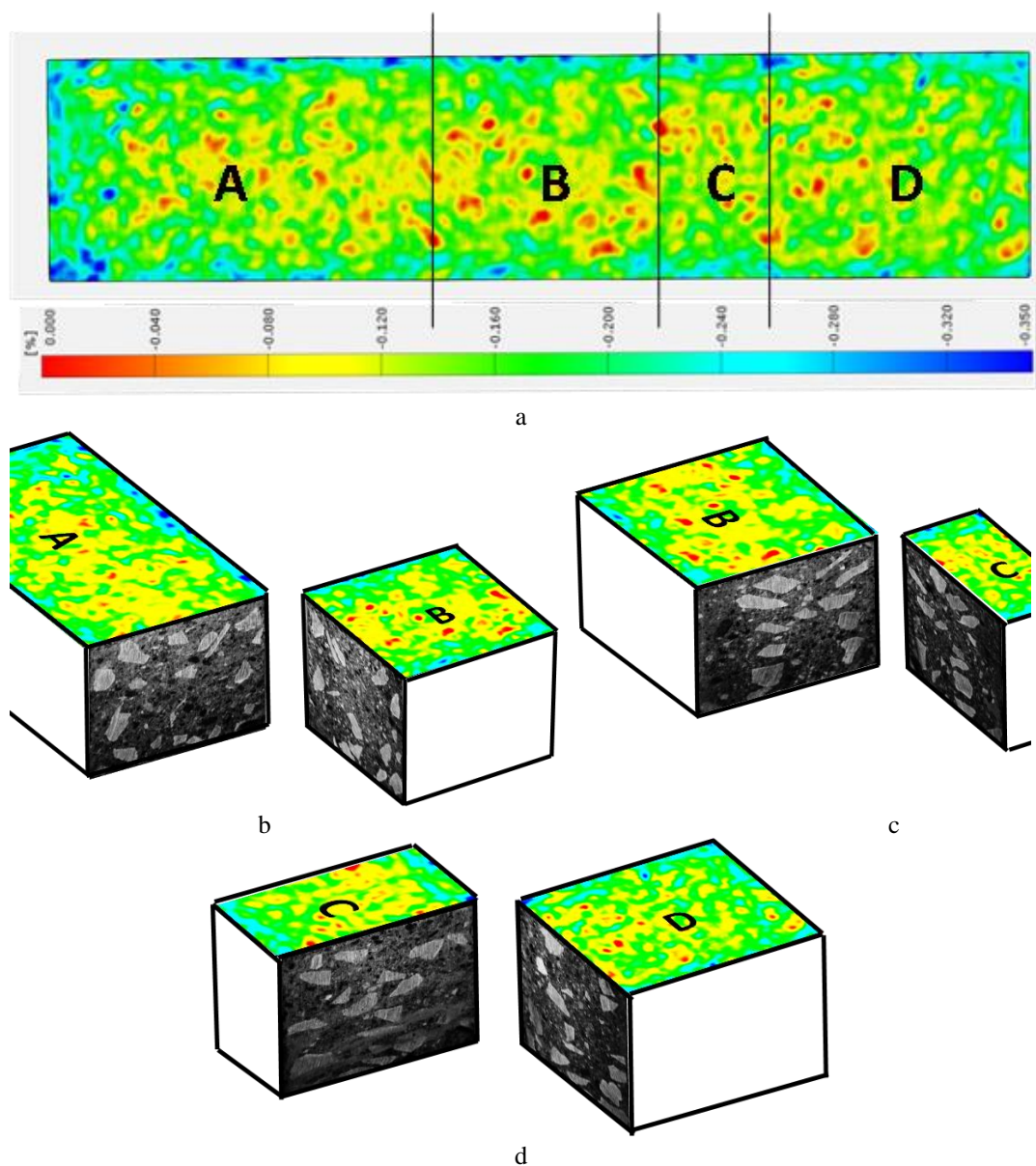


Figure 3-21 Second Principal Strain Distribution and Section Cuts of S1-M1

In the second experiment, two steel bars were placed inside the concrete beam to create additional restraints against shrinkage (S2-M1-R). In this case, DIC measurements were taken both from the top and side surfaces with two different cameras for 10 days. The main idea behind the second experiment was to question the reliability of the proposed method by comparing the results of two independent DIC measurements.

In Figure 3-22, the longitudinal displacements and first principal strains of the top and side surfaces at the end of the 10th day are put together and presented. As expected, the reinforcing bars (indicated with dashed lines) reduced the shortening due to drying. The bottom end on the beam shrank up to 0.15 mm, whereas the maximum displacement at the top was 0.1 mm (Figure 3-22 (a)). This restraining effect caused higher tensile strains distributed at a wide area at the top surface near the steel bars, shown with red color in Figure 3-22 (b). The other important aspect of these results of two independent DIC measurements, i.e., top and side surface, is that they matched successfully at their common edge. This can be better observed at the strain distributions (Figure 3-22 (b)). Regions of high and low strains, i.e., red and blue regions, continue around the common edge of both surfaces.

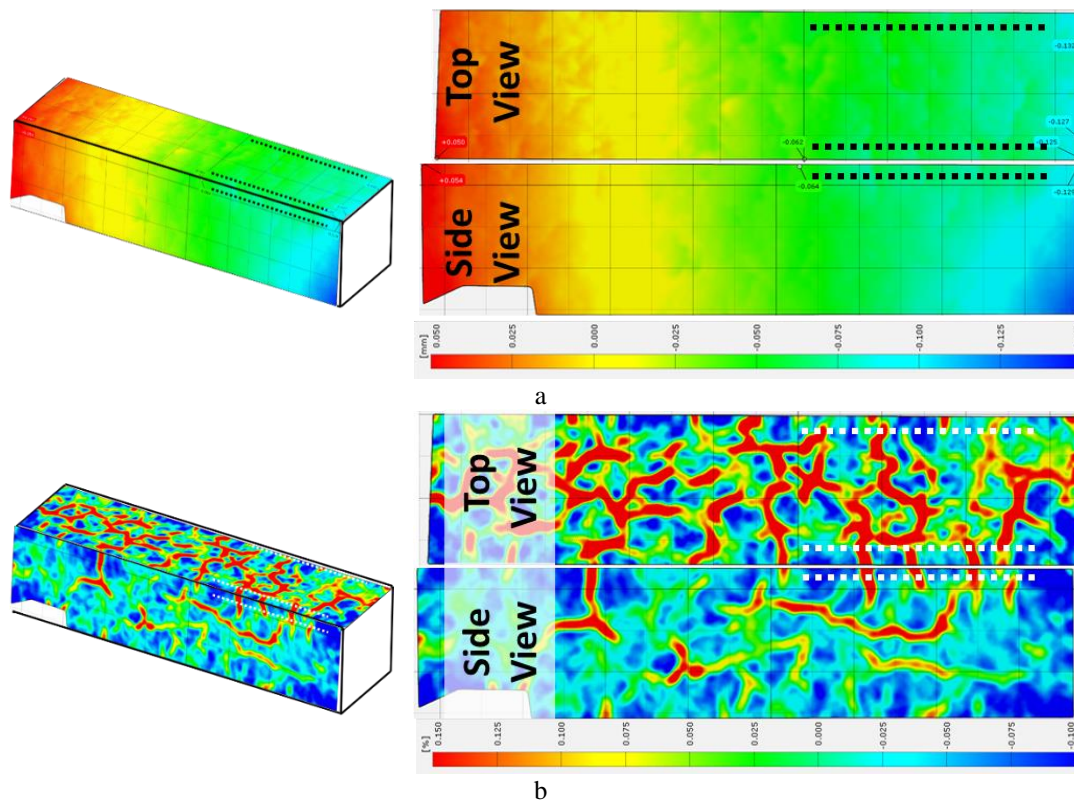


Figure 3-22 Horizontal Displacement (a) and First Principal Strain (b) Distributions of S2-M1-R

3.4. Free and Restrained Shrinkage Testing of Concrete by DIC

3.4.1. Experimental Configuration

After all the validation experiments, the actual shrinkage experiment with two samples was conducted. The aim of this experiment was to measure free and restrained shrinkage deformations on identical samples whose geometry and the material was the same as the previous ones.

The first sample, called “FSS,” was made up of plain concrete and was allowed to shrink with no restraint. It was completely the same (i.e., geometry and concrete mix) with the S1-M; accordingly, there were no restraints other than the gravels, whereas reinforcing steel bars, which restrained the shortening, were placed in “RSS” (Figure

3-23). Four longitudinal reinforcing bars having a diameter 18 mm were placed in the beam such that two of them were at the bottom and the remaining two were at the top to obtain a uniform restraining effect throughout the cross-section. These bars would be strong enough to prevent shrinkage induced length change (Figure 3-23 (a)).

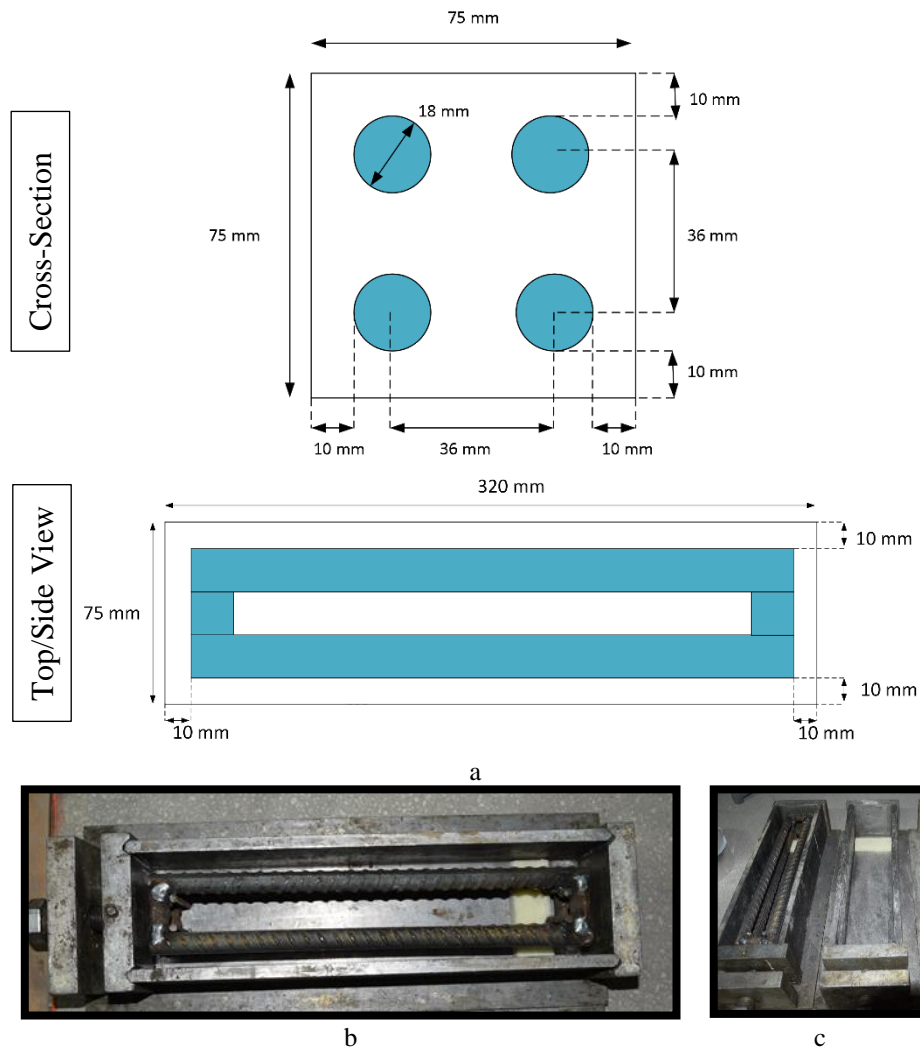


Figure 3-23 Reinforcement Details (a), Reinforcement in the Mold (b), Molds used (c)

This time, specimens were cured for three days properly by covering them with wet clothes in order to reduce the chance of breaking them while removing from molds or

placing them to the testing apparatus. After three days, the beams were placed in the testing setup, and immediately, the measurement system started. Beams stayed in the same room for 64 days, but for only the last 61 days, measurements were conducted.

Three cylindrical samples whose diameters and heights were 10 and 20 cm, respectively and one three-dimensional dog-bone shaped sample were prepared for the M1 concrete mixture and for the mortar (M1-M), which was obtained by removing the gravels of M1 just before casting (Figure 3-24). These samples were used for measuring elastic modulus and compressive/tensile strengths. Those samples were placed in the same environment and they were subjected to the same curing conditions.



Figure 3-24 Cylindrical and Dog-Bone Shaped Samples

A single DSLR camera (Nikon D5300, Appendix A) was utilized for top surface measurements of both specimens at the same time (Table 3-6, Figure 3-25). Side surface measurement, however, was not conducted. This time, a single LVDT was set due to the uniform shortening distributions observed in validation tests. Both LVDT and DIC measurements were recorded hourly and this time, only 5 images were captured at each 1-hour interval in order to reduce computational cost.

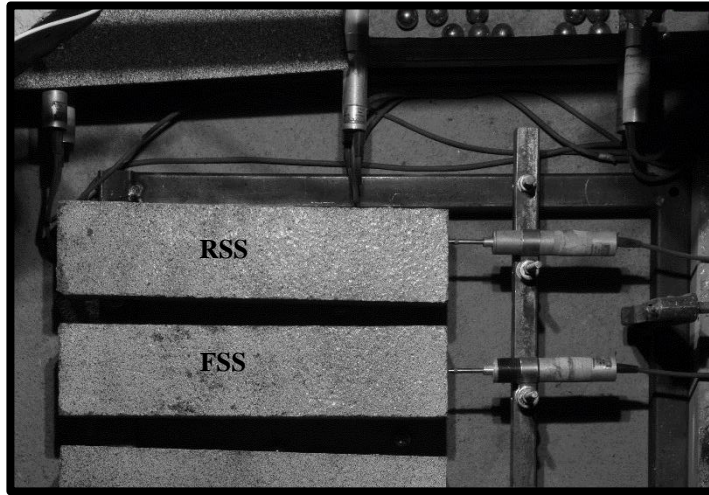


Figure 3-25 Experimental Setup

Table 3-6 Camera Configuration

	Camera 1
Camera Model:	Nikon D5300
ISO:	100
Aperture:	f/22
Shutter Speed (sec.):	1
Focal Length (mm):	45
Camera – Sample Distance (cm):	170
Scale ($\mu\text{m}/\text{pixel}$):	151.93

At the end of the test, a total of 7,295 images were captured and corrections and improvements proposed were conducted before the correlation process. First of all, each image was corrected against lens distortion, and then, they were corrected against sliding based on the fixed reference patterns. Then, a new image was generated synthetically by taking an average of the pixel intensities of 5 images captured hourly to minimize noise. After that, correlation was conducted by selecting almost 11,720 raster points (i.e., 10 pixels distance between points) for each sample with a 31-pixel facet size.

3.4.2. Comparison of Results

Shrinkage induced deformations of both concrete specimens, FSS and RSS, were recorded hourly by utilizing not only the DIC technique but also the LVDTs for 61 days, simultaneously. Free end displacement records show that the FSS sample allowed to shrink with no restraint, whereas reinforcing bars in the RSS sample prohibited the deformations pretty much (Figure 3-26). Plots obtained from each measurement technique for the FSS case are quite close to each other (Figure 3-26 (a)). Not tracking exactly the same point with the LVDT instrument is the reason for the minor differences between these two plots for the later ages. Indeed, the LVDT contact point was a little bit below from the top surface layer; hence, drying and shortening were a little bit less than the top surface. DIC, whereas, tracked the top surface; accordingly, higher shrinkage induced displacement was captured.

Figure 3-26 (b) presents only the shortening of the RSS sample measured by DIC since there was a technical problem in LVDT records, which was the change of contact point of the LVDT rod during the experiment since the specimen shifted a little bit with time. This shift also affected DIC measurements; nevertheless, it could be handled easily. Since the measurement point could still be tracked, the undesired movement was subtracted from the total displacement, which is another benefit of the DIC measurement technique. For the RSS case, although no shortening was expected due to the reinforcing bars, non-zero shortening can be observed in DIC measurements due to the unconfined regions at both ends.

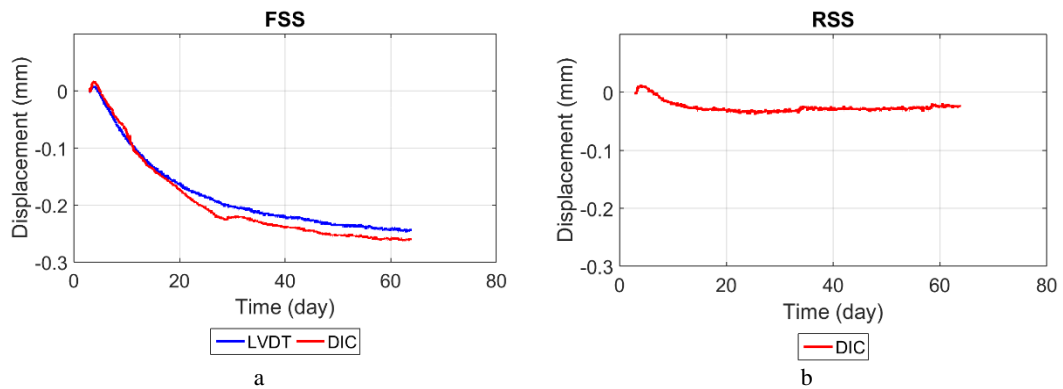


Figure 3-26 LVDT Locations and Displacements at Free End (S1)

Evolution of the first principal strain distribution on the top surfaces of FSS and RSS from the beginning of the experiment in the 3rd day until the end of the experiment (corresponding to 64th day) are compared in Figure 3-27. Gravels in the FSS sample restrained the deformation locally; accordingly, strains were concentrated around these restrained regions. Heterogeneity in strain distribution shown in the figure is the result of those strain localization. The regions indicated with blue color shortened freely due to the shrinkage whereas, gravels restrained the deformation of the nearby regions as the concrete tried to shorten. Because of this reason, high tensile strains looked like branched were observed at those regions which were indicated with red color. These are the possible regions for cracking due to shrinkage. Such localized high tensile strain branches concentrated on the regions close to the edges since edges dry faster than the interior parts. Some of these localized strain branches seen in the distribution of the FSS sample for the early ages disappeared for the later ages due to redistribution. Except for the redistribution effect, no significant change over time was observed in the FSS sample's strain distribution. Strain redistribution in the RSS sample, on the other hand, was not observed clearly due to the high restraining effect of the reinforcing bars. These significant restraints resulted in dominant tensile strain regions, i.e., regions with red color, on the RSS sample surface. In FSS results, the maximum tensile strain is around 0.1%, whereas it is almost 0.35% in the RSS results; nonetheless, no visible crack was observed. Setting a larger tensile strain bound for

the RSS results' contour plot is the other reason why strain redistribution could not be seen clearly. Similar to the FSS results, tensile strain branches started from the edges at an early age due to the drying gradient throughout the cross-section. Contrary to the FSS results, they moved towards the surface's center over time due to the effective restraining effect of reinforcing bars on shrinkage deformation.

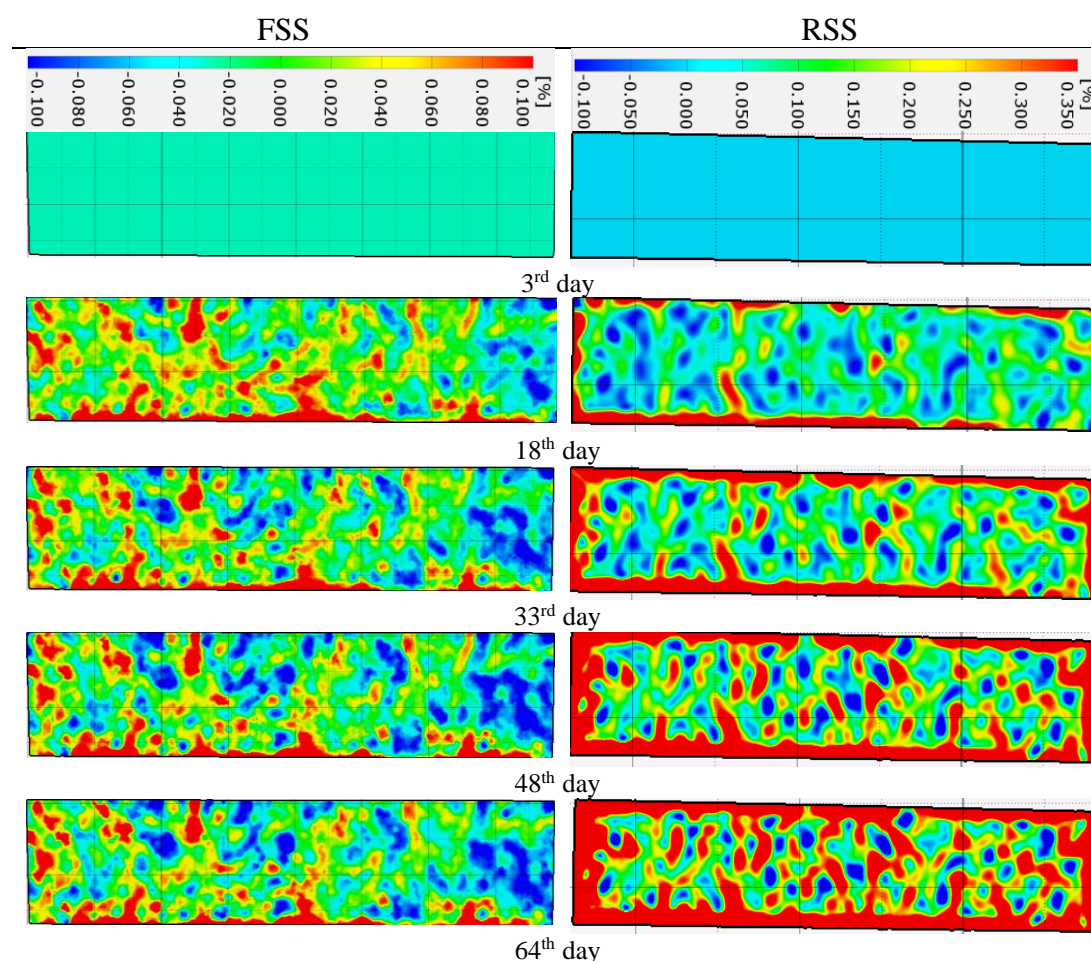


Figure 3-27 Propagation of First Principal Strains on FSS and RSS with Time.

3.5. Summary

This chapter covers details of a novel experimental setup for long-term drying shrinkage measurements of relatively larger concrete members, which can be either

free or restrained, with the proposed DIC method discussed in Chapter 2. For this purpose, two experimental sets for examining the effects of gravels and reinforcing bars on shrinkage deformations of concrete beams were conducted for ten days to obtain a figure of merit of the proposed measurement technique. Moreover, the top and side surfaces of the specimen were measured by utilizing two separate DIC systems individually and a perfect match was observed in the first principal strain distributions.

After validation of the experimental setup, the main shrinkage experiment was conducted for a much longer time (i.e., for 61 days). Two beams, one was made up of plain concrete and the other one had reinforcement, were tested to observe free and restrained shrinkage deformations simultaneously. Furthermore, the properties of concrete constituents for concrete mix design and mechanical properties of the hardened concrete that were required for the numerical modeling were identified by conducting standard tests.

CHAPTER 4

NUMERICAL MODELING

4.1. Introduction

From an engineering point of view, macro-scale modeling, assuming homogeneous material, is preferred due to its simplicity for both linear and nonlinear behaviors. Constant length change throughout an element due to shrinkage is assumed and any localization inside the element volume is not considered.

The highly heterogeneous composition of concrete makes the physics of shrinkage behavior significantly more complicated at the mesoscale since considering the local restraints such as coarse aggregates and reinforcing bars results in strain localization. When these localized strains exceed the elastic limit, nonlinear behavior like cracking occurs. For such problems, macro-scale modeling approaches are powerless as they focus on average behavior and do not account for strain localization. Spatio-temporal evolution of material and interface properties should be considered in models; accordingly, a mesoscale model that takes those effects into account could be used.

Particle-based approaches such as lattice methods and recently emerging peridynamics are strong alternatives to continuum-based finite element methods for simulating the nonlinear behavior of brittle materials. These approaches can be considered to be non-local continuum models in which particles influence the other particles within a specified distance (horizon), and damage occurs at the connection between these particles (Silling & Askari, 2005). This modeling approach is based on the integration over the horizon instead of differentiating the domain. Hence, it concerns the force equilibrium, and if any interaction is lost, i.e., cracked, the formulations are still valid. Overlapping Lattice Model (OLM) is the simplest version

of the peridynamics approach in which connection between horizons are set by pin-connected truss elements (Aydin et al., 2018, 2019; Soysal Albostan et al., 2017).

This chapter covers the theory of the OLM and a novel methodology about how to generate mesoscale OLM models of the real samples stochastically and how to simulate shrinkage induced deformations. Linear and nonlinear elastic calibrations of the methodology and implementation of the shrinkage induced mechanisms to these calibrations are discussed. Furthermore, the validation of the numerical method and comparison of the results with the experimental measurement are also presented in this chapter.

4.2. Theory of Overlapping Lattice Model

Overlapping Lattice Model (OLM) employs simple rules for the force-deformation response of bonds between nodes. The collective dynamics of damage and sophisticated bond connectivity dictates the OLM response. Each material point (node) is assumed to interact with all nodes within a certain distance. This distance is called horizon. If a uniform lattice is used, then the horizon is chosen to be proportional to the shortest distance between the nodes (d_s), i.e., $\delta = a d_s$. In two-dimensions, choosing $a=1.5$ gives the simplest lattice with 8 bonds for each node, whereas choosing $a=3.01$ yields 28 bonds with many non-local interactions. This concept can easily be extended to three-dimensions. Generally, OLM is not a mesoscale approach that accounts for the distribution of concrete constituents. It is calibrated for homogenized properties of concrete and it conveniently allows one to solve for the autonomous creation and propagation of cracks. Bonds are assumed to behave like truss elements, i.e., the direction of force is along the direction connecting the nodes (Figure 4-1). In the figure, L_a and L_b indicate the truss elements in orthogonal and diagonal directions, respectively. As most practical problems faced in concrete mechanics involve tension and shear failures, bonds are assumed to be linearly elastic in compression and assumed to soften in tension. In this way, the number of

parameters is kept at a minimum while providing a global match of the force-deformation response along with the crack propagation pattern for most practical problems.

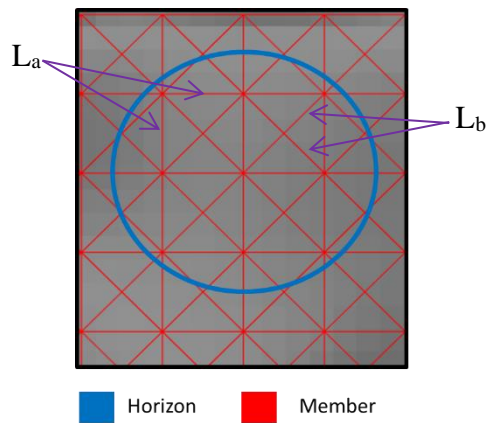


Figure 4-1 Sample Horizon for OLM ($a = 1.5$)

This method, on the other hand, requires the stiffness of the truss members to be calibrated before the numerical simulations. For this purpose, a rectangular shaped two-dimensional domain that is subjected to bi-axial tensile strain can be considered. The stored elastic energy is calculated by using the continuum equations. The stored elastic energy for the OLM is obtained as well and the equivalency of energy yields the stiffness of truss members (Figure 4-2).

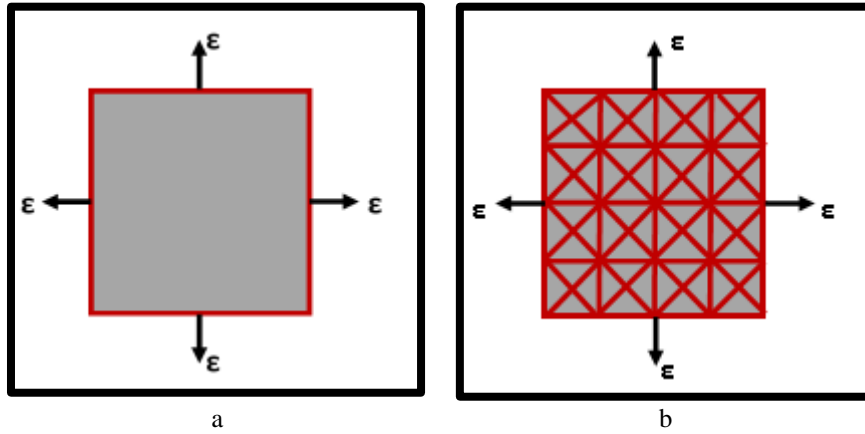


Figure 4-2 Sample Domains. Continuum Approach (a), OLM (b)

Elastic strain energy (e_c in Equation 4.1), which is the area under the stress-strain (σ - ε) curve, is the integration of the strain energy density through the entire volume (V). In a two-dimensional domain, applied strains for both horizontal and vertical axis directions are taken to be equal, so the normal stresses calculated based on Hooke's Law are also equal as well (Equation 4.2). The letters, E and ν , indicate elastic modulus and Poisson's ratio, respectively. Substituting Equation 4.2 into Equation 4.1 yields the elastic energy stored equation for the continuum approach (Equation 4.3).

$$e_c = \frac{1}{2}(\sigma_x \varepsilon_x + \sigma_y \varepsilon_y)V = \frac{1}{2}(2\sigma\varepsilon)V = \sigma\varepsilon V \quad (4.1)$$

$$\sigma = \frac{\varepsilon E}{1 - \nu} \quad (4.2)$$

$$e_c = \frac{\varepsilon^2 E}{1 - \nu} V \quad (4.3)$$

On the other side, applying the same strain in both horizontal and vertical axis directions provide that all interaction bars, even diagonal ones, are subjected to the same strain ε as well (Equation 4.4). Energy stored in a single element, e_i (Equation 4.5), is calculated similarly with the continuum approach. The letter l represents the bar length, and the parameters with subscript OLM mean that these parameters are

utilized in the OLM method. The total energy stored in the domain is calculated by summing member strain energies (Equation 4.6).

$$\varepsilon = \frac{\delta}{l} = \frac{\delta\sqrt{2}}{l\sqrt{2}} \quad (4.4)$$

$$e_i = \frac{1}{2}\sigma\varepsilon V_i = \frac{1}{2}E_{OLM}A_{OLM}\varepsilon^2 l_i \quad (4.5)$$

$$e_{OLM} = \sum_{i=1}^n \frac{1}{2}E_{OLM}A_{OLM}\varepsilon^2 l_i \quad (4.6)$$

Total elastic energies obtained from both approaches (Equation 4.3 and Equation 4.6) are equated to each other to get the stiffness of the bar elements (Equation 4.7 and Equation 4.8). Poisson's ratio should be taken as 1/3 for plane stress condition (Madenci & Oterkus, 2014). To simplify the implementation of the modified stiffness to any software, the elastic modulus of the constituent can be used directly for the bar members. In this way, only the cross-sectional area must be calibrated (Equation 4.9).

$$e_c = \frac{\varepsilon^2 E}{1-\nu} V = \sum_{i=1}^n \frac{1}{2}E_{OLM}A_{OLM}\varepsilon^2 l_i = e_{OLM} \quad (4.7)$$

$$E_{OLM}A_{OLM} = \frac{2E}{1-\nu} \frac{V}{\sum_{i=1}^n l_i} \quad (4.8)$$

$$A_{OLM} = 3 \frac{V}{\sum_{i=1}^n l_i} \quad (4.9)$$

Similarly, for three-dimensional problems, a hexahedral domain under tri-axial tensile strain can be considered. In this manner, applying the same amount of deformation in the third dimension provides 1.5 times greater continuum energy than the two-dimensional case (Equation 4.10). Furthermore, by conducting three-dimensional stress-strain behavior (Hooke's Law), the stored elastic energy equation for the continuum approach can be obtained (Equation 4.11 and Equation 4.12).

$$e_c = \frac{1}{2}(\sigma_x \varepsilon_x + \sigma_y \varepsilon_y + \sigma_z \varepsilon_z)V = \frac{1}{2}(3\sigma\varepsilon)V = \frac{3}{2}\sigma\varepsilon V \quad (4.10)$$

$$\sigma = \frac{\varepsilon E}{1 - 2\nu} \quad (4.11)$$

$$e_c = \frac{3\varepsilon^2 E}{2(1 - 2\nu)} V \quad (4.12)$$

At this point, the domain can be considered as a sphere and it can be represented by a cube-shaped connection of OLM mesh (Figure 4-3). Accordingly, the domain involves a third type of link element that is the diagonal of the cube (L_c) whose length is $\sqrt{3}d_s$. It is, nevertheless, subjected to the same strain as the other link types under tri-axial deformation (Equation 4.13). Therefore, the total energy in the OLM approach is not different from the previous two-dimensional approach (Equation 4.15).

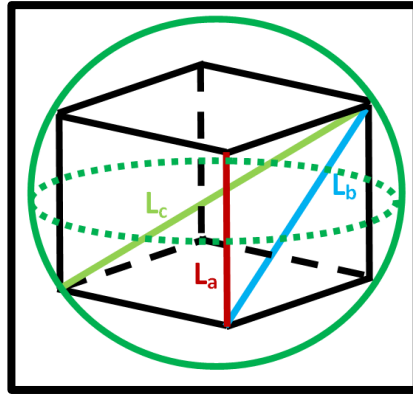


Figure 4-3 Three-Dimensional OLM Domain

$$\varepsilon = \frac{\delta}{l} = \frac{\delta\sqrt{2}}{l\sqrt{2}} = \frac{\delta\sqrt{3}}{l\sqrt{3}} \quad (4.13)$$

$$e_i = \frac{1}{2} \sigma \varepsilon V_i = \frac{1}{2} E_{OLM} A_{OLM} \varepsilon^2 l_i \quad (4.14)$$

$$e_{OLM} = \sum_{i=1}^n \frac{1}{2} E_{OLM} A_{OLM} \varepsilon^2 l_i \quad (4.15)$$

For the three-dimensional approach, ν is taken as 1/4 instead (Silling, 2000). Hence, the cross-section area of OLM members takes the form by equating the total elastic energies obtained from both approaches (Equations from 4.16 to 4.18).

$$e_c = \frac{3\varepsilon^2 E}{2(1-2\nu)} V = \sum_{i=1}^n \frac{1}{2} E_{OLM} A_{OLM} \varepsilon^2 l_i = e_{OLM} \quad (4.16)$$

$$E_{OLM} A_{OLM} = \frac{3E}{1-2\nu} \frac{V}{\sum_{i=1}^n l_i} \quad (4.17)$$

$$A_{OLM} = 6 \frac{V}{\sum_{i=1}^n l_i} \quad (4.18)$$

Any softening behavior can be implemented in the method by considering two major assumptions. The first one is that all members of a horizon should crack under the same strain. In this way, if the domain is rotated 45 degrees, for example, it would crack under the strain that is required to crack the unrotated domain. The second assumption is, having the same fracture energy for each member in the same horizon.

The size of the horizon affects the non-local behavior of the domain. Broader horizon means longer bonds between farther material points and the behavior is considered as uniform throughout these bonds. This reduces the resolution of strain localization inside the domain. Furthermore, the softening behavior of the bond elements, i.e., ultimate strain capacity, depends on their lengths to satisfy constant fracture energy throughout the horizon and the domain, since the ultimate strain and the length of the element are inversely proportional in the fracture energy equation. Choosing a smaller horizon size provides more precise non-locality behavior; but on the other hand, it increases the computational cost.

4.3. Analytical Modeling

As being a composite material, concrete members under shrinkage deformations encounter localized strains. These localized strains are due to concrete's internal mesostructure that gravels act like local restraints against shrinkage deformations. Hence, the mesoscale modeling approach is required to investigate the spatio-temporal evolution of strain localization. All major concrete constituents such as mortar, gravels, etc. are accounted for in the mathematical model in such a way that the shape, location, and stiffness of each material component and the bounding effects of those volumes to each other are taken into account. In this way, localized deformations and force redistribution are considered in the solution. Properties of each material constituents, such as gravels, are not the same and they are randomly distributed within the volume during the casting of concrete. Exact positions of each component; therefore, are not known and generating a mathematical model being completely the same with the existing concrete member is almost impossible. Various simplifications and approximations, thus, must be considered.

In this study, the concrete beam specimens that were subjected to shrinkage deformations were modeled. As a starting point, the outer boundaries of the specimen were generated first and then, the gap that was used to add a restraint for the horizontal translation of the member was generated. The gap is shown with the black solid in Figure 4-4 (a). Then, reinforcing bars were placed in the model as solid cylinders to their actual locations, as in the specimen. The ribs of the reinforcing bars were not considered. All coarse aggregates were assumed to be spherical in shape, although, in reality, they are crushed and have irregular shapes. The size of the spheres was estimated randomly based on the probability density function (pdf) of the actual aggregate granulometry obtained in the laboratory (Figure 4-4 (b)). Then, they were placed randomly in such a way that no overlapping was allowed (Figure 4-4 (c)). Randomly located aggregates in any arbitrary cross-section is presented in Figure 4-4(d).

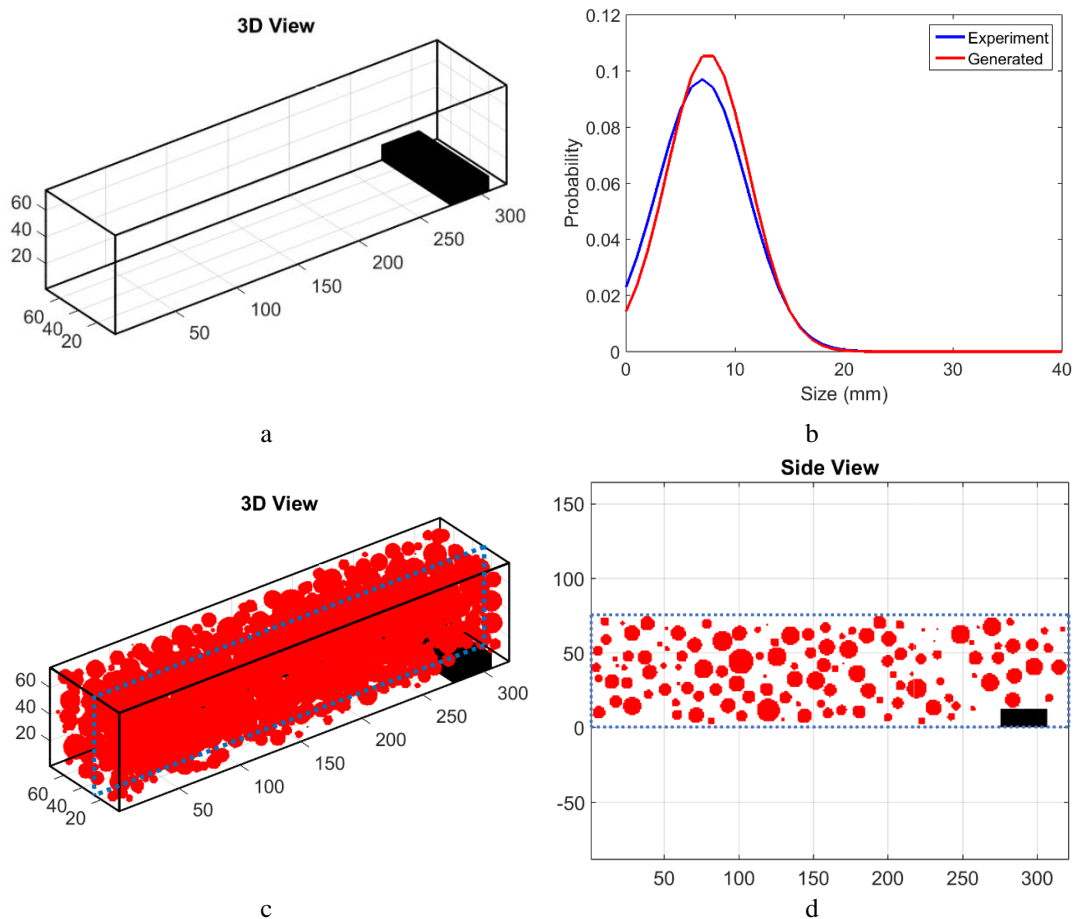


Figure 4-4 3D View of Specimen Domain (a), Probability Density Function of Aggregate Granulometry (b), 3D View of Specimen with Aggregates (c), Location of Aggregates in a Section Cut (d)

The entire domain, including the aggregates and reinforcements, was discretized such that the body was divided into 1 mm x 1 mm x 1 mm cubes, which provided 1.8 million sub-volumes. Sample slices of discretized volumes for both plain concrete and reinforced concrete are given in Figure 4-5 in which the spherical aggregates and the cylindrical reinforcements are represented by white and black color, respectively. The mortar is shown with gray color. Each sub-volume corresponded to a single constituent. Totally, three different material constituents, mortar, gravel, and reinforcement, were taken into account.

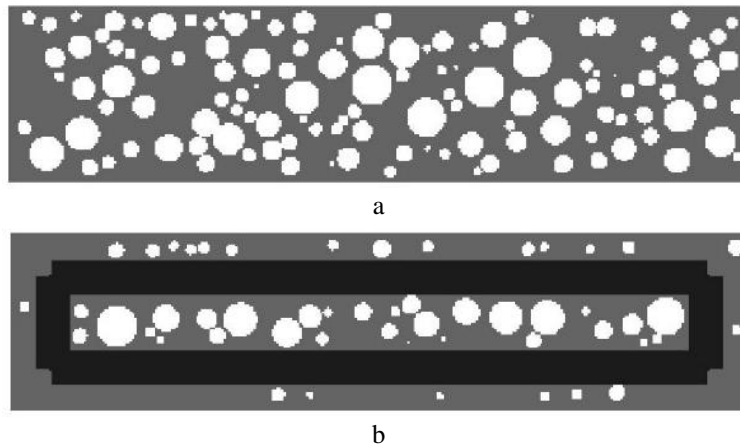


Figure 4-5 Discretized Domain Coarse Aggregates only (a), Reinforcement and Coarse Aggregates (b)

The domain was also meshed in such a way that the domain was divided into equally spaced horizons. The horizon size was taken as 3 mm. Material points were connected to each other via truss elements. Each truss element took the material properties of the sub-volumes which it intersected with. The elements were divided into pieces depending on the number of sub-volumes that they intersect and each piece took the material properties of the corresponding sub-volume. If a member exists on an interface between at least two different constituents, i.e., more than one material constituents were assigned to any truss element (Figure 4-6 (a)), the stiffness of each piece can be taken into account separately. This situation, however, is not practical for the OLM approach due to non-local behavior assumption in a horizon. As an alternative approach, the current truss element was duplicated for each constituent. These duplicated elements were connected to the same nodes, and each of these parallel elements was responsible for modeling only one of the corresponding materials (Figure 4-6 (b)). In this case, the total effective cross-sectional area was shared with those elements by equating the stiffness of the parallel elements to one of the actual serially connected members (Equation 4.19).

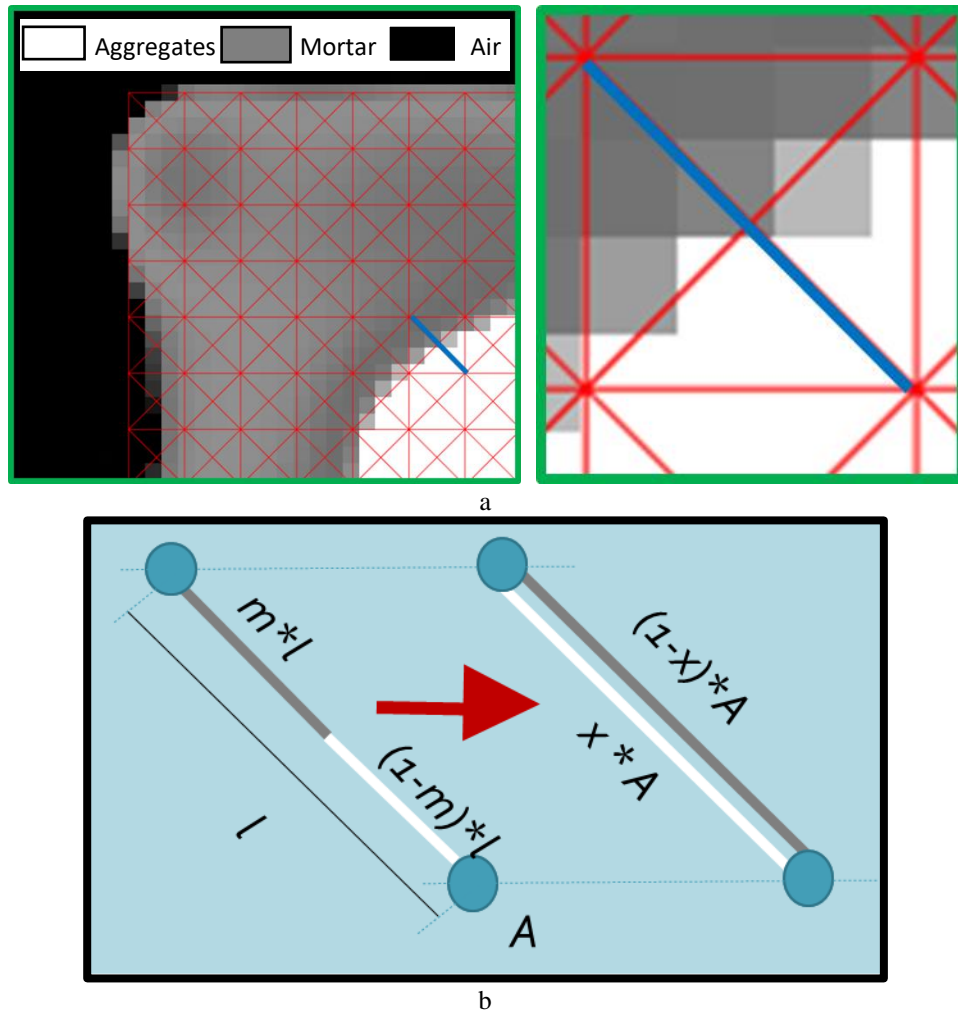


Figure 4-6 Truss Element Exist on Interface (a), Duplicated Truss Elements (b)

$$x = \frac{E_1(1 - m)}{E_1 - m(E_1 - E_2)} \quad (4.19)$$

In Equation 4.19, E_1 and E_2 are the elastic moduli of the material constituents and m is the length ratio of one of the serially connected elements. The result of Equation 4.19, i.e., x is utilized to scale the sectional areas of the parallelly connected truss elements. This equation is valid if all the elastic modules are constant. As the elastic modulus of mortar changes with time; the ratio, x , changes with time for the interfaces between aggregate-mortar and reinforcement-mortar. Thus, for such regions, the average elastic modulus value for the mortar was utilized in Equation 4.19. This

simplification caused a weaker interface zone for the early response when the averaged elastic modulus is greater than the real one, whereas stiffer behavior for the rest due to taking lower elastic modulus than it is for the later ages (Figure 4-7 (a)) if there is a perfect bond between the mortar and the aggregate or the reinforcement. In reality, air pores can exist at aggregates and reinforcements' surfaces that weaken the bonding of the mortar. This causes relatively weaker zones (Erdem et al., 2012). In order to account for the effect of air pores, in other words the weaker zones, the interfacial transition zones (ITZ) are defined. At this zone, the mortar and aggregates are assumed to be in contact if the strain at ITZ is less than the critical strain; otherwise, the elastic modulus of ITZ is reduced significantly to account for the separation of aggregate from the mortar. Maruyama and Sugie suggested an equation for the critical strain, which depends on the aggregate size and the thickness of the ITZ pore and they proposed to use the elastic modulus as 0.1% of the elastic modulus of aggregate as the strain exceeds the critical strain (2014). In this study, the critical strain was calculated by assuming the ITZ pore thickness as 2.2 μm (Maruyama & Sugie, 2014) and taking the maximum aggregate size as 22 mm. The calculated stress-strain curve for the ITZ material is shown in Figure 4-7 (b). The ITZ property was assigned to the duplicated truss elements for the aggregate material matrix at the interface regions. This way, if strain exceeded the critical strain of the ITZ material, ITZ elements were also broken; accordingly, the aggregate could not restrain the mortar anymore.

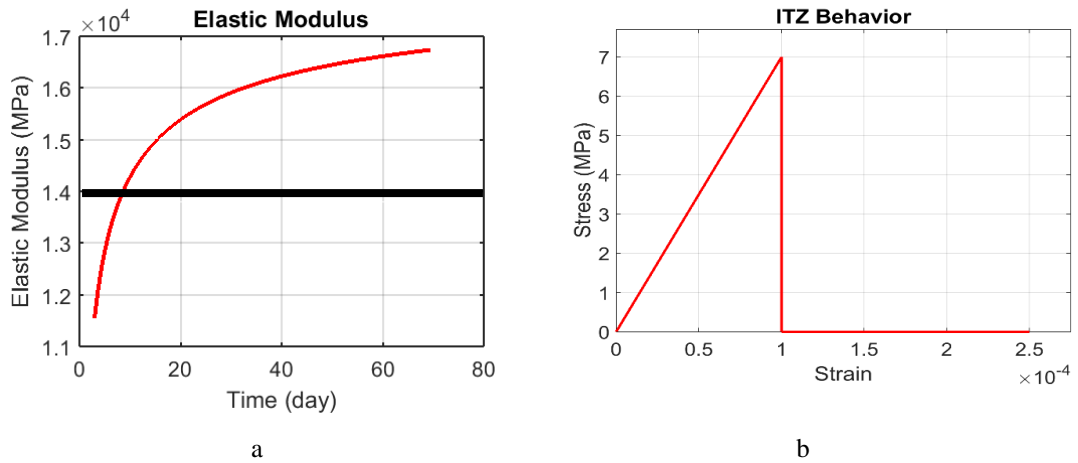


Figure 4-7 Elastic Modulus of Mortar (a), Stress-Strain curve for ITZ (b)

Shrinkage-induced deformation of gravels was ignored in the model since it is relatively small when it is compared with shrinkage deformation of mortar deformation. Since the shrinkage deformations are small, the behavior of aggregates and reinforcing bars are assumed to be linear. Elasticity modulus for limestone aggregate and steel reinforcing bars were taken as 70 GPa (Rezvani et al., 2019; Schlangen et al., 2007) and 200 GPa, respectively. Inelastic behavior was only considered in mortar. Similar to concrete behavior, the compressive strength of mortar is quite higher than its tensile strength (cracks occurs due to only tensile strain on mortar/concrete structures). For this reason, the compressive behavior of mortar was defined as linearly elastic, whereas a linear softening behavior was assigned to its tensile behavior as presented in Figure 4-8.

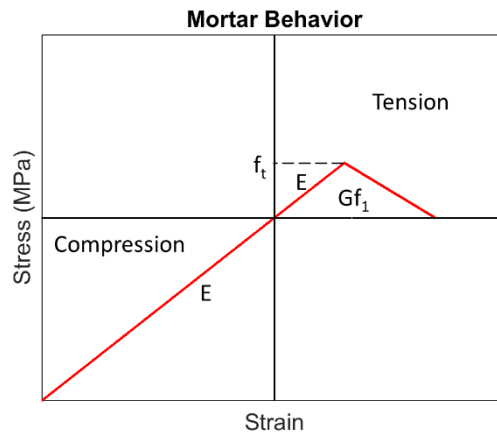
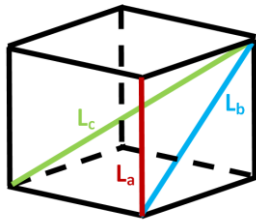


Figure 4-8 Mortar Material Model Example

In this mortar model, elastic modulus (E), tensile strength (f_t), and tensile fracture energy (Gf_t) were the only parameters that should be defined. In reality, these parameters vary with time. On the other hand, to simplify the solution, tensile strength and the tensile fracture energy were taken as 3 MPa and 70 N/m, respectively and their variations with respect to time were ignored (Maruyama et al., 2016). The same values for the tensile strength and the tensile fracture energy were assigned to each member. This way, each bar element (i.e., elements in orthogonal and diagonal directions) within the horizon would crack under the same axial strain. Only the ultimate strain parameters were modified for the diagonal members, which should be inversely proportional to member length so that the tensile fracture energy of each bar would be equal (Table 4-1). The final tensile stress-strain curves for each type of member are given in Figure 4-9. The elastic modulus of mortar was defined as the only time-dependent material parameter.

Table 4-1 Modified Material Parameters



	L_a	L_b	L_c
Length	l	$l\sqrt{2}$	$l\sqrt{3}$
Tensile Strength	f_t	f_t	f_t
Tensile Fracture Energy	Gf_1	Gf_1	Gf_1

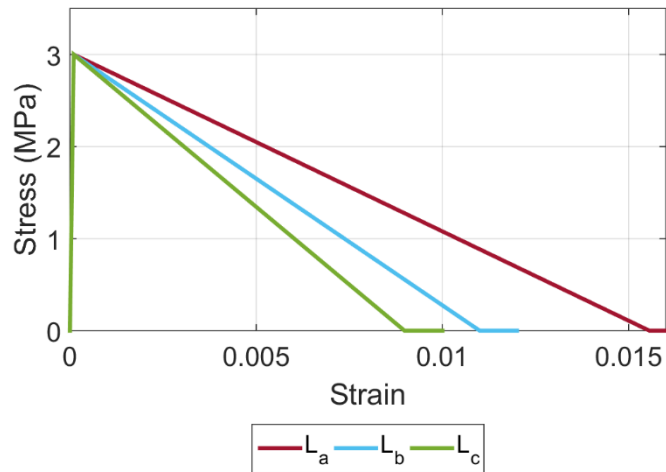


Figure 4-9 Tensile Behavior

To determine the modeling parameters of the concrete specimens, uniaxial compression was applied to the cylindrical samples composed of concrete and mortar, as discussed in Chapter 3. After 43 days, the compressive strengths and elastic modulus of the specimens were determined (Table 3-3). In order to determine the variation of elastic modulus with respect to time, CEB-FIB 90 (CEB-FIB, 1990) equations were used. CEB-FIB 90 equations use elastic modulus value at the 28th day. Since the available data was the elastic modulus value at the 43rd day, the 28th day value was adjusted in such a way that the CEB-FIB 90 equation gave the same elastic modulus value for the 43rd day. The experimental data at the 43rd day ($E_{con-test}$) and the

adjusted curve ($E_{con-est}$) are presented in Figure 4-10. Then, the elastic modulus response of the mortar with time was determined with the effective medium models.

Effective medium models provide an estimate for the lower and upper bounds of the bulk modulus of the multi-phase medium by assuming isotropic behavior for it and considering the moduli and the volume ratios of the constituents if geometric details are not available. According to Hashin-Shtrikman's model (Hashin & Shtrikman, 1963), which is one of the effective medium model, the lower (-) and upper (+) bounds for the composite material's modulus can be calculated by Equation 4.20 and 4.21, respectively. These equations can be used for getting elastic modulus limits for an isotropic medium by utilizing the conversion formula between elastic and bulk moduli (van Mier, 2012).

$$K^{(-)} = K_m + \frac{V_a}{\frac{1}{K_a - K_m} + \frac{3V_m}{3K_m + 4G_m}} \quad (4.20)$$

$$K^{(+)} = K_a + \frac{V_m}{\frac{1}{K_m - K_a} + \frac{3V_a}{3K_a + 4G_a}} \quad (4.21)$$

In these equations, K is the bulk modulus, G is the shear modulus, V is the volume ratios of constituents and subscripts, “ a ” and “ m ” represent the aggregate (gravel) and mortar matrix, respectively. Lower and upper bounds for concrete bulk moduli can be estimated by inserting these parameters (K , G , and V) for gravel and mortar into these equations.

In this study, a single modulus rather than a range was estimated since the actual moduli of the concrete and its constituent, mortar, were known from the experiment conducted at the 43rd day and the modulus of the gravel was also known from the literature. Indeed, first of all, the concrete modulus bounds were estimated and then, it was calibrated with linear interpolation (Equation 4-22) such that the interpolated

value, $K_{estimated}$, matched with the experimental data. This way, the calibration parameter, d , was obtained that provides the adjusted CEB-FIP 90 moduli curve.

$$K_{estimated} = d K^{(+)} + (1 - d) K^{(-)} \quad (4.22)$$

In a similar way, a range for any constituent material such as mortar can be estimated in an iterative way if the modulus of the composite material (concrete) and one of its constituents (gravel) are available. Time-dependent modulus of mortar was estimated for all ages ($E_{mort-calc}$) by trial and error method in such a way that the difference between the $K_{estimated}$ values and the adjusted CEB-FIP 90 moduli curve was minimized, which was compatible with its experimental data ($E_{mort-calc}$) (Figure 4-10).

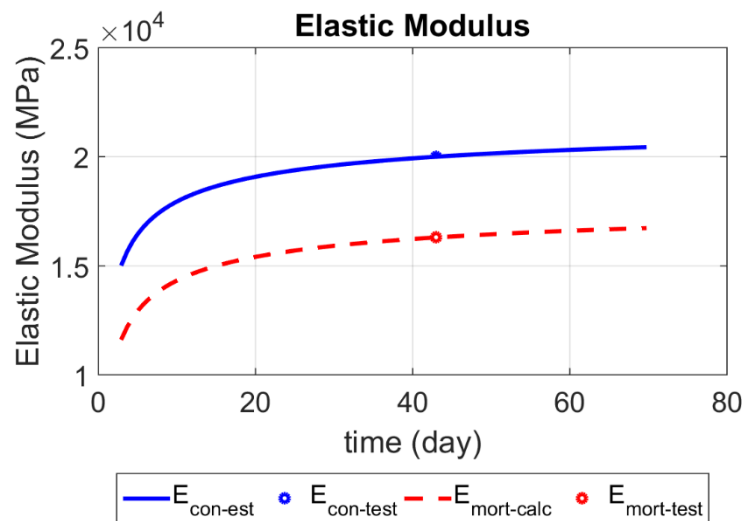


Figure 4-10 Time-Dependent Elastic Modules

4.3.1. Mortar Shrinkage Strain

The variation of shrinkage of mortar with respect to time is another parameter that must be determined for the numerical simulations. In reality, shrinkage of mortar at concrete members is not constant throughout the volume of the body. The regions closer to outer surfaces dry faster and shrink more than the interior regions (S. B. Tang

et al., 2016), but this phenomenon was ignored and it was assumed that mortar has the same shrinkage strains everywhere. Unfortunately, in the current concrete codes, there are no equations that describe the variation of mortar shrinkage strains with respect to time. Because of this reason, concrete shrinkage models were used in a modified manner to describe the shrinkage behavior of mortar even though aggregates inside the concrete have a restraining effect of shortening of mortar. It is possible to say that the time-dependent shrinkage behavior of the mortar has a similar trend with the concrete, but shrinkage strains are higher since there are no aggregates. In this study, CEB-FIP 90 concrete shrinkage model (ACI Committee 209, 2008) was utilized as a reference model that describes the variation of strains with time; nevertheless, the strain values were scaled up in such a way that the final strain values are not larger than the upper limit for mortar suggested by ASTM C596 (ASTM International, 2017b). Thus, the time-dependent shrinkage curve for mortar was obtained by multiplying the shrinkage strains for the concrete curve with 1.45 as presented in Figure 4-12. In this figure, red and black lines represent the CIB_FIB 90 shrinkage strain curve for concrete and scaled shrinkage deformation for mortar, respectively.

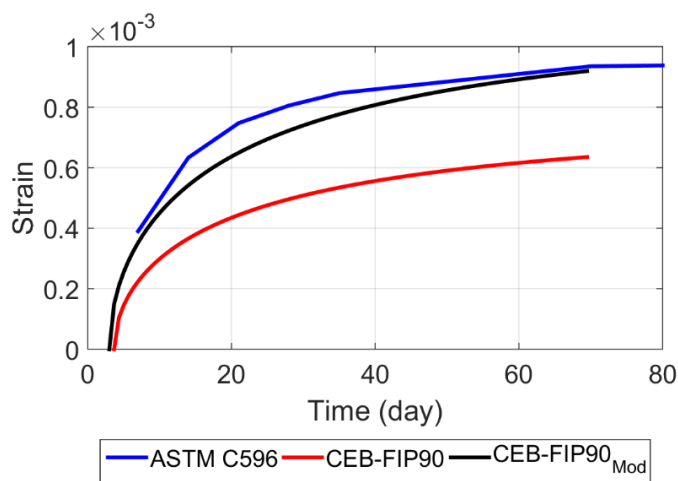


Figure 4-11 Time-Dependent Shrinkage Deformation Curves

4.4. Validation Studies

Numerical simulations were performed by utilizing a high-performance finite element analysis platform, Panthalassa (Bahçecioglu et al., 2012). Truss elements were used, and their cross-sectional areas were assigned according to Equation 4.9 for the two-dimensional models or Equation 4.18 for the three-dimensional models. The nonlinear static analysis was performed by using 0.67-day intervals to model the behavior of members between the 3rd and 64th days.

4.4.1. Two-Dimensional OLM Analysis

As a validation study to check the material parameters and the assumptions related to material behavior and mortar shrinkage strains, the shrinkage behavior of a slice of the beam specimen (FSS) was computed by a two-dimensional OLM model. For this purpose, the test specimen was scanned via a computed tomography scan that is located in the Petroleum Research Center at METU to visualize the matrix geometry and spatial distribution of constituents (Figure 4-12).



Figure 4-12 Scanning Concrete Samples via Tomography

The scanner took images of slices in the transverse direction, starting from the right end of the sample. Since the resolution of the scanner was not high enough to image the whole length of the beam, images focused only on the region, 120 x 75 mm, at the mid-span (ROI) that is shown with a red rectangle in Figure 4-12. The scanner took 24 slices at 3 mm intervals. The closest slice to the outer edge of the right end is presented in Figure 4-13 (a). In this figure, white and gray colors represent the gravels and mortar, respectively. A two-dimensional OLM model was generated that fit to the tomography image (Figure 4-13 (b)) by taking the horizon as 0.94 mm. In this model, 12,000 nodes and 48,000 elements were generated and 92 sequential nonlinear static analyses for the 61-day period were performed. The total time for the whole analysis was approximately 6 minutes.

The strain distribution at the end of the 64th day is presented alone in Figure 4-13 (c) and together with the DIC measurement results in Figures 4-13 (d) and (e). As expected, as the mortar tends to shrink, aggregates resist the shortening and tensile stresses occur at the locations around the boundaries of aggregates. The red-colored regions in Figure 4-13 (c) indicate the localized tensile strains, which may lead to minor shrinkage cracks. As can be seen from Figure 4-13 (e), the strain distributions are continuous at the neighbor edge of the numerical simulation and DIC measurement plots. Even though a two-dimensional OLM solution was performed, strain localization branches (marked with red circles) seen on the OLM strain distribution results extend to the top surface and match with the locations of the experimental localized strain results at the top surface. Thus, it is possible to say the numerical results match and complement the experimental results.

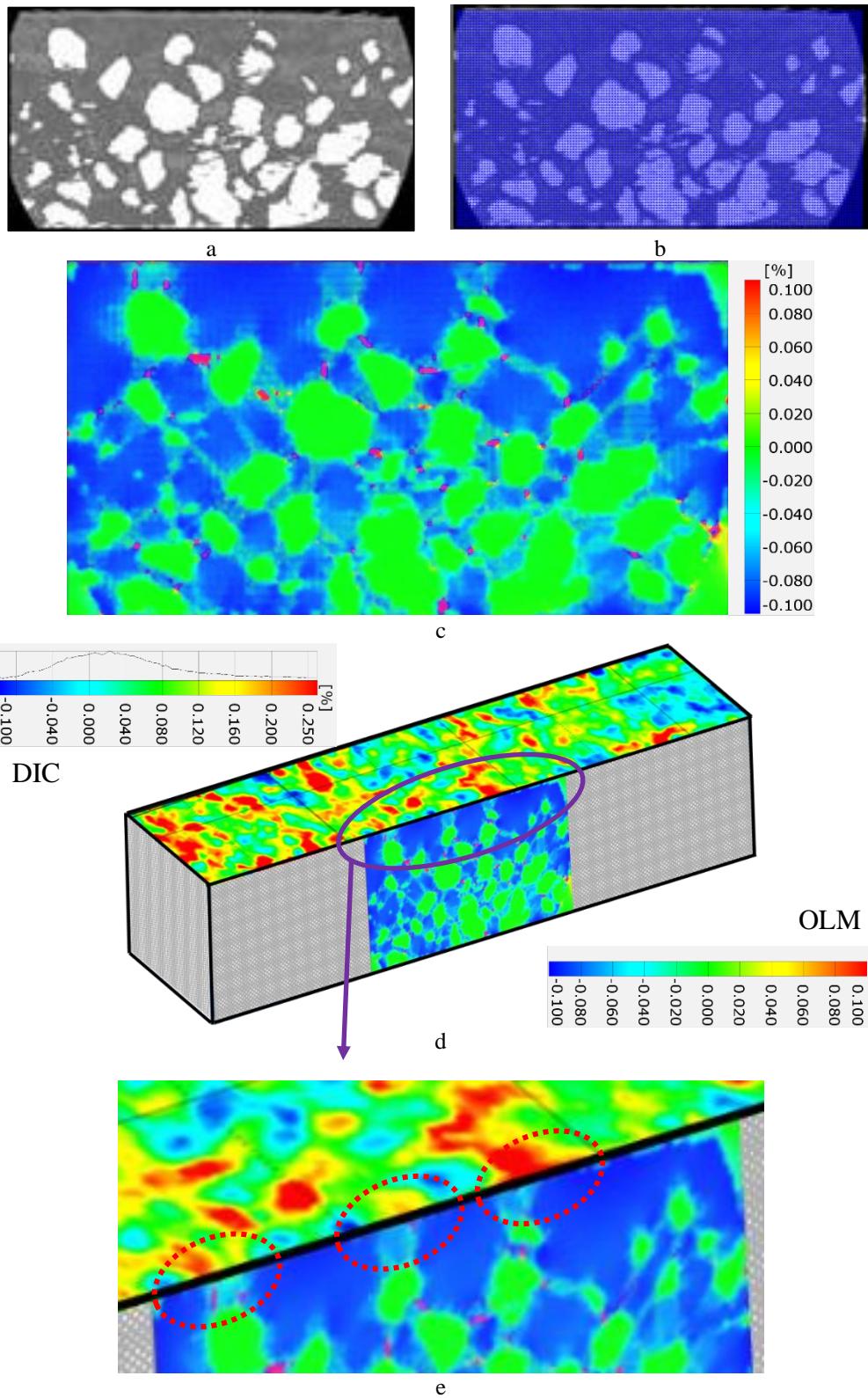


Figure 4-13 Tomography Image of Right Surface (a), Two-Dimensional OLM Model (b), OLM Strain Distribution of Right Surface (c), DIC and OLM Strain Distributions on the Specimens (d & e).

As an additional verification study, another slice, which is very close and parallel to the top surface, was analyzed and the strain distribution results were compared with the experimental ones. In order to determine the location of gravels at this slice, all tomography images that are going in the transverse direction were visited one-by-one and the pixel intensities on a line at a couple of mm below the top surface were copied to a new image. This way, by combining the transverse images at a certain height, the tomography image of a plane parallel to the top surface was obtained. Since there were a limited number of slices, it was assumed that the pixel intensities between two transverse images were interpolated. This newly generated image is presented in Figure 4-14 (a).

Similar to the previous analysis, two-dimensional OLM mesh was adapted from this generated image (Figure 4-14 (b)) and strain distributions for this surface were computed (Figure 4-14 (c)). Figure 4-14 (d) and (e) present the experimental strain distribution and the comparison of the strain distribution of the top surface obtained from DIC measurements and the OLM analysis results, respectively. There is a good correlation between the two results; the local high strain locations of the numerical results match well with the DIC measurements (shown with black dashed lines). When aggregates were close to each other and densely located at a region, much higher tensile strains were computed between the aggregates due to their restraining effect. In DIC measurements, at the location of the aggregates and their interfaces, high tensile strains were measured in a similar manner. As a result, even though two-dimensional OLM analysis was performed, the results were able to catch the shrinkage behavior of the region of interest when compared with the experimental results.

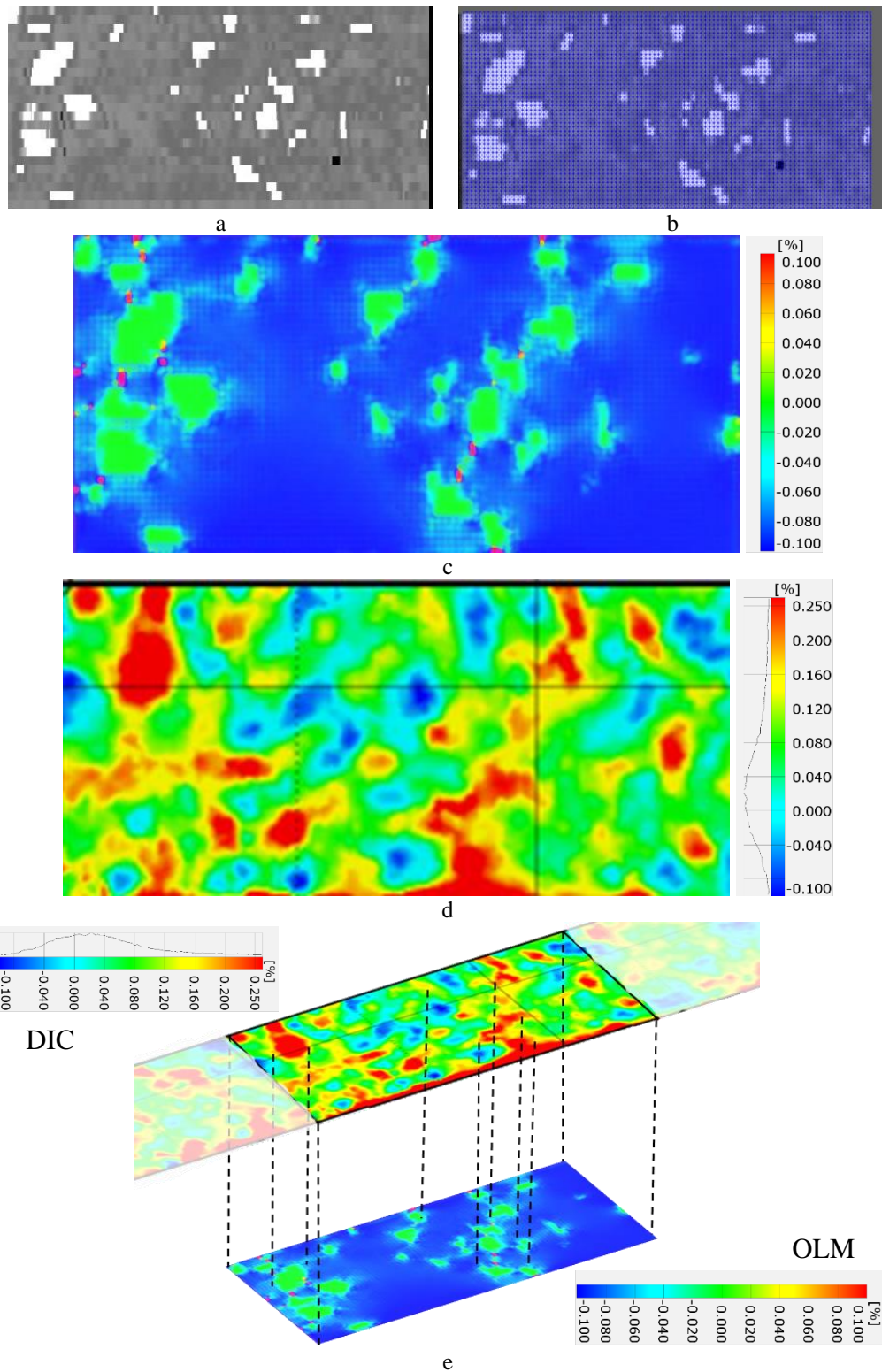


Figure 4-14 Tomography Image of Top Surface (a), Two-Dimensional OLM Model (b), OLM Strain Distribution of Top Surface (c), DIC Strain distribution at top Surface (d), DIC and OLM Strain Distributions on the Specimens (e).

4.4.2. Three-Dimensional OLM Analysis

In 2D OLM analyses, the actual material matrix of the specimen was modeled utilizing the 2D tomography images. In this case, 3D OLM analyses were performed by a synthetically generated material matrix by following the method described in the previous section. For this purpose, three-dimensional OLM models of both specimens (FSS and RSS) were generated and numerical results were compared with the experimental ones. In the numerical models, 3 mm spaced three-dimensional horizons were used, which required 73,008 material points with 1,054,131 and 1,087,655 connecting bars for FSS and RSS specimens, respectively. Displacements at the free end were compared with both LVDT and DIC measurements as well as the CEB-FIB90 shrinkage model. In addition to these, the top surface strain distributions obtained from both analyses were compared with the DIC measurements.

The free end displacements of the FSS specimen obtained from the measurements and numerical results are presented in Figure 4-15. The results of the CEB-FIB90 model are also added to the same graph. As discussed in Chapter 3, LVDT's measured the displacements a couple of mm below the top surface, that's why it measured smaller displacement than the DIC. Since the top surface dries much faster, the top surface shrinks faster than the interior surfaces, which could be one of the reasons for obtaining different values of displacement between LVDT and DIC measurements. In the numerical simulations, however, the difference in the rate of drying, in other words varying rate of shrinkage, was not considered. Because of this reason, very close results were obtained from the nodes at the end of the top (OLM_{Top}) and middle surfaces (OLM_{Mid}). The numerical results closely matched the CEB-FIB 90 model, which is somewhat expected since the mortar shrinkage model was obtained from the CEB-FIB 90 model. According to ACI Committee 209 (2008), the CEB-FIP90 model overestimates the early age response, whereas for the long time period, it underestimates the shrinkage deformations. This situation is also observed in both CEB-FIB 90 and OLM analysis results, they gave larger displacement values for the

first 10 days but about 1.25 times smaller displacements after 64 days when compared with the experimental results.

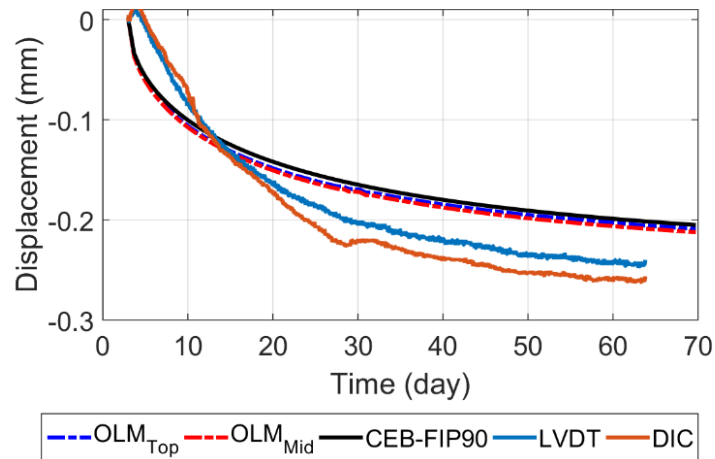


Figure 4-15 Free End Displacement of FSS

The free-end displacements of the numerical and experimental results, as well as the CEB-FIB 90 model results for the specimen with reinforcement (RSS) are presented in Figure 4-16. As expected, the reinforcement significantly reduced the effect of shrinkage and the beam specimen shortened 10 times less than the FSS specimen at the end of the experiment. The displacement of the top center (OLM_{Top}) and middle center (OLM_{Mid}) of the end section of the beam obtained from the OLM analysis are very close to each other, this shows the reinforcing bars in the numerical models provided a uniform restraining effect throughout the cross-section of the beam. The numerical simulations give approximately 1.5 times greater displacement than the experimental measurement. This is possibly due to not using the same material matrix in the numerical model with the experimental sample. Overall, the three-dimensional OLM method together with the material matrix generation and reinforcement modeling approach gives reasonable results for cases with and without the reinforcing bars. Moreover, the mortar shrinkage model has a significant effect on the accuracy of the analysis results.

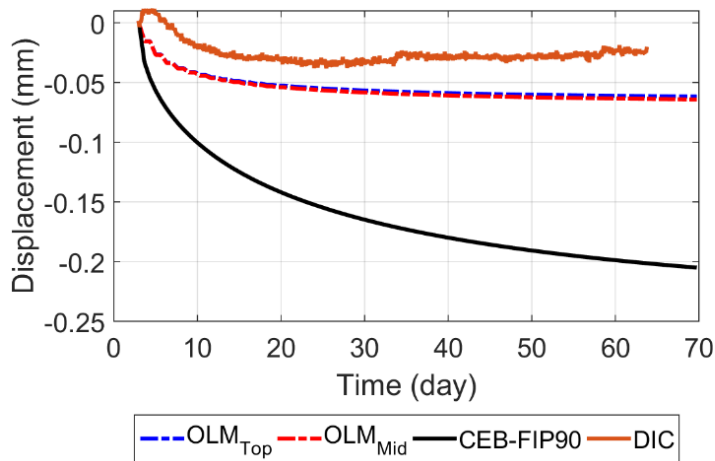


Figure 4-16 Free End Displacement of RSS

After the OLM analysis, only the longitudinal strains in the direction of each connection bar's axis can be obtained. Thus, in order to obtain the strain distribution as a continuum, the nodal displacements obtained from the OLM solution were used as if they are DIC measurement results and strain distributions were computed by first defining a displacement field using finite element interpolation functions and differentiating the displacement field (Figure 4-17). Figure 4-18 presents the strain propagation at the top surface of RSS and FSS from the beginning of the test, 3rd day to the end, 64th day. In this figure, almost uniform shortening (indicated with blue color), which increased with time, can be observed for the FSS sample. Even though this member is free to shrink, there are several strain localization regions due to gravels close to the top surface. Such regions can be observed as early as 13th day of the experiment. Tensile strains at these localized regions increase with time as well. The RSS sample, on the other hand, could not deform as much as the FSS sample due to the restraining effect of the reinforcing bars. Furthermore, more strain localizations occurred on the RSS surface which are distributed to the entire surface and increased with time. Tensile strains are greater than the FSS counterpart that are shown with red color.

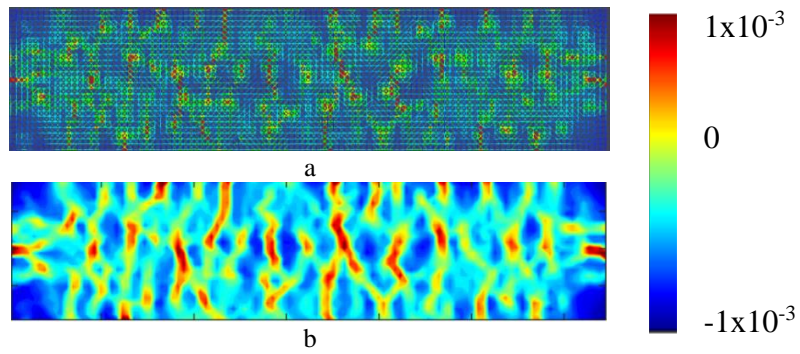


Figure 4-17 Longitudinal Element Strain (a), Computed First Principal Strain Distribution (b)

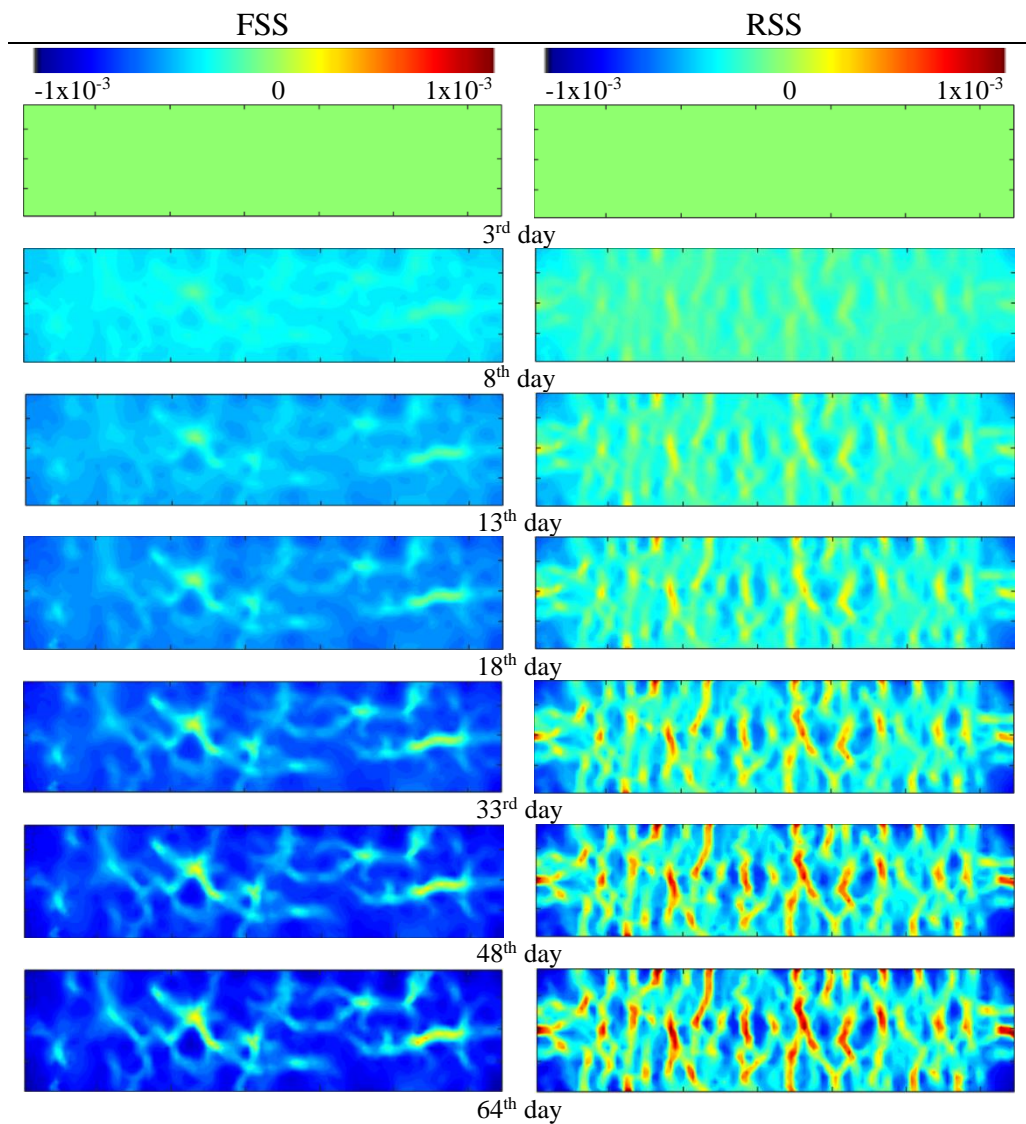


Figure 4-18 Propagation of First Principal Strains on FSS and RSS with Time.

Figure 4-19 and 4-20 present the strain distribution on the top surface at the end of the test (64th day) for the RSS and FSS specimens, respectively. In these figures, the first and second plot, (a) and (b), show the first principal strain distribution calculated by using the DIC measurement and OLM results, respectively. The reinforcing bars in the RSS specimen restrained the shrinkage deformation that caused plenty of high tensile strain regions in the shape of branches governing in the perpendicular direction of the reinforcing bars that can be seen in both numerical and experimental results. In the FSS results, however, the drying caused a more uniform strain pattern. There are a couple of places where high tensile strains occur, but these regions are due to having gravels close to the surface. The locations of such high local strains in numerical results do not perfectly match with experimental ones for both samples because different material matrices were generated in the numerical models. Even strain amounts are not in the same range for the RSS sample. Moreover, differential drying induces the propagation of strain localization from the edges; that is why these branches concentrated on the edges of both FSS and RSS specimens. This effect can only be seen in the experimental results since the numerical results are based on a uniform drying assumption.

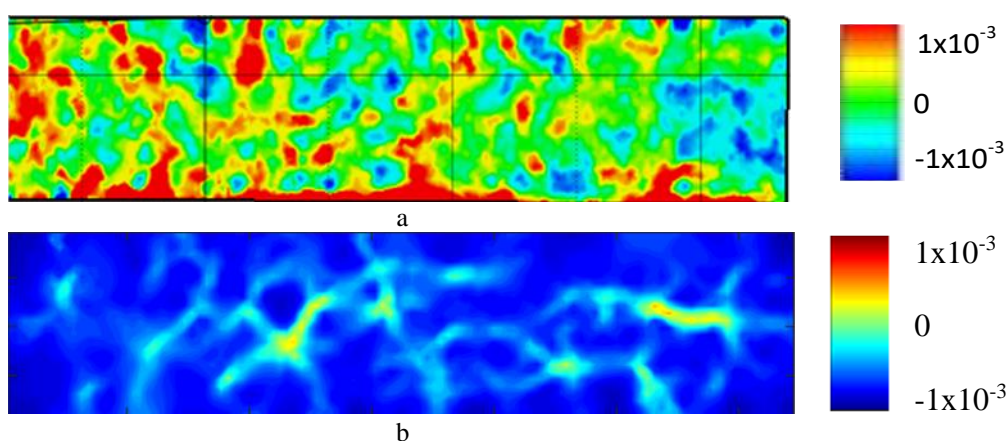


Figure 4-19 Strain Distributions of FSS. First Principal Strain Distribution (DIC) (a), First Principal Strain Distribution (OLM) (b)

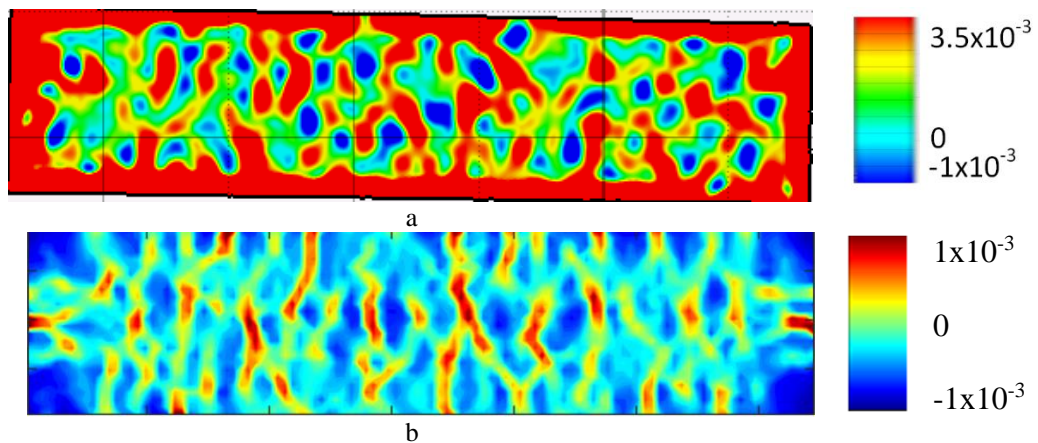


Figure 4-20 Strain Distributions of RSS. First Principal Strain Distribution (DIC) (a), First Principal Strain Distribution (OLM) (b)

4.5. Summary

A mesoscale modeling approach was presented to simulate drying shrinkage deformation in concrete and reinforced concrete members. For this purpose, mesoscale models were generated for a plain concrete beam and a reinforced concrete beam having the same geometry and material properties. OLM method, which is a kind of peridynamics approach, was adapted to solve for the spatio-temporal evolution of material properties and interfaces. Material parameters were calibrated for both elastic and inelastic shrinkage behavior. The time-dependent shrinkage deformation curve of concrete material was adapted for the mortar constituent, and it was applied to all mortar elements uniformly.

The experimental specimen's material matrix (plain concrete) was scanned via tomography, and a two-dimensional numerical model was generated to represent the actual matrix geometry. Shrinkage deformation of the experimental specimen was measured by utilizing DIC methods providing strain distribution on the top surface. Numerical results were compared with the experimental ones to validate the proposed numerical modeling approach. Additionally, one more experimental specimen with the restraining effects of coarse aggregates and reinforcing steel bars were left to shrink in a controlled laboratory environment. Experimental and numerical results of

both plain concrete and reinforced concrete samples were compared in order to validate the proposed methodology for modeling any three-dimensional domains. It is possible to say the numerical results match and complement the experimental results.

CHAPTER 5

CONCLUSION AND FUTURE WORKS

5.1. Executive Summary

A novel measurement approach based on the DIC method is proposed for experiments that require surface deformation measurement with high sensitivity for a long duration of time. In this approach high-resolution DSLR cameras in photograph mode were utilized instead of conventional high-speed video cameras to be able to measure relatively small deformations in the order of μm on large surfaces. Using DSLR cameras in photograph mode, however, brings its own issues that may significantly affect the measurement accuracy. These issues were identified as alterations in images due to lens distortions, shifting of the region of interest in the images due to vibration caused by the shutter mechanism vibration, and noise on the image sensor. Several improvement methods were developed that minimizes the effects of these issues and validated by comparing the results of the other measurement devices in three different types of experiments. Each experiment has different challenges, such as tracking the relatively small deformations of a brittle material, identifying the non-visible crack patterns, and obtaining the same deformations from two independent DIC measurements for the same surface. The results showed that utilizing high-resolution DSLR cameras together with the proposed improvement methods in the DIC method allowed measuring and quantifying deformations on concrete surfaces.

A new experimental setup was then designed for conducting and measuring long-term shrinkage deformations of plain and reinforced concrete beams. Initially, two sets of experiments were conducted for ten days to examine the effects of gravels and reinforcing bars on shrinkage deformations as well as to obtain a figure of merit of the proposed measurement approach. Furthermore, the top and side surfaces of the

specimen were measured independently to validate the results of the DIC measurement. After the experiments, a good match was obtained in the first principal strain distributions at the neighborhood edge of the top and side surfaces which gave enough confidence about the experimental setup to start the actual shrinkage experiments.

The actual experiments were conducted for a much longer time (i.e., for 61 days). Two beams, one was made up of plain concrete and the other one had reinforcing bars in it, were tested to observe free and internally restrained shrinkage deformations. The experiments were successfully completed and the surface displacement and strain distribution variations for 61 days were obtained for both specimens. The results were in good agreement with the LVDT measurements and the restraining effects of reinforcing bars were clearly observed at the surface strains.

A new modeling and calibration methods were developed that was based on overlapping lattice method (OLM) for simulating the shrinkage behavior of plain and reinforced concrete beams at the mesoscale level. The mechanical properties of the hardened concrete were identified with the standard test procedures and used for calibrating material parameters utilized during the OLM simulations. Moreover, the time-dependent shrinkage deformation curve of the concrete material was used as a basis to describe the shrinkage behavior of the mortar. A constant drying gradient was assumed throughout the whole volume. For validating the material parameters, calibrations, and modeling assumptions, a two-dimensional OLM model was generated in the light of the actual material matrix obtained by scanning the side section of the plain concrete beam element via tomography. Numerical results of two different surfaces were compared with the experimental results to figure out the merit of the proposed numerical modeling approach and it was observed that assumptions done for the material properties and calibrations of the element stiffnesses were sufficient to simulate the behavior reliably.

Then, three-dimensional OLM models of the FSS and RSS samples were created. Their material matrices, however, were generated stochastically based on the granulometry of the gravels, mix design proportions of the concrete, and the reinforcing bars inside the RSS sample since they were not known exactly. Numerical total length changes and strain distribution at the top surface were compared with the experimental measurements.

5.2. Concluding Remarks

The main conclusions of this study are as follows:

- Deformations in the range of μm at a large region can be measured by capturing images in photography mode with high-resolution DSLR camera. In the presented experimental studies, the shrinkage deformations at the beam specimens' surfaces having 32 cm x 7.5 cm dimensions are successfully measured.
- With the proposed image-sliding correction procedure, the undesired rigid body translation and/or rigid body rotations occurred on images due to vibration of the shutter mechanism of DSLR cameras can be minimized. This approach significantly increased the accuracy of the DIC measurements.
- Capturing more than one image in a relatively short amount of time consecutively and averaging of the color intensities of these back-to-back acquired images reduced the noise on images significantly. This correction facilitated the tracking of the raster points from one image to another.
- The proposed measurement approach with the DIC method enabled to observe local restraining effects of aggregates and reinforcing bars during the shrinkage process for 61 days.
- The numerical results obtained from the DIC measurements were in good agreement with other independent measurements. Moreover, two independent DIC measurements also matched to each other. Thus, the proposed

measurement approach not only accurately describes the deformation characteristics but also gives reliable numerical results.

- Overlapping lattice model (OLM) based numerical simulations can successfully describe the shrinkage deformation of both plain and reinforced concrete beams. The validation studies that were performed by comparing 2D OLM results and DIC measurements showed that the proposed modeling and calibration approach produced not only reliable results but also caught the local deformation characteristics of specimens.
- The same drying rate was assumed for the whole volume of specimens during numerical simulations. Because of this reason, the free end displacements of the center and the top of the cross-sectional were computed as almost the same. This behavior was not observed in the experimental results. Thus, differential drying of exterior and interior points should be considered for more refined shrinkage simulations.
- Free end displacements obtained from the numerical solutions of the plain concrete specimen are very close to the macro-scale shrinkage model of CEB-FIP90. This is mainly due to the time deformation characteristics of the mortar that was derived from CEB-FIB90. The numerical results, however, did not fully match the experimental results which indicates that CEB-FIB90 cannot fully describe the shrinkage deformation of beam specimens.
- Reinforcing bars provided a significant restraining effect on shrinkage deformations, thus reduced the total shortening of the beam specimen. Such a reduction was also computed with numerical simulations. The deformation characteristics are similar when compared with the experimental results, but there is a little difference between the final shortening values. This was mainly due to using a generated material matrix instead of the actual one.
- Several local strain branches are observed at the principal strain distributions for the plain concrete specimen in both experimental and numerical results. These branches were concentrated in regions closer to the outer edges in the

experiments since drying is much faster in those regions. In the numerical results, however, these branches were mainly located at the boundaries of coarse aggregates since variation in the drying rate throughout the cross-section was not considered.

- In the reinforced concrete specimen, strain localization occurred at more locations due to the existence of the dominant restraining effect of reinforcing bars. In this case, the trend of the localized strain branches observed in experimental and numerical results is quite similar to each other since the reinforcing bars were placed exactly the same location in the numerical model as in the actual specimen.

5.3. Recommendations for Future Study

This study has some limitations in order to simplify the procedure. However, this study can be extended by following the future studies recommended:

- By utilizing this measurement methodology, the experimental setup can be adapted to two-dimensional structural members. This way, the multi-dimensional effect of the shrinkage mechanism that occurs in any arbitrary geometry can be investigated.
- By adapting the proposed measurement method to the three-dimensional DIC method, shrinkage response in the third direction will also be considered.
- Conducting more tests for more samples with various concrete mix designs will provide a better understating of the shrinkage phenomenon.
- Obtaining time-dependent mechanical properties of the hardened concrete by conducting more tests for several ages of the material and applying time-dependent shrinkage response to the numerical elements by considering the drying gradient will converge the numerical results to the experimental ones more.

- Considering the shrinkage response of the gravels and the existence of air entrained in the material matrix for the numerical models will provide more reliable results.

REFERENCES

- ACI Committee 209. (2008). ACI 209.2R-08 Guide for Modeling and Calculating Shrinkage and Creep in Hardened Concrete. In *American Concrete Institute Technical Documents*.
- Albostan, U., & Kurç, Ö. (2016). Application of 2D Digital Image Correlation: Three Points Flexure Test of Reinforced Concrete Beam. *12th International Congress on Advances in Civil Engineering*.
- Almusallam, A. A. (2001). Effect of environmental conditions on the properties of fresh and hardened concrete. *Cement and Concrete Composites*, 23(4–5), 353–361. [https://doi.org/10.1016/S0958-9465\(01\)00007-5](https://doi.org/10.1016/S0958-9465(01)00007-5)
- ASTM International. (2017a). *C157/C157M-17 Standard Test Method for Length Change of Hardened Hydraulic-Cement Mortar and Concrete*.
- ASTM International. (2017b). *C596-09(2017) Standard Test Method for Drying Shrinkage of Mortar Containing Hydraulic Cement*. <https://doi.org/10.1520/C0596-09R17>
- Aydin, B. B., Tuncay, K., & Binici, B. (2018). Overlapping Lattice Modeling for concrete fracture simulations using sequentially linear analysis. *Structural Concrete*. <https://doi.org/10.1002/suco.201600196>
- Aydin, B. B., Tuncay, K., & Binici, B. (2019). Simulation of Reinforced Concrete Member Response Using Lattice Model. *Journal of Structural Engineering*, 145(9), 04019091. [https://doi.org/10.1061/\(ASCE\)ST.1943-541X.0002381](https://doi.org/10.1061/(ASCE)ST.1943-541X.0002381)
- Bahçecioğlu, T., Albostan, U., & Kurç, Ö. (2012). *An Extensible Parallel Finite Element Analysis Environment : Panthalassa*. October, 17–19.
- Baril, M. A., Sorelli, L., Réthoré, J., Baby, F., Toutlemonde, F., Ferrara, L., Bernardi, S., & Fafard, M. (2016). Effect of casting flow defects on the crack propagation in UHPFRC thin slabs by means of stereovision Digital Image Correlation. *Construction and Building Materials*. <https://doi.org/10.1016/j.conbuildmat.2016.10.102>
- Baweja, S. (1995). Creep and shrinkage prediction model for analysis and design of concrete structures- model B3. *Materials and Structures*, 28(6), 357–365. <https://doi.org/10.1007/BF02473152>
- Buttlar, W. G., Hill, B. C., Kim, Y. R., Kutay, M. E., Millien, A., Montepara, A., Paulino, G. H., Petit, C., Pop, I. O., Romeo, E., Roncella, R., Safavizadeh, S. A., Tebaldi, G., & Wargo, A. (2014). Digital image correlation techniques to investigate strain fields and cracking phenomena in asphalt materials. *Materials*

- and Structures/Materiaux et Constructions*, 47(8), 1373–1390. <https://doi.org/10.1617/s11527-014-0362-z>
- Destrebecq, J. F., Toussaint, E., & Ferrier, E. (2011). Analysis of Cracks and Deformations in a Full Scale Reinforced Concrete Beam Using a Digital Image Correlation Technique. *Experimental Mechanics*. <https://doi.org/10.1007/s11340-010-9384-9>
- Di Luzio, G. (2009). Numerical model for time-dependent fracturing of concrete. *Journal of Engineering Mechanics*. [https://doi.org/10.1061/\(ASCE\)0733-9399\(2009\)135:7\(632\)](https://doi.org/10.1061/(ASCE)0733-9399(2009)135:7(632))
- Erdem, S., Dawson, A. R., & Thom, N. H. (2012). Influence of the micro- and nanoscale local mechanical properties of the interfacial transition zone on impact behavior of concrete made with different aggregates. *Cement and Concrete Research*, 42(2), 447–458. <https://doi.org/10.1016/j.cemconres.2011.11.015>
- Gajewski, T., & Garbowski, T. (2014). Calibration of concrete parameters based on digital image correlation and inverse analysis. *Archives of Civil and Mechanical Engineering*, 14(1), 170–180. <https://doi.org/10.1016/j.acme.2013.05.012>
- GOM Correlate (No. 2018). (2018). <https://www.gom.com/>
- Grasley, Z. C., & Lange, D. A. (2004). Modeling drying shrinkage stress gradients in concrete. *Cement, Concrete and Aggregates*. <https://doi.org/10.1520/cca12302>
- Grassl, P., Wong, H. S., & Buenfeld, N. R. (2010). Influence of aggregate size and volume fraction on shrinkage induced micro-cracking of concrete and mortar. *Cement and Concrete Research*. <https://doi.org/10.1016/j.cemconres.2009.09.012>
- Grzybowski, M., & Shah, S. P. (1989). Model to predict cracking in fibre reinforced concrete due to restrained shrinkage. *Magazine of Concrete Research*, 41(148), 125–135. <https://doi.org/10.1680/mac.1989.41.148.125>
- Hashin, Z., & Shtrikman, S. (1963). A variational approach to the theory of the elastic behaviour of multiphase materials. *Journal of the Mechanics and Physics of Solids*, 11(2), 127–140. [https://doi.org/10.1016/0022-5096\(63\)90060-7](https://doi.org/10.1016/0022-5096(63)90060-7)
- Hedegaard, B. (2020). Creep and Shrinkage Modeling of Concrete Using Solidification Theory. *Journal of Materials in Civil Engineering*. [https://doi.org/10.1061/\(asce\)mt.1943-5533.0003256](https://doi.org/10.1061/(asce)mt.1943-5533.0003256)
- Holt, E. (2005). Contribution of mixture design to chemical and autogenous shrinkage of concrete at early ages. *Cement and Concrete Research*. <https://doi.org/10.1016/j.cemconres.2004.05.009>
- Holt, E. E. (2001). Early age autogenous shrinkage of concrete. *VTT Publications*.
- Hoult, N. A., Dutton, M., Hoag, A., & Take, W. A. (2016). Measuring crack

- movement in reinforced concrete using digital image correlation: Overview and application to shear slip measurements. *Proceedings of the IEEE*. <https://doi.org/10.1109/JPROC.2016.2535157>
- Idiart, A. E., López, C. M., & Carol, I. (2011). Modeling of drying shrinkage of concrete specimens at the meso-level. *Materials and Structures/Materiaux et Constructions*, 44(2), 415–435. <https://doi.org/10.1617/s11527-010-9636-2>
- Jin, T., Ha, N. S., Le, V. T., Goo, N. S., & Jeon, H. C. (2015). Thermal buckling measurement of a laminated composite plate under a uniform temperature distribution using the digital image correlation method. *Composite Structures*, 123, 420–429. <https://doi.org/10.1016/j.compstruct.2014.12.025>
- Kalaycıoğlu, M. T., Albostan, U., Işık, G., Canbay, E., Arıcı, Y., Binici, B., & Tuncay, K. (2018). *Experimental Studies on Reinforced Concrete Pressure Tunnels*. September, 12–14.
- Keskin, S. B., Sahmaran, M., Yaman, I. O., & Lachemi, M. (2014). Correlation between the viscoelastic properties and cracking potential of engineered cementitious composites. *Computers and Chemical Engineering*. <https://doi.org/10.1016/j.conbuildmat.2014.08.089>
- Lionello, G., & Cristofolini, L. (2014). A practical approach to optimizing the preparation of speckle patterns for digital-image correlation. *Measurement Science and Technology*. <https://doi.org/10.1088/0957-0233/25/10/107001>
- Luković, M., Šavija, B., Schlangen, E., Ye, G., & van Breugel, K. (2016). A 3D lattice modelling study of drying shrinkage damage in concrete repair systems. *Materials*. <https://doi.org/10.3390/MA9070575>
- Madenci, E., & Oterkus, E. (2014). *Peridynamic Theory and Its Applications*. In *Peridynamic Theory and Its Applications*. Springer New York. <https://doi.org/10.1007/978-1-4614-8465-3>
- Maruyama, I., Sasano, H., & Lin, M. (2016). Impact of aggregate properties on the development of shrinkage-induced cracking in concrete under restraint conditions. *Cement and Concrete Research*, 85, 82–101. <https://doi.org/10.1016/j.cemconres.2016.04.004>
- Maruyama, I., & Sugie, A. (2014). Numerical Study on Drying Shrinkage of Concrete Affected by Aggregate Size. *Journal of Advanced Concrete Technology*, 12(8), 279–288. <https://doi.org/10.3151/jact.12.279>
- MATLAB* (No. R2015a). (2015). <https://www.mathworks.com/help/matlab/release-notes-R2015a.html>
- Mauroux, T., Benboudjema, F., Turcry, P., Aït-Mokhtar, A., & Deves, O. (2012). Study of cracking due to drying in coating mortars by digital image correlation. *Cement and Concrete Research*, 42(7), 1014–1023.

<https://doi.org/10.1016/j.cemconres.2012.04.002>

- Meng, L., Jin, G., & Yao, X. (2006). Errors caused by misalignment of the optical camera axis and the object surface in the DSCM. *Qinghua Daxue Xuebao/Journal of Tsinghua University*.
- Nghiem, H. L., Al Heib, M., & Emeriault, F. (2015). Method based on digital image correlation for damage assessment in masonry structures. *Engineering Structures*. <https://doi.org/10.1016/j.engstruct.2014.12.021>
- Photoshop (CS6.0). (2012). Adobe. <http://www.adobe.com/products/photoshop/selector.html>
- Qi, C. (2005). Characterization of plastic shrinkage cracking in fiber reinforced concrete using image analysis and a modified Weibull function. *Materials and Structures*, 36(260), 386–395. <https://doi.org/10.1617/12686>
- Qi, C., Weiss, J., & Olek, J. (2003). Characterization of plastic shrinkage cracking in fiber reinforced concrete using image analysis and a modified Weibull function. *Materials and Structures/Materiaux et Constructions*. <https://doi.org/10.1007/bf02481064>
- Rao, G. A. (2001). Long-term drying shrinkage of mortar — influence of silica fume and size of fine aggregate. *Cement and Concrete Research*, 31(2), 171–175. [https://doi.org/10.1016/s0008-8846\(00\)00347-1](https://doi.org/10.1016/s0008-8846(00)00347-1)
- Rezvani, M., Proske, T., & Graubner, C. A. (2019). Modelling the drying shrinkage of concrete made with limestone-rich cements. *Cement and Concrete Research*, 115, 160–175. <https://doi.org/10.1016/j.cemconres.2018.09.003>
- Romeo, E. (2013). Two-dimensional digital image correlation for asphalt mixture characterisation: interest and limitations. *Road Materials and Pavement Design*, 14(4), 747–763. <https://doi.org/10.1080/14680629.2013.815128>
- Sadouki, H., & Van Mier, J. G. M. (1997). Meso-level analysis of moisture flow in cement composites using a lattice-type approach. *Materials and Structures/Materiaux et Constructions*. <https://doi.org/10.1007/bf02486899>
- Schlangen, E., Koenders, E. A. B. A. B., & van Breugel, K. (2007). Influence of internal dilation on the fracture behaviour of multi-phase materials. *Engineering Fracture Mechanics*, 74(1–2), 18–33. <https://doi.org/10.1016/j.engfracmech.2006.01.033>
- SEM. (2014). *Society for Experimental Mechanics*. <https://sem.org/dicchallenge>
- Shah, S. G., & Kishen, J. M. C. (2011). Fracture Properties of Concrete-Concrete Interfaces Using Digital Image Correlation. *Experimental Mechanics*. <https://doi.org/10.1007/s11340-010-9358-y>
- Silling, S. A. (2000). Reformulation of elasticity theory for discontinuities and long-

- range forces. *Journal of the Mechanics and Physics of Solids*, 48(1), 175–209. [https://doi.org/https://doi.org/10.1016/S0022-5096\(99\)00029-0](https://doi.org/https://doi.org/10.1016/S0022-5096(99)00029-0)
- Silling, S. A., & Askari, E. (2005). A meshfree method based on the peridynamic model of solid mechanics. *Computers and Structures*. <https://doi.org/10.1016/j.compstruc.2004.11.026>
- Soysal Albostan, F., Aydin, B. B., Tuncay, K., Arici, Y., & Binici, B. (2017). *Overlapping Lattice Simulation of Concrete Gravity Dam Collapse Scenarios*. June, 730–738. <https://doi.org/10.7712/120117.5453.18423>
- Su, Y. Q., Yao, X. F., Wang, S., & Ma, Y. J. (2015). Improvement on measurement accuracy of high-temperature DIC by grayscale-average technique. *Optics and Lasers in Engineering*, 75, 10–16. <https://doi.org/10.1016/j.optlaseng.2015.06.003>
- Sutton, M. A., Orteu, J. J., & Schreier, H. (2009). Image correlation for shape, motion and deformation measurements: Basic concepts, theory and applications. In *Image Correlation for Shape, Motion and Deformation Measurements: Basic Concepts, Theory and Applications*. <https://doi.org/10.1007/978-0-387-78747-3>
- Tang, S. B., Wang, S. Y., Ma, T. H., Tang, C. A., Bao, C. Y., Huang, X., & Zhang, H. (2016). Numerical study of shrinkage cracking in concrete and concrete repair systems. *International Journal of Fracture*, 199(2), 229–244. <https://doi.org/10.1007/s10704-016-0108-8>
- Tang, S. B., Yu, Q. L., Li, H., Yu, C. Y., Bao, C. Y., & Tang, C. A. (2013). Mesomechanical model of moisture diffusion and shrinkage cracking in building material – Model development. *Construction and Building Materials*, 47, 511–529. <https://doi.org/10.1016/j.conbuildmat.2013.05.040>
- Tang, X., Zhou, Y., Zhang, C., & Shi, J. (2011). Study on the Heterogeneity of Concrete and Its Failure Behavior Using the Equivalent Probabilistic Model. *Journal of Materials in Civil Engineering*, 23(4), 1–19. [https://doi.org/10.1061/\(ASCE\)MT.1943-5533](https://doi.org/10.1061/(ASCE)MT.1943-5533)
- Turcry, P., Loukili, A., Haidar, K., Pijaudier-Cabot, G., & Belarbi, A. (2006). Cracking tendency of self-compacting concrete subjected to restrained Shrinkage: Experimental study and modeling. *Journal of Materials in Civil Engineering*. [https://doi.org/10.1061/\(ASCE\)0899-1561\(2006\)18:1\(46\)](https://doi.org/10.1061/(ASCE)0899-1561(2006)18:1(46))
- van Mier, J. G. M. (2012). Concrete fracture: A multiscale approach. In *Concrete Fracture: A Multiscale Approach* (1st ed.). CRC Press. <https://doi.org/10.1201/b12968>
- W.Mokarem, D. (2002). Development of concrete shrinkage performance specifications. *Virginia Polytechnic Institute and State University*.
- Wallah, S. E. (2009). Drying Shrinkage of Heat-Cured Fly Ash-Based Geopolymer

- Concrete. *Modern Applied Science*, 3(12). <https://doi.org/10.5539/mas.v3n12p14>
- Weiss, W. J., Yang, W., & Shah, S. P. (1998). Shrinkage Cracking of Restrained Concrete Slabs. *Journal of Engineering Mechanics*, 124(7), 765–774. [https://doi.org/10.1061/\(asce\)0733-9399\(1998\)124:7\(765\)](https://doi.org/10.1061/(asce)0733-9399(1998)124:7(765))
- Weiss, W. J., Yang, W., & Shah, S. P. (2000). Influence of specimen size/geometry on shrinkage cracking of rings. *Journal of Engineering Mechanics*. [https://doi.org/10.1061/\(ASCE\)0733-9399\(2000\)126:1\(93\)](https://doi.org/10.1061/(ASCE)0733-9399(2000)126:1(93))
- Wu, H. Y., Rubinstein, M., Shih, E., Guttag, J., Durand, F., & Freeman, W. (2012). Eulerian video magnification for revealing subtle changes in the world. *ACM Transactions on Graphics*. <https://doi.org/10.1145/2185520.2185561>

APPENDICES

A. Features of DSLR Cameras

Features of the DSLR cameras used in this study are presented in Table A-1.

Table A-1 Features of DSLR cameras

				
Model	Nikon D5200	Nikon D5300	Nikon D300	Nikon D800
Resolution (Photo)	24.1 MP (6000 x 4000)	24.2 MP (6000 x 4000)	12.3 MP (4288 x 2848)	36.3 MP (7360 x 4912)
Resolution (Video)	2 MP (1920 x 1080)	2 MP (1920 x 1080)	1 MP (1280 x 720)	2 MP (1920 x 1080)
Sensor Size (mm)	23.5 x 15.6	23.5 x 15.6	23.6 x 15.8	35.9 x 24.0
Sensor Type	CMOS	CMOS	CMOS	CMOS
Lens	AF-S NIKKOR 18-105mm f/3.5-5.6G ED VR	AF-S NIKKOR 18-105mm f/3.5-5.6G ED VR	18-200mm f/3.5-5.6G ED VR	AF NIKKOR 20mm f/2.8 D

CURRICULUM VITAE

PERSONAL INFORMATION

Surname, Name : Albostan, Utku
Nationality : Turkish (TC)
Date and Place of Birth : 21 February 1987, Ankara
Phone : +90 5052332186
E-mail : utku.albostan@metu.edu.tr

EDUCATION

Degree	Institution	Year of Graduation
MS	METU Civil Engineering	2013
BS	METU Civil Engineering	2010
High School	Mehmet Emin Resulzade High School, Ankara	2005

WORK EXPERIENCE

Year	Place	Enrollment
2018-Present	LARSA Eurasia	Research and Software Engineer
2012-2018	Civil Eng. Dep. / METU	Research Assistant
2010-2013	TÜBİTAK	Project Assistant
2009-July	PROMER Müş. & Müh. A.Ş.	Intern Engineering Student

FOREIGN LANGUAGES

Advanced English

PUBLICATIONS

1. Bahçecioğlu, T., Albostan U., Kurç, Ö. (2012). “An Extensible Parallel Finite Element Analysis Environment: Panthalassa”, 10th International Congress on Advances in Civil Engineering, 17-19 October 2012, Ankara, Turkey.
2. Yılmaz, A., Albostan, U., Caner, A., Kurc, O. (2014) “Temperature Gradient Map for Turkey”, Istanbul Bridge Conference, August 2014, İstanbul, Turkey.

3. Yilmaz, A., Albostan, U., Caner, A., Kurc, O. (2016) “Turkish Solar Radiation Zones for Segmental Girder Bridge Design Under Temperature Gradient Loading”. In: Caner A, Gülkan P. Mahmoud K. (eds) *Developments in International Bridge Engineering*. Springer Tracts on Transportation and Traffic, vol 9. Springer, Cham. DOI: 10.1007/978-3-319-19785-2_7
4. Albostan, U. and Kurç, Ö. (2016). “Application of two-dimensional Digital Image Correlation: Three Points Flexure Test of Reinforced Concrete Beam”, 12th International Congress on Advances in Civil Engineering, 21-23 September 2016, İstanbul, Turkey.
5. Albostan, U., Bahcecioglu, T., Arici, Y., Kurc, O. (2017). “Nonlinear Seismic Dam and Foundation Analysis Using Explicit Newmark Integration Method with Static Condensation”, 10th International Conference on Structural Dynamics (EURODYN), Rome, Italy, 10 - 13 September 2017, vol.199, pp.316-321.
6. Gargari, A. M., Ozbey, B., Demir, H. V., Altintas, A., Albostan, U., Kurc O., Erturk, V. B. (2018). “A Wireless Metamaterial-Inspired Passive Rotation Sensor With Submilliradian Resolution”, *IEEE SENSORS JOURNAL*, vol. 18, Issue 11, pp. 4482-4490.
7. Işık, G., Kalaycıoğlu, M. T., Albostan, U., Canbay, E., Arici, Y., Binici, B., Tuncay, K. (2018). “Numerical Modeling of Reinforced Concrete Pressure Tunnels Using the Overlapping Lattice Method”, 13th International Congress on Advances in Civil Engineering, 12-14 September 2018, İzmir, Turkey.
8. Kalaycıoğlu, M. T., Albostan, U., Işık, G., Canbay, E., Arici, Y., Binici, B., Tuncay, K. (2018). “Experimental Studies on Reinforced Concrete Pressure Tunnels”, 13th International Congress on Advances in Civil Engineering, 12-14 September 2018, İzmir, Turkey.

HOBBIES

Cycling, Making Electronics Circuits